EXPERIMENTAL AND NUMERICAL MODELING OF FLUID INJECTION INTO UNCONSOLIDATED FORMATIONS

A Thesis
Presented to
The Academic Faculty

by

Longde Jin

In Partial Fulfillment
of the Requirements for the Degree
Doctor of Philosophy in the
School of Civil and Environmental Engineering

Georgia Institute of Technology
December 2017

EXPERIMENTAL AND NUMERICAL MODELING OF FLUID INJECTION INTO UNCONSOLIDATED FORMATIONS

Approved by:

Dr. Haiying Huang, Advisor
School of Civil and Environmental Engineering
Georgia Institute of Technology

Dr. Susan E. Burns
School of Civil and Environmental Engineering
Georgia Institute of Technology

Dr. J. David Frost
School of Civil and Environmental Engineering
Georgia Institute of Technology

Dr. Leonid Germanovich
School of Civil and Environmental Engineering
Georgia Institute of Technology

Dr. Ying Zhang
School of Electrical and Computer Engineering
Georgia Institute of Technology

Date Approved: August 18, 2017

To my parents, who taught me love of life

ACKNOWLEDGEMENTS

I would like to thank for the support from the Sand Control Client Advisory Board of Schlumberger and the National Science Foundation through grant NSF/CMMI-1055882. I also wish to thank Itasca Consulting Group, Inc. for the education software loan of PFC®.

I would like to express my sincere gratitude to my advisor, Dr. Haiying Huang, for her patience, guidance, encouragement, and inspiration throughout the course of my Ph.D. Her scope of big pictures motivates me to keep pursuing my research goals.

I also want to acknowledge my Ph.D. thesis committee members, Dr. Susan Burns, Dr. J. David Frost, Dr. Lenoid Germanovich, and Dr. Ying Zhang, for their valuable comments and suggestions.

Special thanks to Dr. Sheng Dai, Dr. Chloe Arson, and Dr. Paul Mayne for their valuable suggestions and insights. I acknowledge my former group members, Fengshou Zhang, Yifei Ma, and Yixuan Sun, for their help. Furthermore, I thank all Geo-society fellows for their valuable discussions and suggestions. In particular, I appreciate Joshua Smith and Karie Yamamoto for their inputs in my dissertation. I am grateful to my friends Fangzhou Liu, Cheng Zhu, Bo Wang, Yue Zhao, Jongmuk Won, Koochul Ji, and Mahdi Roozbahani for their constant supports and encouragements during my Ph.D. journey.

Lastly, I would like to express my appreciation to my parents, Fengwan Jin and Zhenshun Cui, for their endless support and love. Also, I want to extend my gratitude to the care and patience from Miss Lina Quan.

TABLE OF CONTENTS

LIST OF TABLES

LIST OF FIGURES

SUMMARY

Both the fracturing and acid cleaning processes in unconsolidated reservoirs are examined in this work. Specifically, we first focus on characterizing how the fracture morphology and fluid leakoff are affected by the injection rate, fluid rheology and formation permeability. A series of injection experiments is performed with mixtures of sand and silica flour as analog materials for unconsolidated formations. We show that as the weight percentage of the silica flour increases, the matrix permeability decreases significantly and the capillary effect becomes non-negligible. Compared with the injection experiments with pure sand, an additional dimensionless number incorporating surface tension is introduced in order to characterize the fluid-grain displacement process. Effect of the non-Newtonian fluid rheology is subsequently analyzed using the discrete element method (DEM) coupled with a pore-network model. The quasi-steady-state fluid flow algorithm is improved to enhance numerical stability in modeling fluid injection in a wellbore. It is shown that the high shear rate rheology is critical to the near-wellbore failure and fluid flow. Furthermore, a hybrid phase field method is constructed to model the fracturing process. The benefit of the phase field method is that creation of a fracture could be modeled through explicit consideration of phase change. Finally, the acid cleaning process is simulated using a hydro-chemically coupled scheme implemented in an equation based solver. Effects of the injection rate, the acid reaction rate and the fracture conductivity are examined. Outcomes from this research could serve as guidelines to optimize the field practice.

CHAPTER I

INTRODUCTION

Understanding the failure mechanisms and fluid flow patterns in response to fluid injection into unconsolidated formations is critical to reservoir stimulation and production. While hydraulic fracturing is commonly employed to create pathways of increased permeability to connect a wellbore with the reservoir matrix, the fracturing process in such weakly cemented and highly permeable formations remains poorly understood. Meanwhile, production in these reservoirs is often accompanied by fines migration, which could substantially reduce the fracture permeability, consequently hampering productivity in the long term. In practice, acid could be injected into the production zone in order to recover the fracture conductivity. Motivated by these engineering applications, both the fracturing and acid cleaning processes in the unconsolidated reservoirs are examined in this work.

Granular media have been used as analog materials to investigate the fluid injection process in weak formations [9, 21, 22, 12, 23, 33, 43, 52]. Specifically, in the case of fluid injection into densely packed dry granular media, the granular response was observed to occur in four distinct regimes [41]: (i) a simple radial flow regime, (ii) an infiltration-dominated regime, (iii) a grain displacement-dominated regime, and (iv) a viscous fingering-dominated regime. A dimensionless number $\tau_1 = \eta v l / E k$ was used to characterize the granular movements, where η is fluid viscosity; v is the characteristic fluid velocity; l is a characteristic length scale; E is Young's modulus; and k is the permeability. The classification was obtained through injection tests with different combinations of fluid injection rate and viscosity in densely packed F110 sand in a Hele-Shaw cell [41]. In this work, a question we ask is whether the

the permeability scaling can be verified experimentally. Meanwhile, at low matrix permeability, the capillary effect may become non-negligible. Injection experiments are therefore performed to investigate the effects of permeability and capillarity on the fluid-grain displacement patterns using mixtures of Ottawa F110 sand and silica flour as model materials.

In practice, rheology of the fracturing fluid is generally non-Newtonian [25]. Laboratory injection experiments show fluid rheology has a strong influence on the fracturing behaviors [9, 12, 29, 30, 43, 44, 52, 53]. For a complex fluid, the rheological signatures may include shear thinning, zero shear viscosity, yield stress, thixotropy, viscoelasticity, etc. Furthermore, behaviors of flow in porous media may be further affected by the multi-phase characteristics of the fluids in that both external and internal filter cakes may develop. It is, however, important to understand how and when a certain rheological signature plays a critical role. A unique benefit of numerical analysis is that the effect of rheology can be explored by isolating the rheological signatures. Effect of the shear thinning rheology is investigated with a DEM-pore network coupled model based on PFC2D®.

As a continuum approach, the pressurized crack propagation can be simulated with the phase field method [10, 56, 67, 72, 73, 74, 75, 95]. The phase field method has been widely used to model the solidification process [82]. A benefit of the method is that the creation of a fracture could be modeled through explicit consideration of phase change so that the numerical scheme is free from tracking the sharp interface. A fixed grid mesh setup can be used, thereby reducing the computational cost [73]. Evolution of the phase field variable can be modeled as either quasi-static or viscous. Quasi-static phase evolution has been recently adopted to simulate the hydraulic fracturing process [10, 73, 74, 56, 57, 95]. However, it was shown that viscous regularization provides a more stable scheme, compared to the quasi-static process [70]. Furthermore, various forms of the constitutive law have been used with the assumption that fractures can

be only created in tension. Compared to non-linear forms in [4, 70], the linear form of the hybrid scheme [2] significantly reduces computational cost. In this work, a hybrid phase field method is developed by adopting viscous phase evolution and the hybrid scheme for constitutive law to investigate the pressurized fracture propagation problem. The model is constructed and implemented in the equation based solver COMSOL Multiphysics®.

Lastly, acid cleaning process is a multi-physics problem which involves fluid flow in porous media, chemical reaction, and chemical transport. In this work, the acid cleaning process is modeled using hydro-chemically coupled scheme implemented in the equation based solver COMSOL Multiphysics® to investigate the effects of injection rate, dimensionless fracture conductivity, and reaction rate on the effectiveness of acid cleaning.

The chapters are structured as follows.

Chapter 2 "Granular fingering in fluid injection into a densely packed sand and silica flour mixture" presents the experimental study on the effects of permeability and capillarity during fluid injection into a densely packed sand and silica flour mixture in a Hele-Shaw cell.

Chapter 3 "Effect of non-Newtonian rheology on fluid injection into dense granular media" presents the DEM-pore network coupled model to investigate the effect of non-Newtonian fluid rheology.

Chapter 4 "Phase field method for pressurized fracture propagation in porous media" presents a hybrid phase field method as a continuum numerical approach to model pressurized fracture propagation.

Chapter 5 "Acid cleaning to recover fracture conductivity" presents a numerical analysis to examine the effects of the injection rate, the acid reaction rate, and the fracture conductivity on the effectiveness of acid cleaning.

Chapter 6 "Conclusions and future work" summarizes the main findings obtained

from this research and provides some suggestions for future work.

CHAPTER II

GRANULAR FINGERING IN FLUID INJECTION INTO A DENSELY PACKED SAND AND SILICA FLOUR MIXTURE

2.1 Introduction

Granular media have been used as analog materials to investigate the fluid injection process in weak formations. Injection experiments in triaxial cells were performed to investigate the effects of fluid rheology, the leakoff characteristics, and the confining stresses on the fracturing process in compacted saturated sand in [9, 21, 22, 23, 52], and by the research group led by Prof. Leonid Germanovich at Georgia Tech [12, 33, 43]. To analyze the fracture geometry, Chang [12] and Hurt [43] excavated the fracture after the solidification of the fracturing fluid. A recent study shows that the real-time fracturing process could be also monitored with acoustic emission testing [33]. In another approach, Dong et al. [22] employed X-ray CT (Computed Tomography) for subsequent scans of a test with multiple injection of cross-linked gel.

An alternative way of monitoring real-time fluid and grain kinematics is to use a Hele-Shaw cell, which consists of two transparent plexi-glass plates with a fixed gap simulating a two dimensional condition. The Hele-Shaw cell has been used as an analog model for a rigid porous medium with a constant permeability, where the gap size translates to the permeability, since the processes of steady state fluid flow in between two plates and flow in porous media are both governed by the Laplacian equation. Hydrodynamic instability in both linear and radial Hele-Shaw cells has been extensively studied in depth both mathematically and experimentally since the pioneering work in [36, 83, 16], and subsequent research in [62, 68, 80]. Fluid-fluid displacement

is also conducted in a Hele-Shaw cell filled with granular materials [63, 65], where the different fluid displacement patterns are characterized by capillary number Ca and mobility M [38, 60]. The capillary number Ca is the ratio of viscous force to capillary force, while the mobility M is the ratio of invading fluid viscosity to displacing fluid. At large Ca, the capillary effect is negligible, and fluid invasion depending on M. If $M < 1$, hydrodynamic instability in the form of viscous fingering. When $M > 1$, fluid displacement is stable. At a low capillary number, capillary fingering is dominant, and the fluid displacement pattern is insensitive to fluid mobility. The response of bentonite clay suspensions during injection can be characterized by the Deborah number $D_e = t_c/t_p$, where t_c is the stress relaxation time, and t_p refers to the characteristic time scale of an experiment [92].

Deformability of porous media in a Hele-Shaw cell was first captured by van Damme et al. [93] where air is injected into dry powder. Striking similarity to viscous fingering is reported and also in fingering in colloidal paste [59, 58]. Johnsen et al. [48, 47, 46] conducted a series of air injection tests into loosely compacted granular material in Hele-Shaw cells and discussed about the injection pressure effect on the particle displacements near injection point and the finger front. Unlike the loosely packed scenario, Cheng et al. [14] identified that granular fingering exists at the zero-surface tension limit, in which the wave number of the interface reaches infinite during viscous fingering. MacMinn [64] observed shear band formation near the wellbore where aqueous glycerin is injected into a densely packed mono-layer of soft particles.

Holtzman et al. [37] defined a fracture number $N_f = \frac{\gamma L^2}{\eta w d}(1 + Ca)$ to describe the capillary fracturing, where γ is surface tension, L a length scale, η fluid viscosity, w confining weight, and d the diameter of particles. They pointed out that N_f governs the transition from fluid flow in rigid porous media to grain displacement, where the grain displacements happen in low confinement or with a high capillary number.

However, N_f is insufficient to distinguish different grain displacement patterns in the fluid injection into densely packed dry granular media.

The fluid injection process involving grain displacement, specifically, pattern formation during fluid injection into densely packed dry granular media, has not been fully explored. The granular response was observed to occur in four distinct regimes [41]: (i) a simple radial flow regime, (ii) an infiltration-dominated regime, (iii) a grain displacement-dominated regime, and (iv) a viscous fingering-dominated regime. A dimensionless number $\tau_1 = \eta v l/Ek$ was used to characterize the granular movements, where η is fluid viscosity; v is the characteristic fluid velocity; l is a characteristic length scale; E is Young's modulus; and k is the permeability. The classification was obtained through injection tests with different combinations of fluid injection rate and viscosity in densely packed F110 sand in a Hele-Shaw cell [41]. In this work, a question we ask is whether the the permeability scaling can be verified experimentally. Meanwhile, at low matrix permeability, the capillary effect may become non-negligible. Injection experiments are therefore performed to investigate the effects of permeability and capillarity on the fluid-grain displacement patterns using mixtures of Ottawa F110 sand and silica flour as model materials.

The chapter is structured as follows. In Section 2.2, soil properties of the mixtures are first characterized from laboratory experiments. Experimental setup for the injection tests in Hele-Shaw cells are introduced in Section 2.3, and the displacement patterns from the injection experiments are presented in Section 2.4. In Section 2.5, an additional dimensionless number incorporating surface tension is derived to characterize the fluid-grain displacement. The boundaries are defined to classify the fluid-grain displacement patterns during fluid injection into sand silica flour mixtures.

Table 1: Index properties of Ottawa F110 sand and silica flour [12].

Soil Name	D_{50} (μm)	C_u	C_c	G_s	φ_{rep} (°)
Ottawa F110	110	1.6	1.0	2.65	27
Silica Flour	19	5.8	1.3	2.65	50

2.2 Soil properties

The granular materials for the study are mixtures of Ottawa F110 sand with silica flour. As fine content in different percentage by weight. Ottawa F110 has a nearly uniform grain size distribution with particle diameter ranging from 100 μm to 200 μm and a median diameter D_{50} of 110 μm. Silica flour used in the experiments is SIL-CO-SIL 106 from U.S. Silica with up to 99.8 % quartz. The mineralogy of both media is quartz, and the similarity in mineralogy minimizes the effect of wettability. Depending on the percentage of the silica flour, both mechanical properties and hydraulic conductivity of the mixture vary. The index properties of Ottawa F110 and silica flour are provided in Table 1, where the coefficient of uniformity $C_u = D_{60}/D_{10}$; the coefficient of curvature $C_c = (D_{30})^2/D_{10}D_{60}$; G_s is the specific gravity for quartz; and φ_{rep} is the angle of repose.

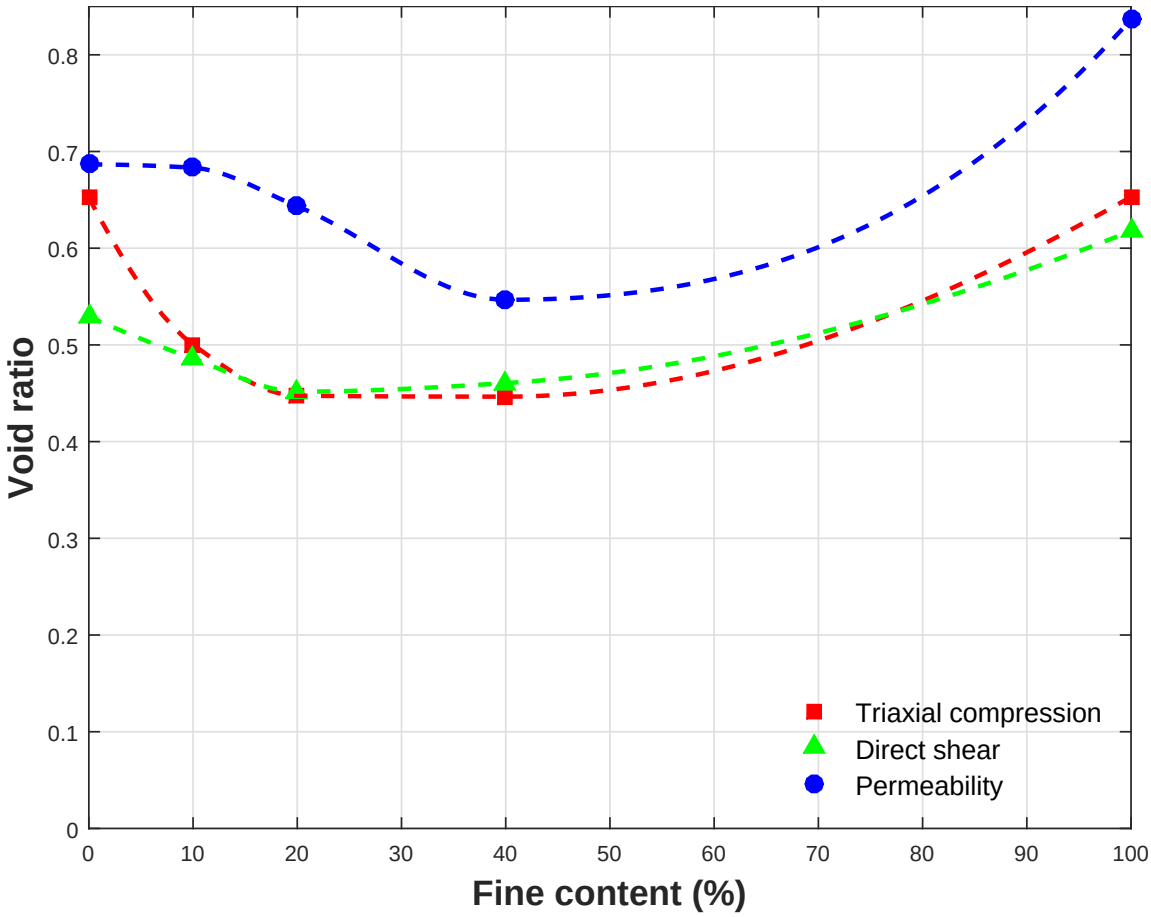

Figure 1: Average void ratio after compaction for material property testing.

The permeability measurement of the mixture is conducted using the flexible wall falling head method following ASTM D5084-03. A sample of 3.56 cm (1.4 inch) diameter and about 7.62 cm (3 inch) height is used. The sample is divided in three layers and slightly tamped 25 times at each layer to reach a dense state. The final averaged void ratio for each test is provided in Figure 1. Permeability is measured at a confining stress of 100 kPa. The measurement gives 2896 mD, 1314 mD, 406 mD, 30.4 mD, and 7.95 mD for 0 %, 10 %, 20 %, 40 %, and 100 % of silica by weight, respectively. Corresponding hydraulic conductivity is 2.8×10^{-3} cm/s, 1.3×10^{-3} cm/s, 3.9×10^{-4} cm/s, 2.9×10^{-5} cm/s, and 7.4×10^{-6} cm/s. The measured values are consistent with previous work by Hurt [43]. Figure 2 shows that as the weight

percentage of the silica flour increases, the matrix permeability decreases significantly. Though the permeability of the mixture with high fine content is relatively low, the poroelastic effect may be considered negligible. This can be illustrated by inspecting coefficient of the consolidation $c_v = k/\eta m_v$, where k is the soil permeability, η is the fluid viscosity, and m_v is the compressibility of the soil matrix which is in an order of magnitude of $O(10^{-7})$ 1/Pa for the mixture under 100 kPa. With given values, the consolidation coefficient of silica flour is in an order of $O(10^{-5})$ m^2/s, which leads to several seconds to reach 90% of consolidation in a standard oedometer test.

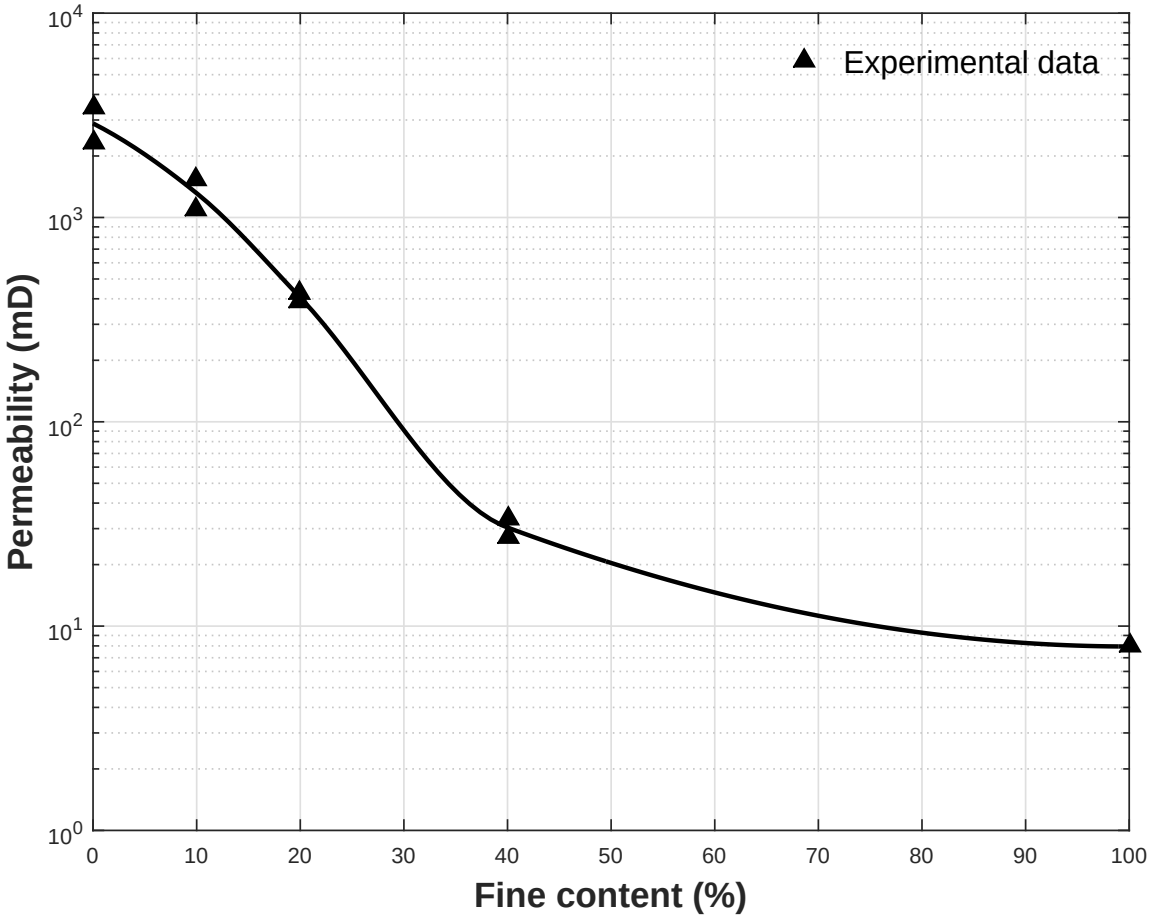

Figure 2: Permeability of mixtures of Ottawa F110 and silica flour measured by flexible wall falling head method at a confining stress of 100 kPa.

Moduli of the mixtures are measured through triaxial tests following ASTM D7181

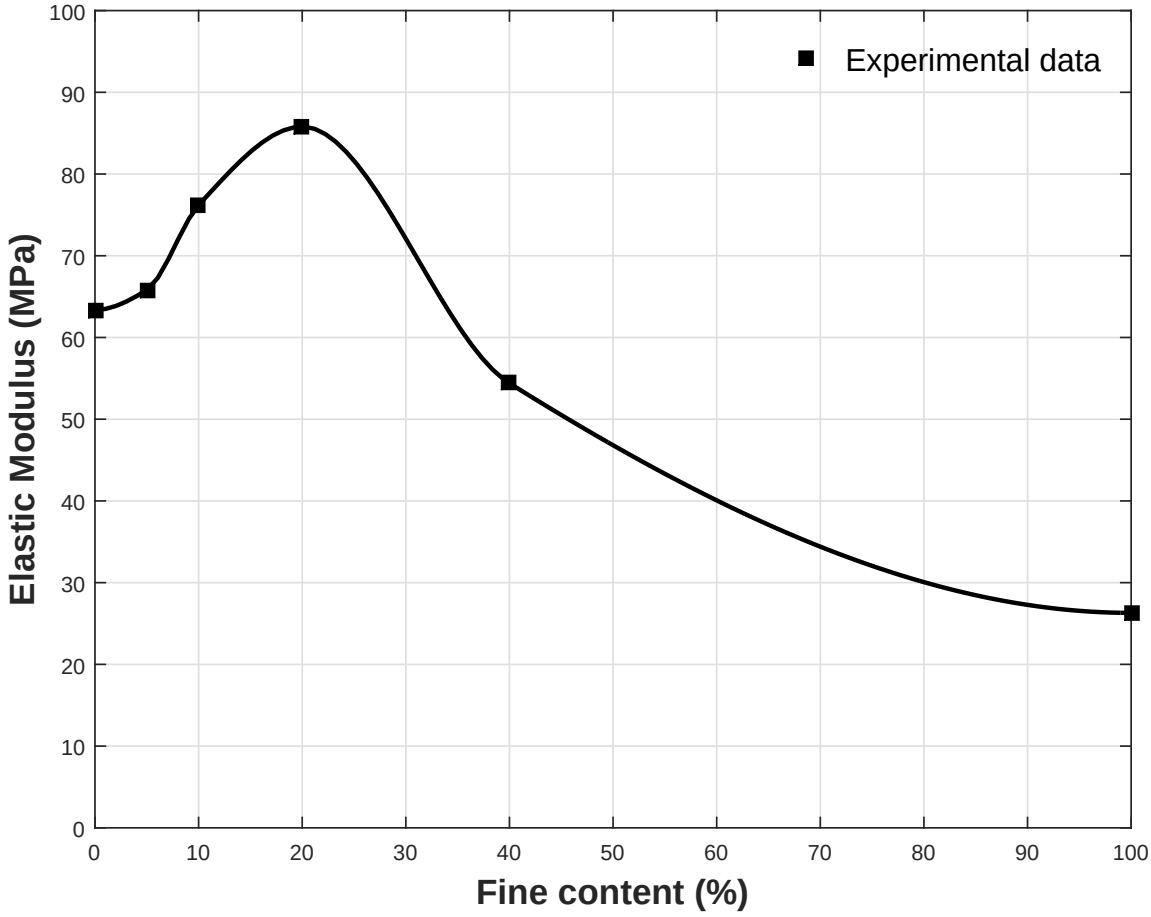

Figure 3: Elastic modulus of dry soil at the confining stress of 100 kPa.

at a confining stress of 100 kPa. The triaxial tests are conducted on dry samples. Each sample is about 7.11 cm (2.8 inch) in diameter and about 12.7 cm (5 inch) in height. Compaction is achieved through 5 sub-layers with each layer tamped 56 times to achieve a dense state. Although the final dense state of sample is different between sample from triaxial test and sample for the experiments, we maintain the same compaction effort (vibration period) during sample preparation in the Hele-Shaw cell to have consistency. The corresponding void ratio variation of the sample at the same packing effort is provided in Figure 1. The small strain modulus is obtained by averaging local slopes until 0.2 % of strain (13 data points). From Figure 3, it can be seen that the elastic modulus has a largest value around 20 % fine content. The variation of the modulus with the fine content can be explained by the fact that

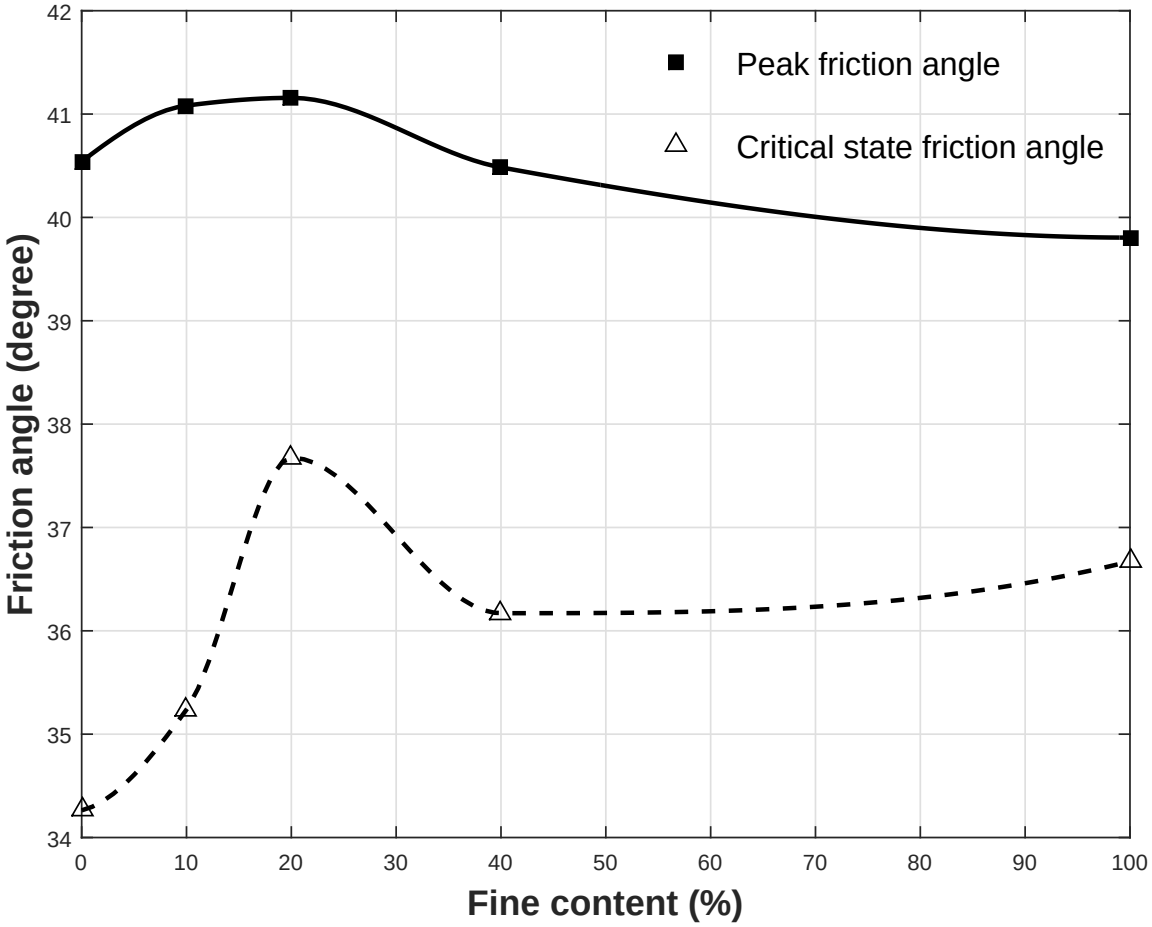

Figure 4: Friction angle variation with fine content %.

for binary mixture, the minimum void ratio at around 20 % results in the maximum coordination number, and therefore, the soil modulus is at maximum [84, 55, 28, 15].

Friction angle of the mixtures are measured by the direct shear test following ASTM D3080. The device has a loading capacity of 10 KN (2000 lb). A sample of 6.35 cm (2.5 inch) in diameter and roughly 2.54 cm (1 inch) in height is compacted in a cylindrical-shape container. For each specimen, five different trials with a normal stress of 80 kPa, 120 kPa, 160 kPa, 320 kPa, and 640 kPa are conducted to obtain the Mohr-Coloumb failure envelop. Dry sample is prepared with 56 times at each layer with three layers in total. The resulting $\sigma - \tau$ relation is fitted linearly based on an assumption of cohesionless soil. Nevertheless, It should be noted in the dry mixture, apparent cohesion could exist due to electrostatic force. Chang [12] reported that

oven-dried silica flour can stand at a vertical slope. The largest friction angle is also at about 20 % fine content (see Figure 4) which coincides with where the minimum void ratio occurs (see Figure 1). The densely packed soil also shows some dilation behavior with a dilatancy angle about 5°.

2.3 Experimental setup

The injection experiments were conducted in a radial Hele-Shaw cell. The cell is made of two pieces of clear acrylic plate bolted together at the four corners. Each plate is 30.48×30.48 cm (12×12 inch) and 2.54 cm (1 inch) in thickness. The gap between the plates is controlled by four stainless steel shims at the four corners where the bolts go through. It has been noted that the patterns created with different gap sizes (0.787 mm, 1.575 mm, 2.362 mm, and 3.175 mm) are comparable to each other [41], so the three dimensional flow effect is negligible. In this work, the gap size is chosen as 1.575 mm (0.031 inch) for all tests except Test V1 and V2 for a gap size of 0.787 mm (0.062 inch) to minimize the three dimensional effect. Dry soil is then filled in between the two plates. The mixture is poured from the top opening into the gap of the cell held in a vertical position with the other three sides are sealed by tape. Compaction is achieved by using a shake table. The acceleration of the shake table is around 5g and the lowest frequency is 20 Hz. For pure sand, each lifts vibrates 45 seconds with three layers total. Due to the existence of electrostatic force, as fine content increases, the grains tend to attach to the inner wall of the cell. To achieve a consistent density across samples of varying fine content, the vibration time is slightly extended. The vibration time is 1 minute for the case of pure silica flour and the soil with 40 % silica content. After compaction, the opening is taped, and the remaining three sides are vibrated 45 seconds respectively to minimize the grain segregation.

An injection port is installed beneath the bottom plate, and fluid is injected through a drill hole of 1.02 mm (0.04 inch) in diameter. The injection rate is held

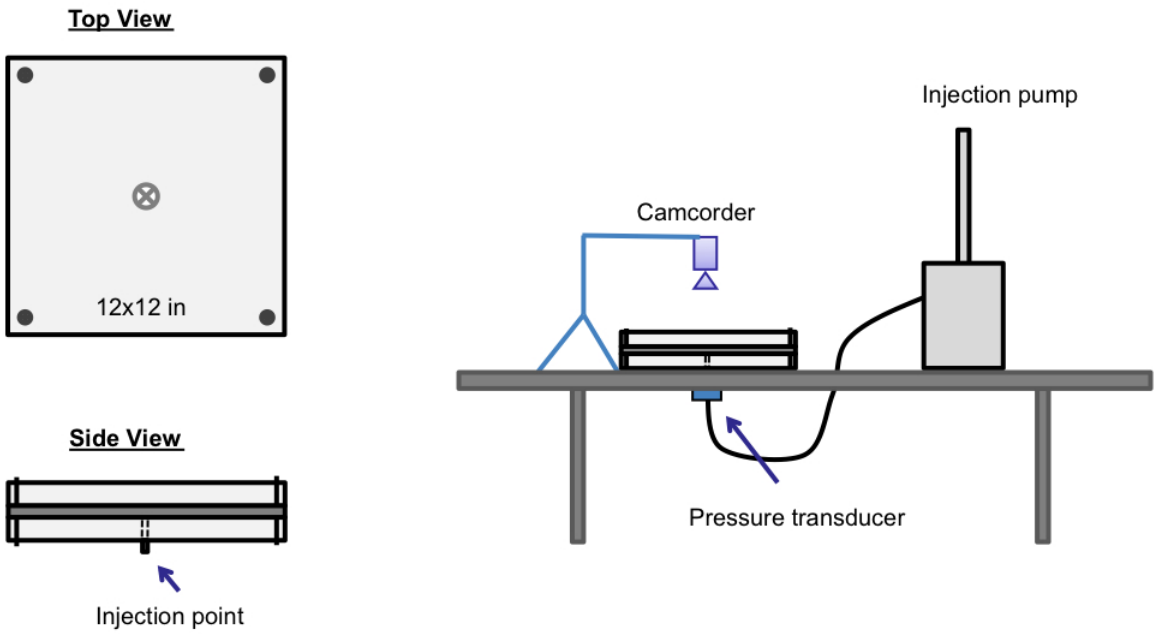

Figure 5: Schematic of the experimental setup [42].

constant with a high pressure syringe pump. Above the plates, a high speed camcorder (Canon VIXIA HFS100) is positioned to take sequential high-resolution photos during the injection process. A pressure transducer is installed at the injection port to monitor the wellbore pressure change during the experiment. The data is transferred through wireless sensors to the lab computer at a frequency of 100 Hz. The schematic of the setup is shown in Figure 5. The injected fluid is aqueous glycerin solution. It has the advantages of having a Newtonian rheology, being perfectly water dissoluble, and non-toxic. At 50 %, 90 %, and 100 % concentration by weight, the viscosity of aqueous glycerin solutions at room temperature (21 °C) is 5 cp, 176 cp, and 942 cp, respectively.

2.4 Grain displacement patterns

Injection test cases are provided in Table 2, where SF stands for the acronym of silica and F110, and digits represent the ratio of silica and sand, e.g., 0/100 stands for the weight percentage of silica content is 0 %. Selected displacement patterns at the

end of the experiment are shown in Figure 6. The black area at the center indicates the fluid channels, lighter area represents the fluid infiltrated area, and the gray area indicates the dry soil. The nominal injection velocity v at the injection well is defined as $v = Q/\pi D_i b$, where Q is the injection rate; D_i is the diameter of injection hole; and b is the gap size. For each test series from I to V, the effects of the injection rate and viscosity are similar to the experimental observations in [42, 40]. For example, in the case of series III, as the injection rate increases (comparing III1 with III2), the granular response changes from a nearly simple radial flow regime to an infiltration-dominated regime. In addition, at the same injection rate, the increase in fluid viscosity promotes the grain movements and limits the fluid infiltration (comparing III1 with III2). Huang et al. [41] introduced a dimensionless time parameter τ_1 to characterize the granular media behavior during fluid invasion.

$$\tau_1 = \frac{t_d}{t_i} = \frac{\mu v l}{Ek}, \tag{1}$$

where E is the initial small strain modulus of the media; k is the permeability; and l is a characteristic length (macro-scale) which can be given as inlet diameter D_i. τ_1 reflects the competition between the fluid pressure dissipation time $t_d = \mu l^2/Ek$ and the injection time $t_i = l/v$. The pattern can be classified into four regimes: (i) a simple radial flow regime, (ii) an infiltration-dominated regime, (iii) a grain displacement dominated regime, and (iv) a viscous fingering-dominated regime. Based on the definition of τ_1, reduction in permeability should be similar to the effect of increase in injection rate or viscosity. In the experiments, fingers are developed at low permeability, under low injection rate and low fluid viscosity. For example, the pattern gradually changes from simple radial flow regime (see I1 in Figure 6) to infiltration governed regime (see V1 in Figure 6). The permeability effect can be also identified by comparing I2 with IV2 where the fluid permeation is more limited in IV2 than I2.

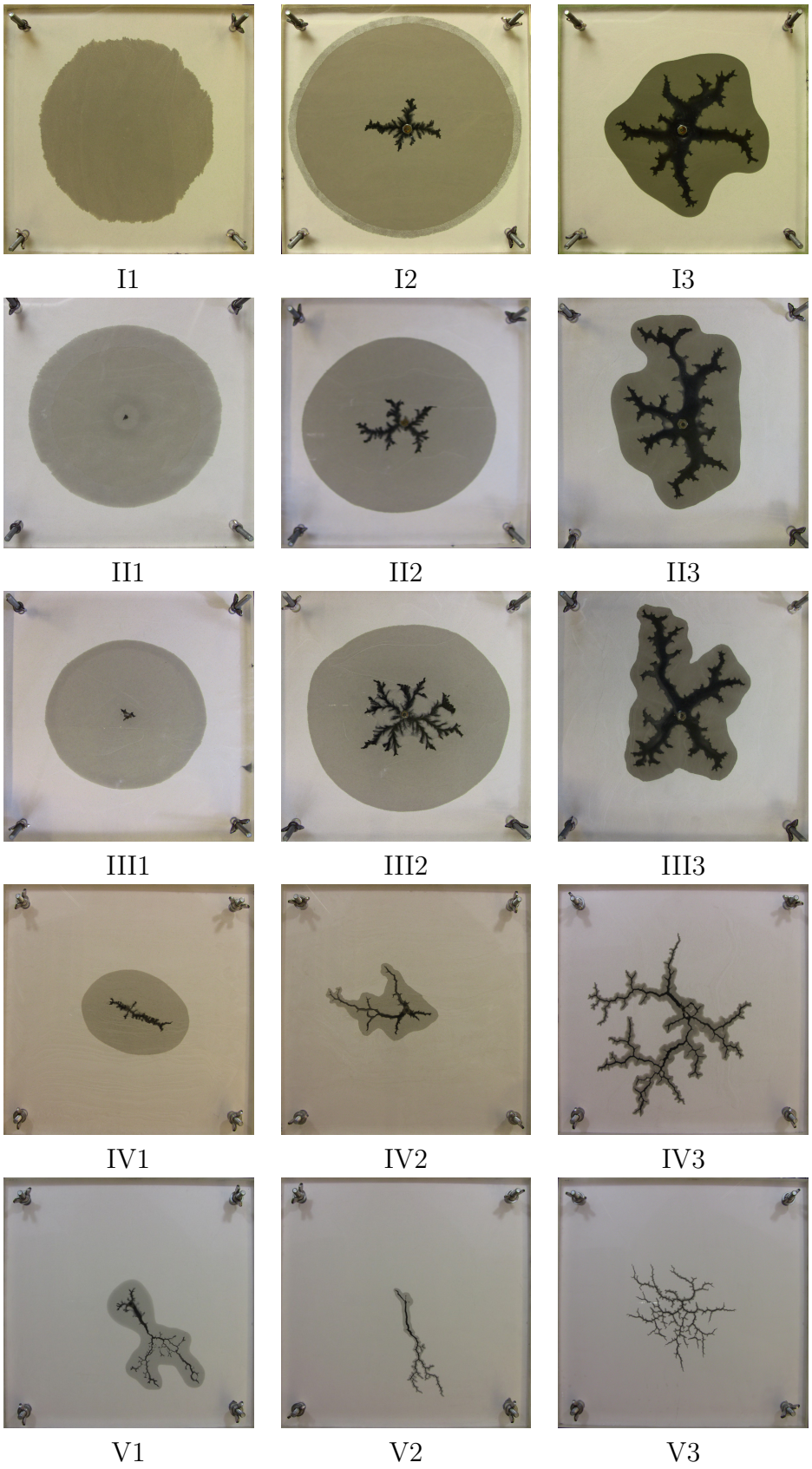

Figure 6: Grain displacement pattern at the end of injection.

Table 2: Test parameters of selected injection tests.

Test Parameters	$\eta = 5$ cp $v = 0.829$ cm/s	$\eta = 5$ cp $v = 8.29$ cm/s	$\eta = 176$ cp $v = 8.29$ cm/s
SF0/100	I1	I2	I3
SF10/90	II1	II2	II3
SF20/80	III1	III2	III3
SF40/60	IV1	IV2	IV3
SF100/0	V1	V2	V3

2.5 Characterization of displacement regimes

2.5.1 Characterization based on λ and τ_1

A similar assessment as is done in [41] is performed to examine whether the grain displacements in sand and silica flour mixtures are still governed by the dimensionless parameter τ_1. The grain displacements can be analyzed with an area ratio λ_t, which is the ratio of fingering area A_f and leakoff area A_l, $\lambda_t = A_f/A_l$. The larger the area ratio indicates the more fingering growth. Evolution of λ_t during the injection test is shown in Figure 7. The λ_t fluctuates at the early time, however, as the injection continues, the growth becomes nearly steady state. Therefore, the averaged late time area ratio λ is used as an index to measure the efficiency in creating the fluid channels in this work.

In Huang et al. [41], the characterization is achieved by analyzing the relation between τ_1 and the averaged late time area ratio λ. $\lambda - \tau_1$ relation of the mixtures are plotted in Figure 8. The experimental data from different fine contents deviate from injection tests in a pure sand matrix, and the deviation is more noticeable if the mixture contains a higher fine content. At the same τ_1, the larger the fine content, the more restrained growth of the fingers (smaller λ) is observed. Nevertheless, some common transition can still be captured. When $\tau_1 < \tau_0\,(\tau_0 \simeq 0.001)$, the grain displacement is also negligible (Test I1, II1, and III1). Although the experimental results seem scattered in Figure 8, the semi-logarithmic relationship appears to exist

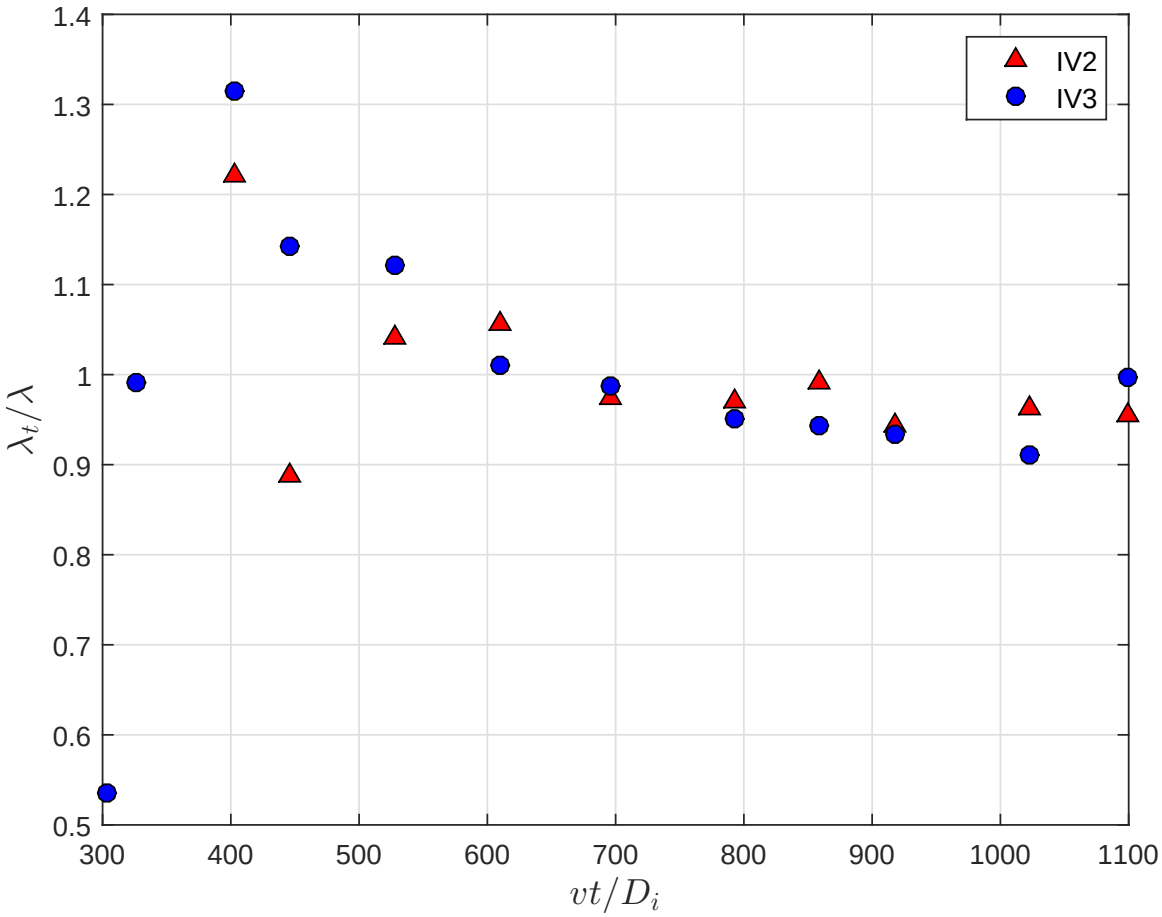

Figure 7: Normalized area ratio λ_t/λ for Test IV2 and IV3, where λ is the averaged late time area ratio.

before the plateau when $\lambda \simeq 45\,\%$.

It is rather challenging to conduct injection experiments with pure silica. Three dimensional effect potentially exists across the gap. For F110 sand, it is about 15 particles spanning a gap size of 1.575 mm. In contrast, the number of silica particles is about 40 spanning a gap size of 0.787 mm, thereby three dimensional channels may be created so that traces of the fingers on the surfaces are not clearly visible. An example is Test V3 where some internal fractures at the sub-pixel scale are hard to capture from the image. One solution is to use a further reduced gap size, however, it is not ideal due to the issues of potential deflection and imperfectly aligned surfaces of the plates. To overcome this situation, a modified image processing approach is

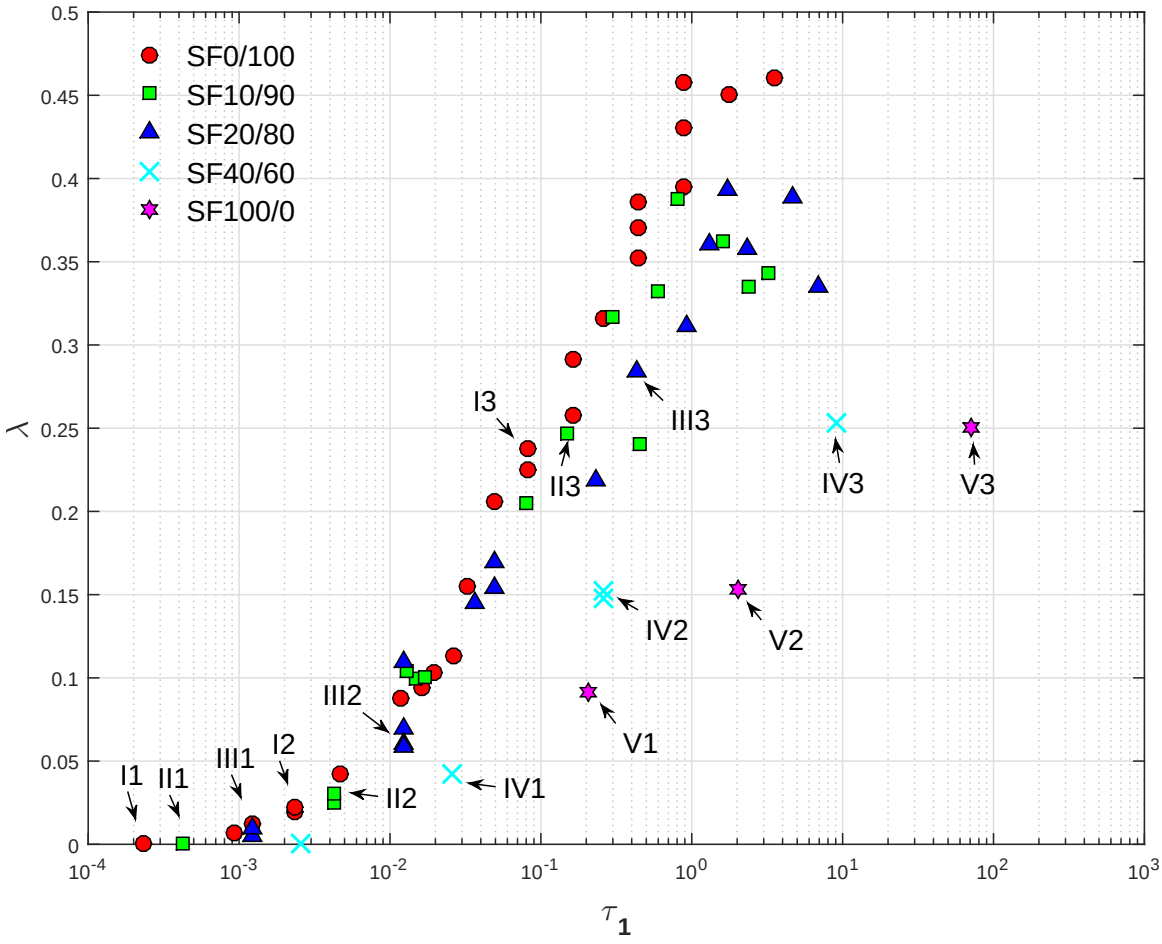

Figure 8: The averaged late time area ratio λ versus τ_1.

applied to recover the sub-pixel features of the fingers.

Test case V3 was conducted with 90 % aqueous glycerin solution injected into 100 % silica silt at a rate of 25 ml/min. The image did not clearly show the geometrical details of the fingers. To recover the information, a skeleton algorithm is used since the elongated leakoff area shape indicates the fingering location. The skeleton method is the morphological operation which uses the iterative thinning algorithm [34, 98]. The corresponding result increases the average late area ratio λ from 0.19 to 0.25. The extrapolation has negligible influence on the fractal dimension (1.2287 for skeleton only, 1.2978 for gray scale only, and 1.2857 for the combined image). From Figure 10, the hidden channels can be recovered assuming one pixel in width. Indeed, the

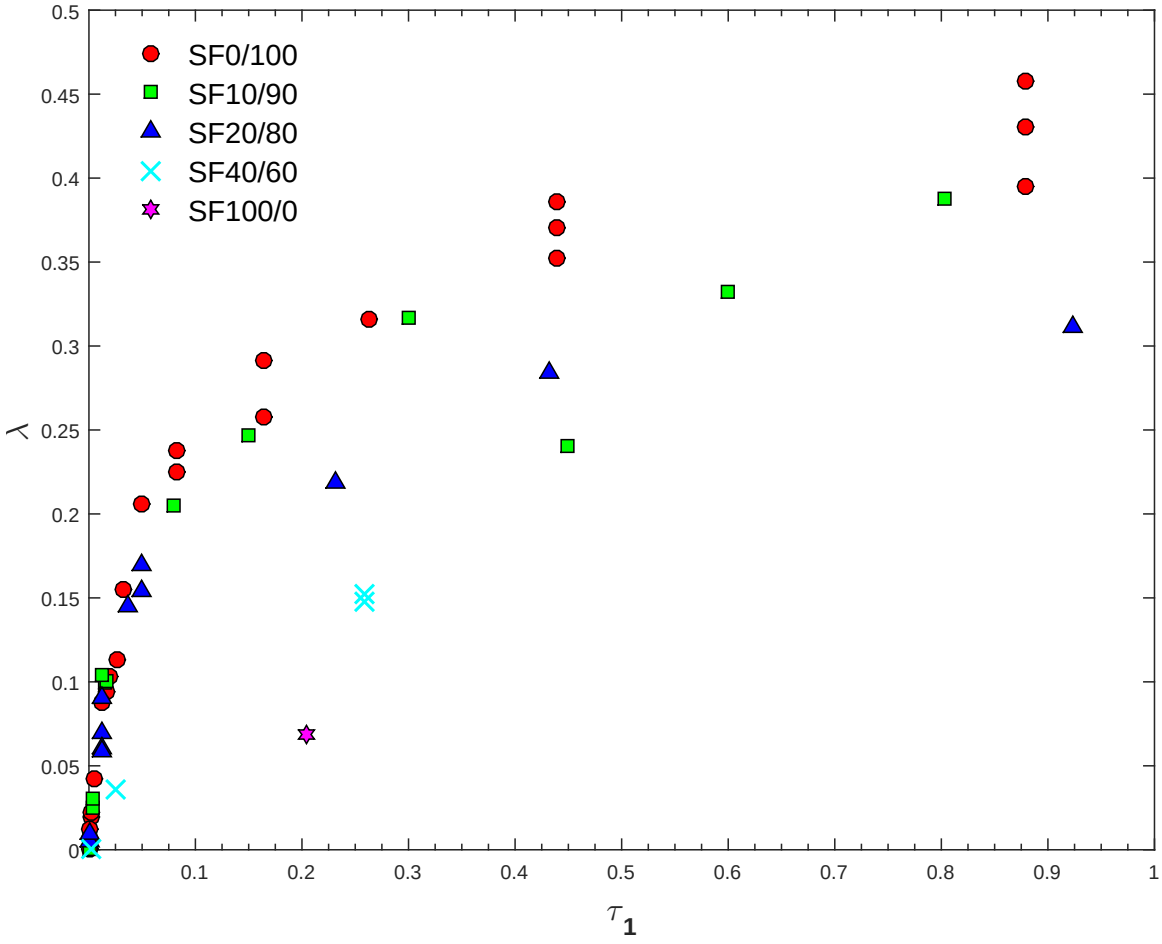

Figure 9: The averaged late time area ratio λ at small τ_1.

one pixel width assumption could overestimate the finger width. For a more accurate result, both higher resolution images and even smaller the gap size (if out-of-plate deflection of the Hele-Shaw cell is constrained perfectly) should be considered.

2.5.2 Morphological difference

The capillary effect leads to the differences in the signature of fingers. A closer look at the geometrical difference among the displacement patterns (see Figure 11 and Table 3 for test parameters) shows that as the fine content increases, the side-walls are smoother, and the sharp finger tips resemble that of a brittle crack. These geometric characteristics can be identified with the assessment of a fractal dimension D [66]. The fractal dimension of the fluid channels is analyzed, and the results are presented

(a)

(b)

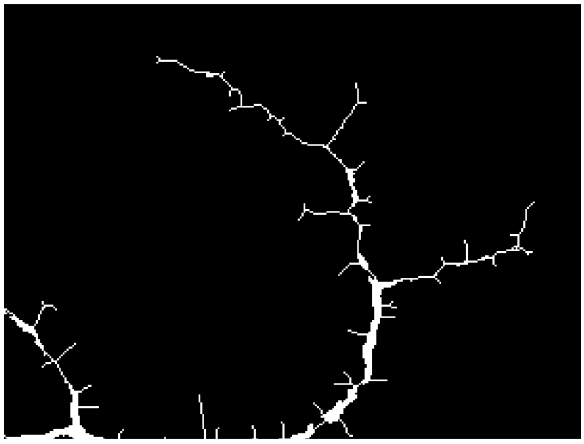

(c)

Figure 10: Image recovery using the skeleton method. Image taken from Test V3 at $t = 5.53$ s. (a) Experimental observation, (b) finger identification without enhancement, and (c) finger identification with enhancement.

Table 3: Test parameters for some additional tests.

Test case	Soil type	η (cp)	v (cm/s)
I4	SF0/100	942	41.4
III4	SF20/80	942	16.6
IV0	SF40/60	5	0.083

in Figure 12 and find that it decreases as increase in the fine content. For instance, the fractal dimension of the fingers in pure silica flour is almost close to 1 indicating sharp straight fractures. Moreover, from Figure 15, Tests II3, III3, IV3, and V3 share nearly the same area ratio of $\lambda = 0.25$, while the fractal dimensions are 1.62, 1.61, 1.46, and 1.30 respectively. A possible explanation is that the surface tension reduces the particle rotation/sliding (shear failure) to cause the fingers to become more brittle crack like.

2.5.3 Capillary effect τ_3

Capillary effect is neglected in the dimensionless number τ_1. However, such an effect may be non-negligible for the low permeability mixtures. The question is when the effect of low permeability comes in, how the corresponding capillary effect affects the fluid-grain displacement patterns. The near-wellbore capillary number can be calculated as $Ca = 6.5 \times 10^{-4}$ for the test series where $v = 0.829$ cm/s with $\eta = 5$ cp, $Ca = 6.1 \times 10^{-3}$ for the test series where $v = 8.29$ cm/s with $\eta = 5$ cp, and $Ca = 2.1 \times 10^{-1}$ for the test series where $v = 8.29$ cm/s with $\eta = 176$ cp. The large capillary number demonstrates the limited effect of the surface tension near the wellbore. However, such definition of Ca does not consider the matrix permeability and the decrease in infiltration-front velocity as the injection continues. Local Ca could become rather low as the infiltration front grows. Since grain displacement is also involved in this coupled process, to account for both the capillary effect and the deformability of the medium, an additional dimensionless number τ_3 could take the

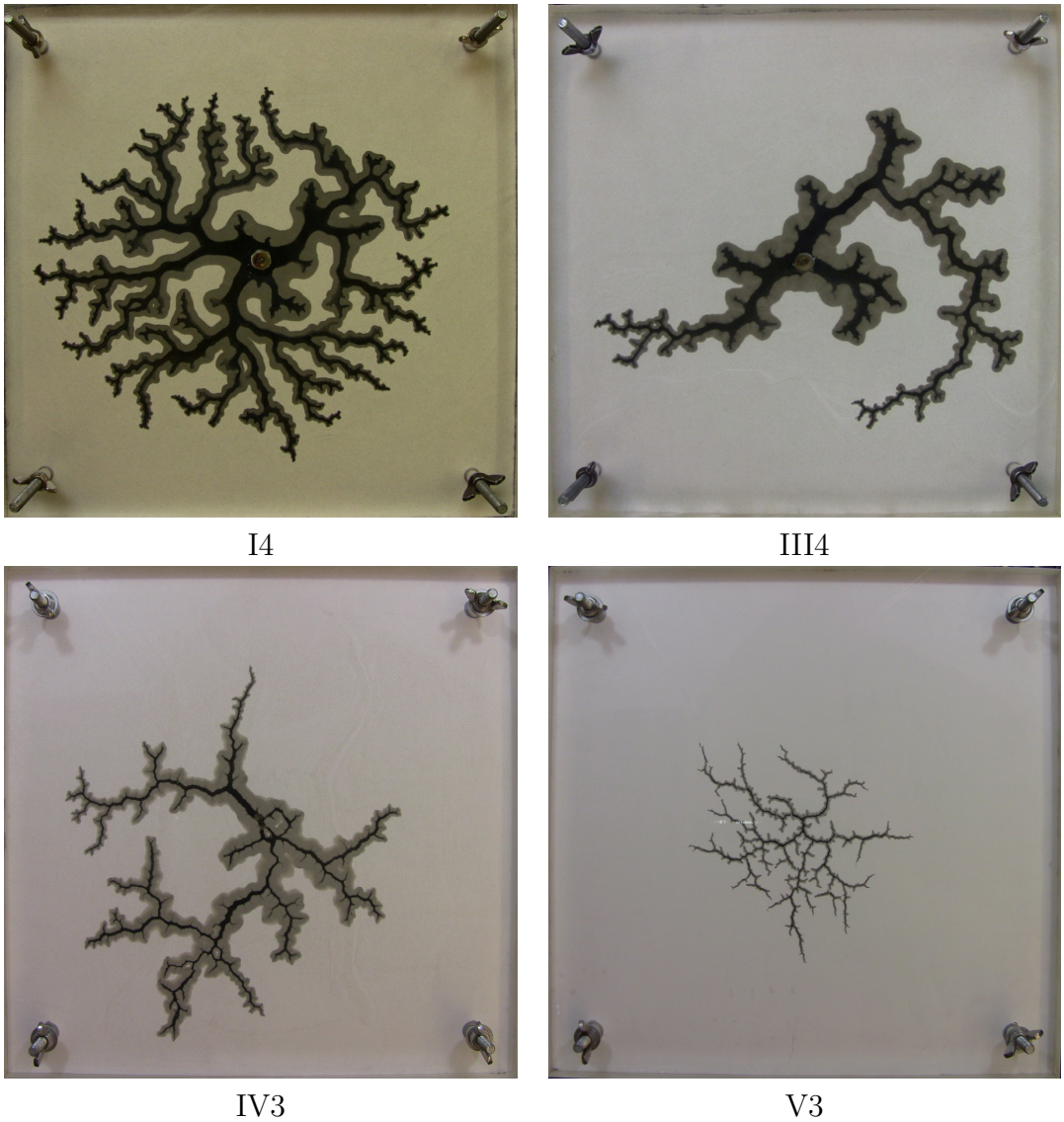

Figure 11: Morphological difference in fluid-grain displacement patterns.

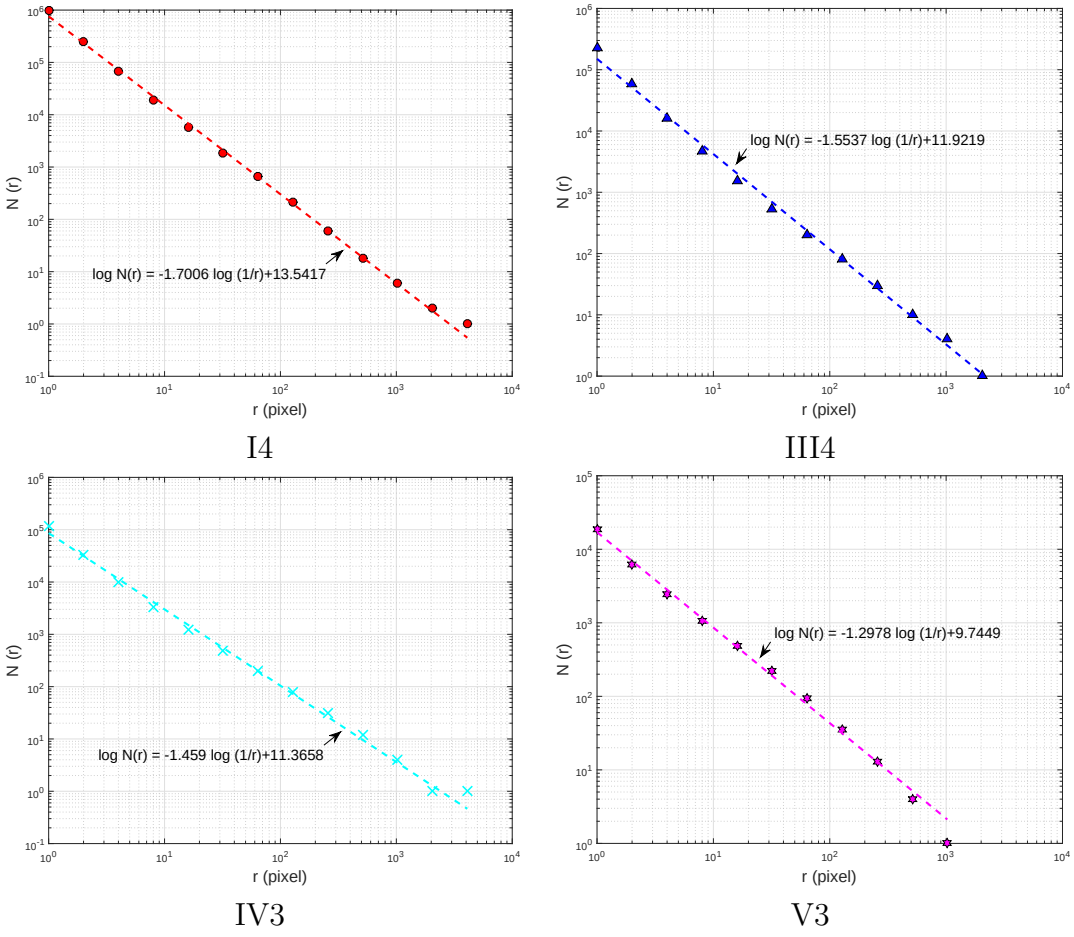

Figure 12: Fractal dimension of the fluid channels in Test I4, III4, IV3, and V3.

form of

$$\tau_3 = \frac{\gamma \cos\theta}{E\sqrt{k}}, \tag{2}$$

where θ is the fluid-solid contact angle, and $\sqrt{k}$ is a characteristic length scale for the pore structure. To explain the physical meaning of τ_3, we can rewrite τ_3 in the form of $\tau_3 \sim \delta p_c/E$, where the capillary pressure $\delta p_c \sim \gamma \cos\theta/\sqrt{k}$. Therefore, τ_3 describes the effect of capillary pressure δp_c over the mixture deformability. Regarding the choice of the deformability reference, it is noted that in [37], the stiffness of the matrix is described by the grain-plate interfacial friction. However, the elastic deformation of the granular structure is not considered. Furthermore, without the out-of-plate confining stress, the grain-plate interfacial friction is negligible [48]. Therefore, the soil modulus is used as the deformability index property in this context. Depending on the contact angle the capillary pressure will either be positive (promoting infiltration) or negative (hampering infiltration). For simplicity, the contact angle is assumed as $\theta = 0°$, which indicates an ideal case of perfect hydrophilic interface. Additional information about the contact angle between quartz and water/glycerin can be found in [85]. Trojer et al. [91] also discussed the transition from drainage to imbibition when the contact angle increases from 0 to 120°.

In case of fluid flow in low-permeability media, the wellbore pressure δp depends on the viscous pressure δp_v and the capillary pressure δp_c (see Figure 13). At a constant rate, $\delta p_v = \text{const}$ for both cases. If the invading fluid is air and the displaced pore fluid is liquid, the wellbore pressure can be written as $\delta p_1 = \delta p_v + \delta p_c$. The additional wellbore pressure due to capillary pressure induces the grain movements and leads to the creation of capillary fractures [37]. On the other hand, in the case of liquid displacing air, the negative capillary pressure at the infiltration front reduces the wellbore pressure, i.e., $\delta p_2 = \delta p_v - \delta p_c$. Therefore the reduction in the wellbore pressure results in the grain movements restraint. Recalling Darcy's law $v = k/\eta \nabla p_v$, δp_v can be given as $\delta p_v \sim v\eta l/k$, and thereby rewrite τ_1 as $\tau_1 \sim \delta p_v/E$, suggesting

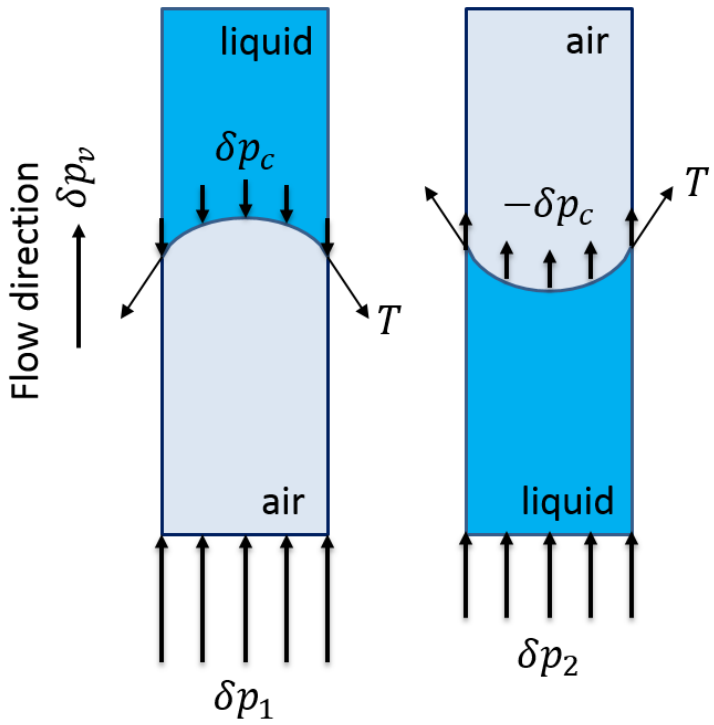

$$\delta p_v = \delta p_1 - \delta p_c = \delta p_2 - (-\delta p_c)$$

$$\delta p_2 < \delta p_v < \delta p_1$$

Figure 13: Schematic relationship between the injection pressure and the capillary pressure during fluid invasion.

that τ_1 is the characteristic number to interpret the effect of viscous pressure δp_v on the matrix deformability.

Therefore, the grain displacement patterns can now be characterized by τ_1 and τ_3 in terms of viscous pressure and the capillary pressure effect on the granular medium deformability. At low τ_3, because the capillary effect is negligible, the wellbore pressure is insensitive to the capillary effect, i.e., the grain movements are mainly characterized by τ_1. As τ_3 increases (e.g., permeability decreases), the capillary effect becomes non-negligible so that the wellbore pressure decreases and grain movements are restrained.

The next step is the identification of critical τ_1 values to define the boundaries. As

suggested in Huang et al. [41], the grain displacement regimes are recognized by τ_0, τ_d, and τ_r ($0 < \tau_0 < \tau_d < \tau_r$), which are the boundaries dividing four regimes of grain displacement patterns. When $\tau_1 < \tau_0$, the growth of granular fingers is negligible so that the pattern remains in the simple radial flow regime and corresponds to $\lambda \to 0$. In the case of extremely large τ_1 ($\tau_1 > \tau_r$), the area ratio λ remains constant at $\lambda \simeq 45\,\%$ as τ_1 increases. When $\tau_1 < \tau_d$, it is observed that λ grows linearly with τ_1 until $\tau_1 = \tau_d$.

The determination of τ_0 is mostly based on the observation of λ. As stated above, τ_0 is recognized when $\lambda \to 0$, and thereby $\lambda \leqslant 0.001$ is defined as our criteria to determine the boundary of τ_0. Similarly, τ_r is also determined by the observation when λ reaches a plateau. Based on the trend of pure silica flour, λ may reach a plateau when τ_1 reaches o(10^5). However, conducting these tests with large τ_1 in laboratory experiments is impractical, and thereby an estimation of τ_r is provided from semi-logarithmic relationship in $\lambda - \tau_1$ curve (Figure 8). For the determination of τ_d, the linear plot at small τ_1 is provided in Figure 9. For Test I, II, and III series, the growth is almost identical, and the linearity ends around $\lambda \simeq$0.1 while $\tau_1 \simeq 0.02$. For higher fine contents (Test IV and V series), it is difficult to say whether the growth of λ is linear. However, if exists, the slopes are clearly flatter than those with low fine content (Test I, II, and III series). The challenge in conducting lab tests requires an alternative approach to determine τ_0, τ_d, and τ_r. As stated in 2.5.1, a semi-logarithmic relation between λ and τ_1 can be observed between τ_0 and τ_r.

Based on these statements, semi-log curve fitting for each test series is provided in Figure 14. The curve fitting is conducted by ignoring data points where $\lambda \leqslant 0.001$ in consideration of $\tau_1 > \tau_0$. The intercept when $\lambda = 0$ can be regarded as τ_0. For determination of τ_d, the linear growth ends $\lambda \simeq 0.1$, where $\tau_d \simeq 0.02$ from the the corresponding linear λ growth from Test I, II and III. If τ_d is same for all test series, λ for 40 % silica content is roughly 0.03 (see Figure 9) and probably be even

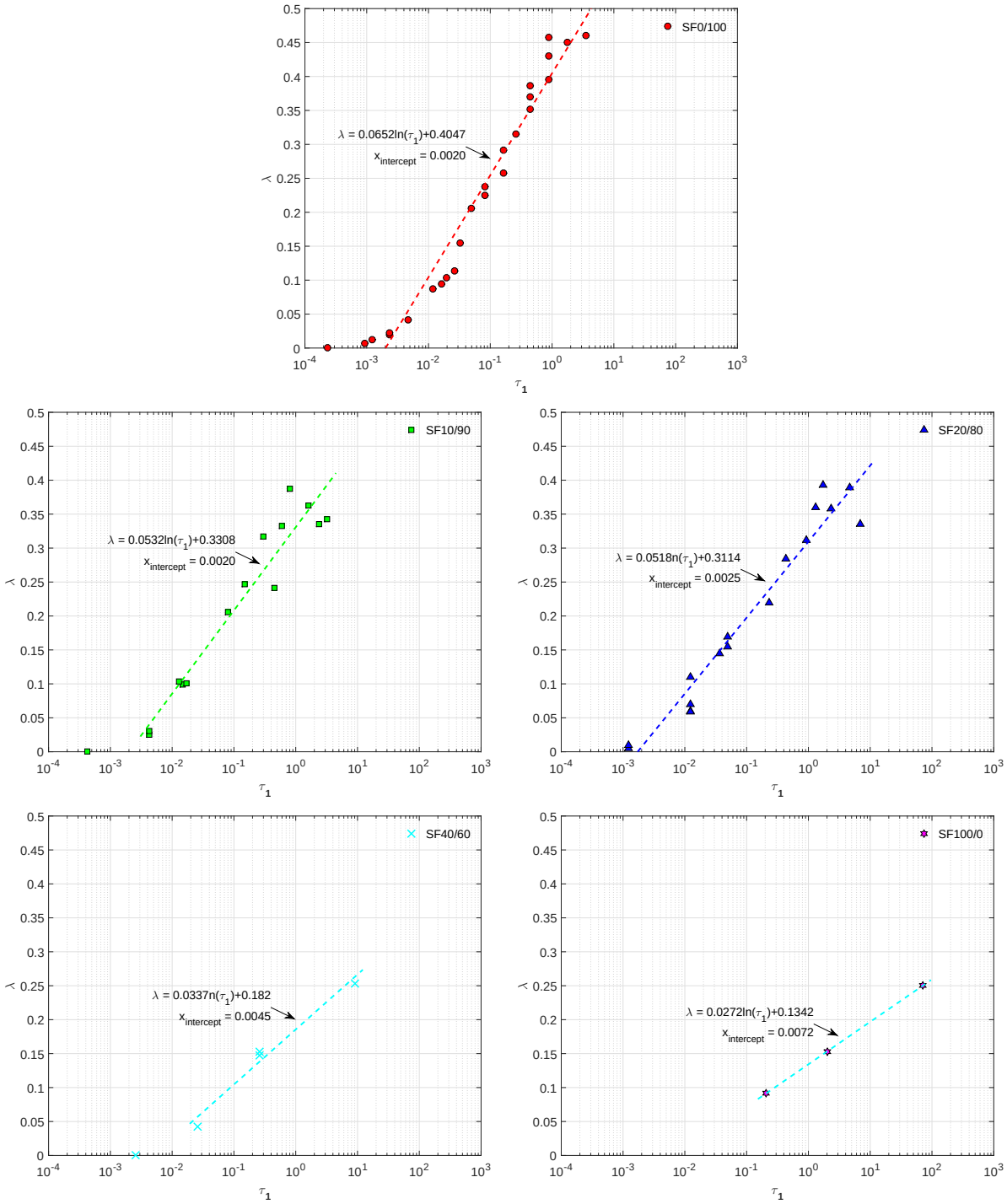

Figure 14: Semi-logarithmic regression of $\lambda - \tau_1$ relation for each mixture of Ottawa F110 sand and silica flour. $x_{intercept}$ indicates the τ_0 of soil.

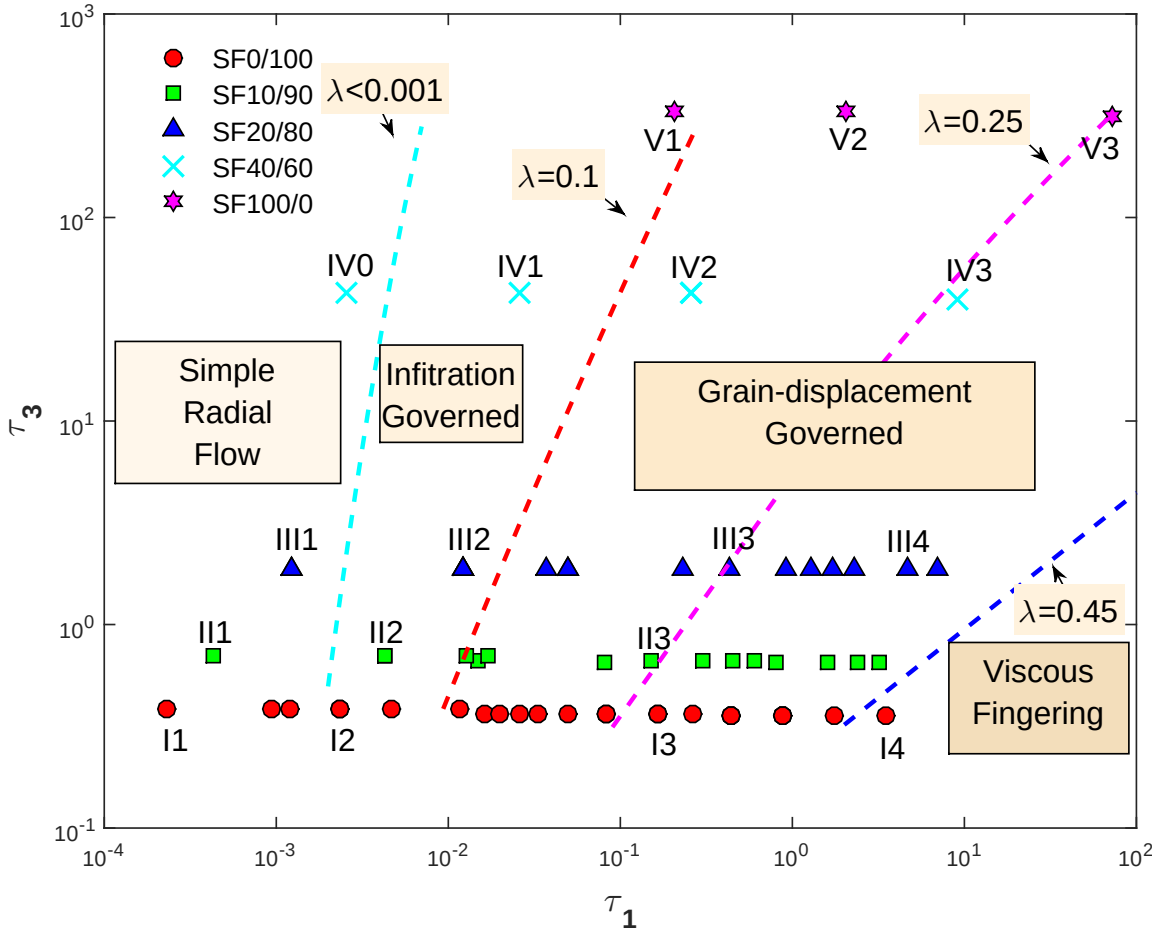

Figure 15: Phase diagram based on τ_1 and τ_3 with showing boundaries. The dotted lines are iso-lines for the area ratio λ.

smaller for Test V series. τ_1 at $\lambda = 0.1$ is chosen to define the boundary of the infiltration governed regime and grain-displacement governed regime. Similarly, τ_r is defined as τ_1 at $\lambda = 0.45$. Therefore, for each test series, the boundaries τ_0, τ_d, and τ_r can be determined as the interceptions of the semi-logarithmic curve when $\lambda = 0$, $\lambda = 0.1$, and $\lambda = 0.45$, respectively. The overall phase diagram based on τ_1 and τ_3 is shown in Figure 15 with the calculated boundaries. Notably, τ_3 divides the displacement regimes based on silica content. At the same averaged late time area ratio λ, the greater τ_3 culminates greater τ_1 indicating more injection energy is needed to generate the same degree of grain movements. Furthermore, the inclined boundary indicates that as the permeability of the matrix decreases, the capillary

effect restrains the grain movement and promotes the fluid infiltration. For instance, Test IV0 (injection condition is provided in Table 3) and Test I2 have almost the same τ_1, but the displacement pattern is entirely different (compare Figure 16 with Figure 6). Test IV0 is in the simple radial flow regime, and Test I2 is in the infiltration governed regime. This gives an example that the determined boundary determined from the aforementioned method can separate these two regimes.

2.6 Conclusions

A series of injection experiments is performed with mixtures of sand and silica flour. As the weight percentage of the silica flour increases, the matrix permeability decreases significantly and the capillary effect becomes non-negligible. The capillary effect at low permeability restrains the grain movements and promotes the fluid infiltration. Results also show a variation in fractal dimension of the fingering geometry suggesting the surface tension at low permeability probably restrains grain rotational and sliding movements. An additional dimensionless number τ_3 incorporating surface tension is derived to characterize the fluid-grain displacement. A methodology for classifying the fluid-grain displacement patterns based on two dimensionless numbers is suggested.

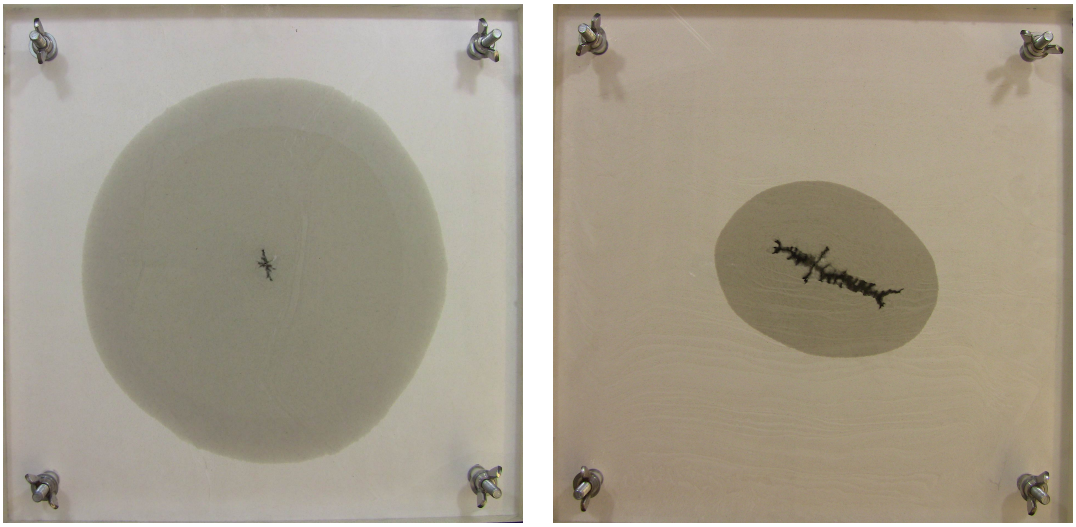

IV0

IV1

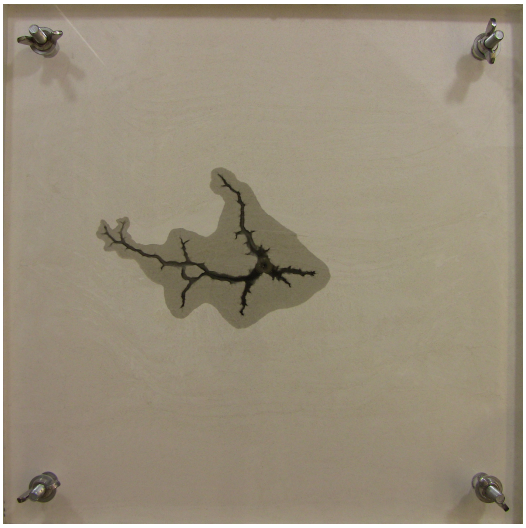

IV2

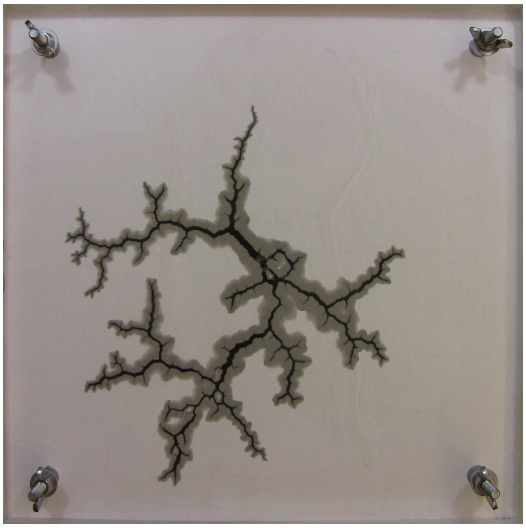

IV3

Figure 16: Additional fluid-grain displacement patterns for injection experiments with the mixture containing 40 % fine content.

CHAPTER III

EFFECT OF NON-NEWTONIAN RHEOLOGY ON FLUID INJECTION INTO DENSE GRANULAR MEDIA

3.1 Introduction

Injection of non-Newtonian fluids in the subsurface is employed in many engineering applications. Cross-linked polymers and viscoelastic surfactant based fluids used in reservoir stimulation or flooding for enhanced oil recovery are of non-Newtonian rheology [25]. Viscoelastic surfactant based fluids are also commonly employed in environmental remediation for DNAPL (Dense Non-Aqueous Phase Liquid) [79]. In drill cuttings reinjection as well as grouting for ground improvement, the rheology of the slurry is also non-Newtonian. In the fluid injection process, the non-Newtonian fluid rheology affects not only the fluid flow response in the porous media but also the mechanical behaviors. Therefore, better understanding of the rheological effects can help design fluids and the injection process to achieve the desired goals.

Laboratory injection experiments with sand in triaxial cells have been conducted to investigate the fracturing process or fluid-grain displacement mechanisms in unconsolidated sand formations [9, 12, 29, 30, 44, 52, 53] (see also references in [96]). Fluid rheology was observed to have a strong influence on the fracturing behaviors. Compared with the cases using Viscasil oil 500, a viscous Newtonian fluid, when fractures were induced using cross-linked gels or bentonite slurry, the fracture paths are relatively straight and the side walls of the fractures are smooth [9].

Similar observations were also obtained in the fluid injection experiments performed using a Hele-Shaw cell like configuration [40, 41]. The experimental setup consists of two transparent acrylic plates set apart with a gap size b. Dry Ottawa

F110 sand is filled in between the two plates to form dense packing with a porosity about $\phi = 0.35$. During the tests, the test cell is placed horizontally and the testing fluid is injected from the center of the bottom plate. The outer boundary is sealed with masking tape. Both the fluid rheology and the injection rate were varied. As shown in Figure 17, at the same injection rate ($Q = 50$ ml/min) and the gap size ($b = 1.575\,\text{mm}$), the openings created using the 0.5 % and 1 % aqueous polyacrylamide (PAAM) solutions are much narrower than those using a 90 % or 100 % aqueous glycerin solution. The sidewalls are smoother and the sharp tips in Figure 17c and Figure 17d resemble that of a brittle crack. Also, the leakoff or infiltration area in the polyacrylamide injection experiments is notably larger than the area of the fluid channels created by the glycerin solutions.

Flow curves of the aqueous polyacrylamide solutions at various concentrations by weight are shown in Figure 18. The polyacrylamide solutions show strong shear thinning behaviors. Normalizing the injection rate Q with respect to the diameter D_i of the injection inlet ($D_i = 1.016$ mm) at a gap size b of 1.575 mm of the test cell yields a nominal shear rate between the two plates, $\dot{\gamma} \simeq 10^5\ \text{s}^{-1}$, near the injection point. The shear rate at the pore scale will be even higher considering the pore size. At such high shear rates, viscosity of the 1 % polyacrylamide solution is approximately 1 cp, similar to that of water at a temperature of 21 °C. As the injection front grows during the infiltration process, the decrease in the infiltration speed at the front could lead to substantial increase in the viscosity. At a shear rate about $\dot{\gamma} \simeq 1$, the 1 % solution has a similar apparent viscosity to the viscosity of pure glycerin at 942 cp, while the 0.5 % solution has a similar apparent viscosity to the 90 % of the aqueous glycerin solution. If the shear rate decreases further, the viscosity of the PAAM solutions will increase even further.

As shown through the experiments in [41, 40], increase in the injection rate and viscosity of a Newtonian fluid or the polymer concentration results in the fluid flow

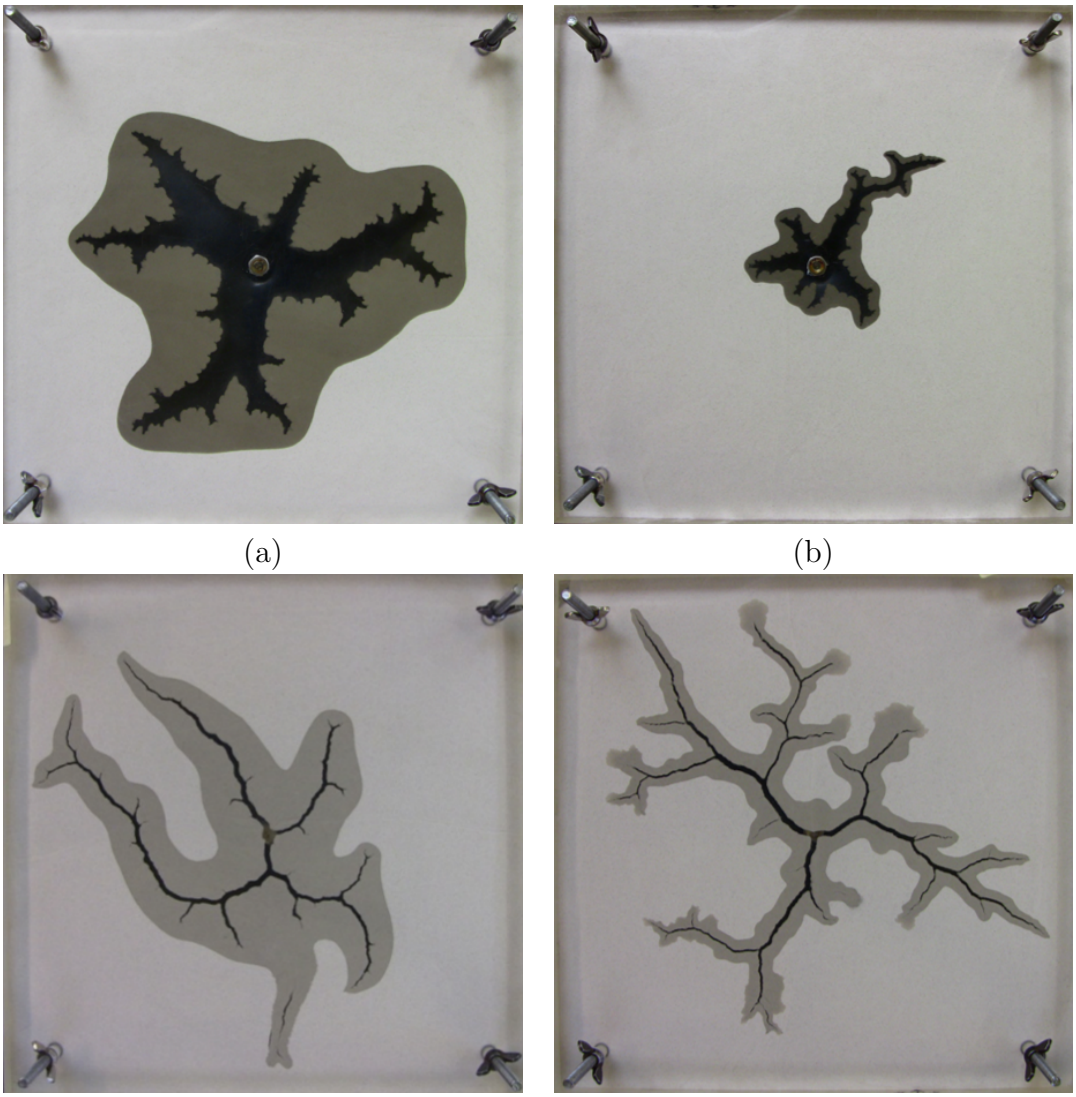

Figure 17: Displacement patterns from the injection experiments in a Hele-Shaw cell like configuration with dry Ottawa F110 sand in dense packing; (a) 90 % aqueous glycerin solution, (b) 100 % aqueous glycerin solution, (c) 0.5 % polyacrylamide solution, and (d) 0.5 % polyacrylamide solution; the black areas are the fluid-only areas; the dark gray and the light gray areas are the infiltrated and the dry areas, respectively [41, 40].

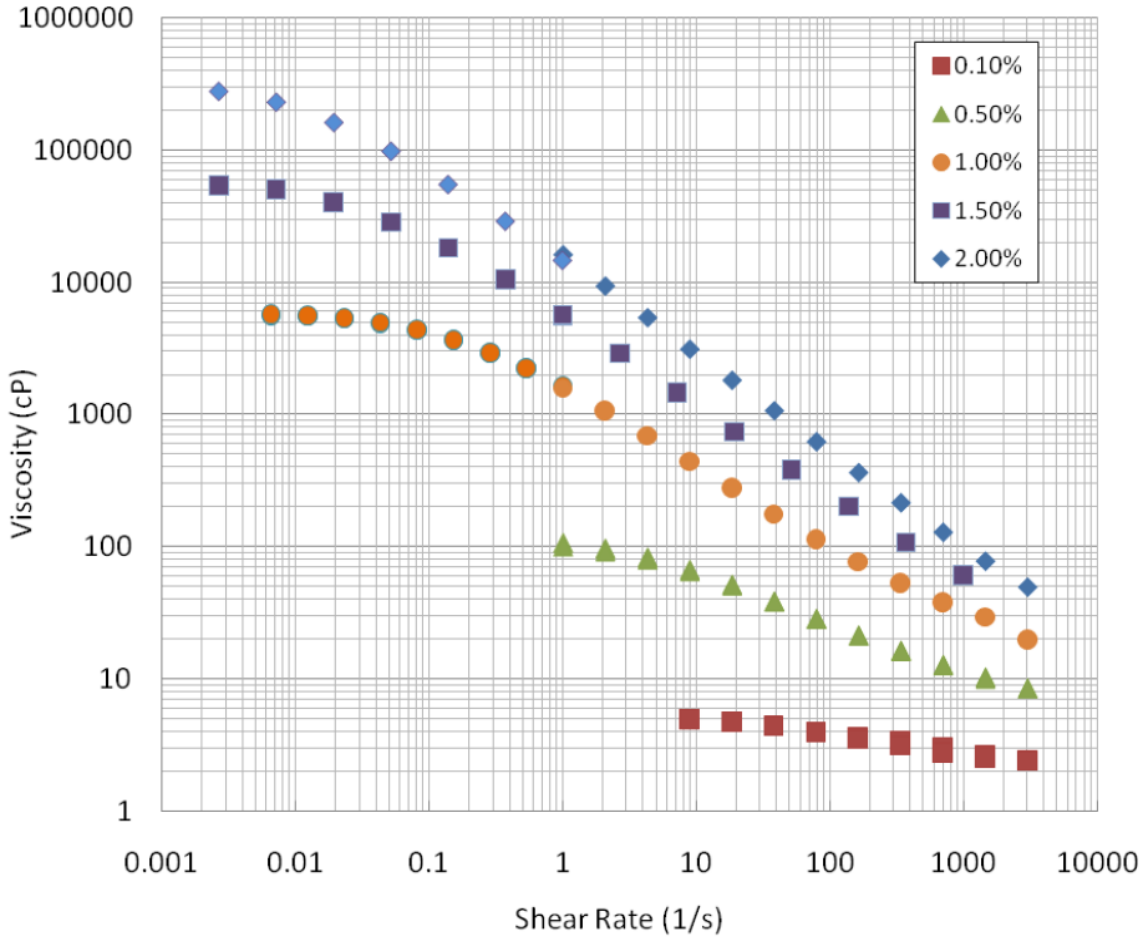

Figure 18: Flow curves of the aqueous polyacrylamide solutions at various concentrations by weight [40].

behaviors to change from infiltration-governed to infiltration-limited. Meanwhile, the granular medium behaviors display a transition from that of a rigid porous medium to localized failure characterized by the growth of fractures or fluid channels.

For a complex fluid, the rheological signatures may include shear thinning, zero shear viscosity, yield stress, thixotropy, viscoelasticity, etc. These rheological features in general are intertwined. In addition to fluid rheology, behaviors of flow in porous media may be further affected by the multi-phase characteristics of the fluids in that both external and internal filter cakes may develop. Therefore, a single rheological feature such as shear thinning alone may not be sufficient to explain the differences in the opening patterns in Figure 17. Nevertheless, it is important to understand how

and when a certain rheological signature plays a critical role.

A unique benefit of numerical analysis is that the effect of rheology can be explored by isolating the rheological characteristics. In this work, the effect of shear thinning rheology on the fluid injection process in an initially dry dense granular medium is investigated numerically using the discrete element method (DEM) code PFC2D® coupled with a pore network model. It extends the previous work by Zhang et al. [96] So that the shear thinning rheology is taken into account. The algorithm in [96] is also improved by incorporating iteration in the pore network to enhance the quasi-steady state fluid flow scheme.

The chapter is structured as follows: Section 3.2 introduces the DEM-pore-network coupled model and then presents implementation of the shear thinning rheology. Improvement in the quasi-steady state fluid flow scheme is illustrated next. Section 3.3 describes the model setup and the fluid rheology model studied in this work. The shear thinning rheology as well as the injection rate effect are discussed in Section 3.4. In Section 3.5, a characteristic viscosity for the injection process is defined and its effect to near-wellbore behavior is discussed.

3.2 Numerical methodology

3.2.1 DEM-pore network coupled model

The advantage of DEM is that with an explicit solution scheme (Newton's second law [45]), the macro-scale mechanical response emerges from the interaction of particles through their contacts at the micro-scale. Meanwhile, pore network models have been widely used to to directly model fluid flow process in pore scales [8, 26]. The pore network can be constructed by identifying the domains formed from close chains of particles as the pores paces. Fluid flow between two adjacent pore spaces takes place through the flow path or pore throat (see Figure 19(a)). The fluid flow inside the flow path is following the Hagen-Poiseuille equation. Details of the numerical

scheme to model the injection process with a Newtonian fluid can be found in [96, 97] and references therein. The numerical scheme, which extends the network coupling approach in [45], differs from previous work dealing with fully saturated condition and bonded particles, e.g., [1, 61, 87, 90, 99], where the solid skeleton is relatively stiff and the pore network structure does not need significant update during simulations. The benefit of the scheme used in this work is that the configuration of the pore structure is updated to allow pore spaces to merge and split as the particle assembly configuration evolves. Since we intend to simulate fluid injection into an initially dry medium, calculation of fluid infiltration is also implemented in the coupling scheme before the fluid flow calculation of pressure diffusion at each fluid time step. Hydro-mechanical coupling is realized by data exchanging at predetermined time steps between the mechanical calculation and fluid calculation cycles. For each particle, a resultant drag force $\boldsymbol{F}_{fluid}$, obtained from summing up the pore pressure over the particle surface (see Figure 19(b)), is passed from the fluid calculation to the mechanical calculation. The resultant drag force $\boldsymbol{F}_{fluid}$ is then applied to each particle in addition to the unbalanced force resulted from the mechanical contact forces. The hydro-mechanical coupling is reflected in the change in the aperture of a flow path due to mechanical deformation and the addition of the drag forces to the particles.

3.2.2 Contact and aperture

Given the geometrical configuration of a particle assembly, the macroscale mechanical properties are governed by the microscale contact model. Here the contact law for the particles is assumed to be linearly elastic and frictional, characterized by the normal and shear stiffness, k_n and k_s, and the friction coefficient μ of the particles. Parameters for the contact model, the mean particle radius $\bar{R}$ and the density ρ_s of the particles are listed in Table 4. In this study, the particle assembly is generated randomly using the radius expansion scheme [81] with the radii of the particles uniformly distributed

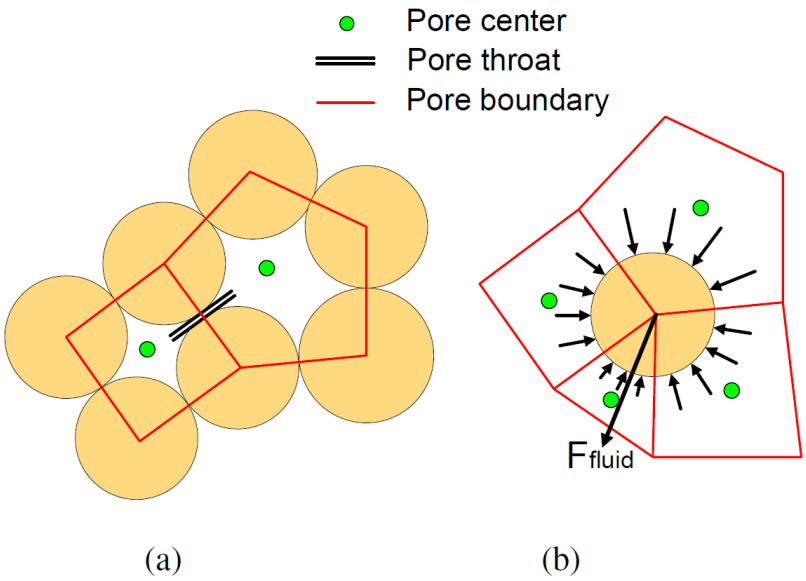

Figure 19: Schematics showing (a) pore spaces formed from close chains of particles and (b) the drag force $\boldsymbol{F}_{fluid}$ as a resultant from the surrounding pore pressure [96].

Table 4: Parameters for the particle assembly

$\bar{R}$	ρ_s	$k_n = k_s$	μ
0.6 mm	2650 kg/m^3	83.3 MN/m	0.577

in the range from 0.5 to 0.7 mm. A biaxial compression test at a confining stress $\sigma_0 = 0.5$ MPa yields the 2D secant modulus and the Poisson's ratio at 50 % of the peak stress to be $E'_{50} = 34.13$ MPa and $\nu'_{50} = 0.222$. At the same confining stress, assuming a Mohr-Coulomb failure criterion, i.e., $\sigma_1 = (1+\sin\varphi)/(1-\sin\varphi)\,\sigma_3$, where σ_1 is the axial peak stress, the apparent peak friction angle of the particle assembly is $\varphi = 25.7°$.

In addition to the particle assembly configuration, apertures of the flow paths also affect the permeability of the assembly. The aperture model adopted in the study can be expressed as follows [61],

$$a = \begin{cases} \dfrac{a_0\delta_0}{\delta_n + \delta_0} & \text{if} \quad \delta_n > 0 \\ a_0 - \lambda\delta_n & \quad\ \ \delta_n \leq 0 \end{cases}, \tag{3}$$

where a_0 is the residual aperture; δ_n is the overlap between two particles ($\delta_n \leq 0$ indicating a gap); δ_0 is a reference value and λ is a multiplier. The residual aperture a_0 is introduced here so that fluid flow can occur in 2D when there is an overlap at the contact. The microscale parameters in the aperture model are chosen to be $a_0/\bar{R} = 0.5$, $\delta_0/\bar{R} = 0.272$, and $\lambda = 1.2$ so that, for a particle assembly with $\bar{R} = 0.6$ mm and subjected to a mean stress of the order of 0.1 MPa, the macroscale permeability obeys the Kozeny-Carman correlation [96],

$$k = \frac{1}{180} \frac{d_p^2 \phi^3}{(1-\phi)^2}, \tag{4}$$

where d_p is the average particle diameter and ϕ is the assembly porosity.

Note that, in this scheme in evaluating the pore volume, the 2D porosity ϕ_{2D} is converted into a 3D porosity ϕ approximately through linear interpolation, using the limits associated with the maximum (hexagonal) and minimum (square or cubic) packing density states for mono-sized packing of disks (2D) and spheres (3D) [96]. The 2D porosity at a mean stress level of $\sigma_0 = 0.5$ MPa is $\phi_{2D} = 0.143$, which corresponds to $\phi = 0.35$. The permeability obtained from the Kozeny-Carman correlation is $k = 8.49 \times 10^{-10}$ m^2.

3.2.3 Implementation of fluid rheology

A power law fluid can be described by,

$$\tau = K\dot{\gamma}^n, \tag{5}$$

where τ and $\dot{\gamma}$ are the shear stress and shear strain rate and n and K are the power law index and the consistency index, respectively. The modified Hagen-Poisuille equation is employed to describe fluid flow through the flow path, namely,

$$q = \frac{n}{2n+1} \left(\frac{a}{2}\right)^{\frac{n+1}{n}} \left(\frac{|\nabla p|}{K}\right)^{\frac{1}{n}} a, \tag{6}$$

where ∇p is the pressure gradient; q is the flow rate and a is the aperture of the flow path.

3.2.4 Numerical scheme for quasi-steady state fluid flow

Details of the solution scheme is shown in Figure 45. The hydro-mechanical coupled scheme is one way in the matrix, i.e., the fluid pressure will cause the displacements of the particles since the deformation of the pore space is relatively small. However, near the wellbore, borehole expansion could lead to large fluctuation in the wellbore pressure, which directly impacts the stress field near the wellbore, and consequently the fracturing process. Therefore, two-way coupling scheme is used to update fluid pressure inside the wellbore. The scheme consists of two main calculation steps, fluid time step for pore pressure update and mechanical time step for pore structure update. During the mechanical calculation, at every five mechanical steps, volume of wellbore expansion is checked, and the wellbore pressure is adjusted to account for the pressure response from volume change,

$$\Delta p_w = K_f \frac{Q\Delta t_f - \Delta V_w'}{V_w}, \tag{7}$$

where V_w is the volume of the pore space that represents the wellbore and $\Delta V_w'$ is the volume increment due to wellbore expansion.

3.2.5 Time step selection

While the time step for the mechanical calculation is chosen automatically in PFC2D®, the time step for the fluid flow in matrix is user defined. The basic criterion we followed is that the pressure perturbation in pore spaces must be much smaller than the original pressure. An order of magnitude estimation of the critical fluid time step can be obtained from [45],

$$\Delta t_f = \frac{24\eta \bar{R} A_{pore}}{N K_f a^3}, \tag{8}$$

where A_{pore} is the area of the pore space and N is the number of contacts for a particle. From Eq. (8), we can see that both fluid bulk modulus and viscosity of fluid are critical to the fluid time step. For a shear thinning fluid with power law index $n < 1$, and if the near-wellbore shear rate is high, the apparent viscosity of the fluid will be extremely low so that the required critical fluid time step is significantly small. To avoid the convergence issue, the power law index in this work is limited to $0.5 \leqslant n \leqslant 1$.

Furthermore, the time step becomes rather small if a realistic fluid bulk modulus, $K_f = 2$ GPa, is chosen for the fluid calculation. However, if we assume the infiltration process during fluid injection into dry granular media is a quasi-steady state, and the governing equation for flow in porous media can be reduced to a Laplace equation,

$$\nabla^2 p = 0, \tag{9}$$

where the fluid bulk modulus is not included. Therefore, we can further reduce the fluid bulk modulus near the wellbore to accelerate the convergence to the quasi-steady state. A smaller fluid modulus $K_f = 75$ kPa is chosen in the fluid calculation for the pore space excluding the wellbore. By setting $A_{pore} \sim \bar{R}^2$, $a \sim \bar{R}/2$, $N = 3$, and $\eta = 1$ Pa·s , the required fluid time step yields $\Delta t_f \approx 8.5 \times 10^{-4}$ s. The characteristic time scale in pore the fluid bulk modulus may be further reduced and $K_f = 1$ kPa is set at each fluid time step for all pore spaces except the wellbore. The fluid time

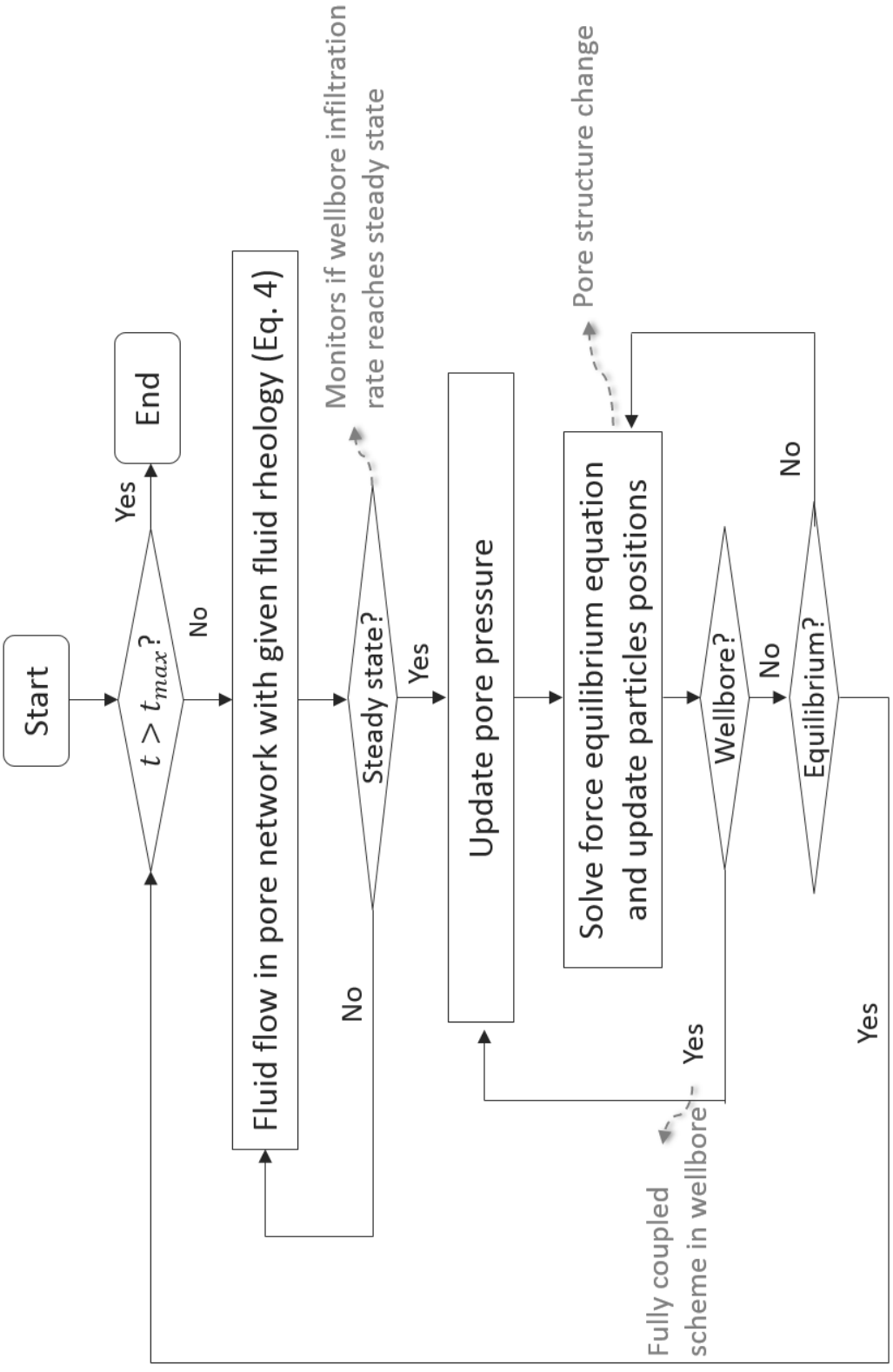

Figure 20: Quasi-steady state algorithm.

Table 5: Fluid time step for a given injection rate.

Test symbol	Injection rate Q (m^2/s)	Fluid time step (s)
a	0.02	1.0×10^{-6}
b	0.04	5.0×10^{-7}
c	0.08	2.5×10^{-7}
d	0.16	1.25×10^{-7}

step at a given injection rate in this study is listed in Table 5.

3.2.6 Improvement in the computational algorithm

The quasi-steady state fluid flow scheme is improved by the iteration of the fluid flow in pore network at each fluid time step until the summation of all flow rate in pipes connecting the wellbore reaches a constant value, while not updating the fluid drag force applied on particles. Note that iterating the entire pore network to reach the fully steady state is computationally expensive. Therefore, we take the compromise of iterating only the near-wellbore portion.

In [96], a fluid bulk modulus of $K_f = 2$ GPa (regarding as water) is used to control the wellbore pressure increment at each fluid step (Eq. (7)). If the same bulk modulus is applied, the calculation encounters large oscillation (see Figure 21). To overcome the stability issue, we relax the fluid bulk modulus during the wellbore expansion calculation. We find that the calculation is stabilized when the fluid bulk modulus is reduced $K_f^a = 5.58$ MPa. The corresponding pattern created (see Figure 22b) is comparable to the case where the realistic bulk modulus is used, and the same magnitude in the peak breakdown pressure in Figure 23 suggests that similarity in the near-wellbore stress state.

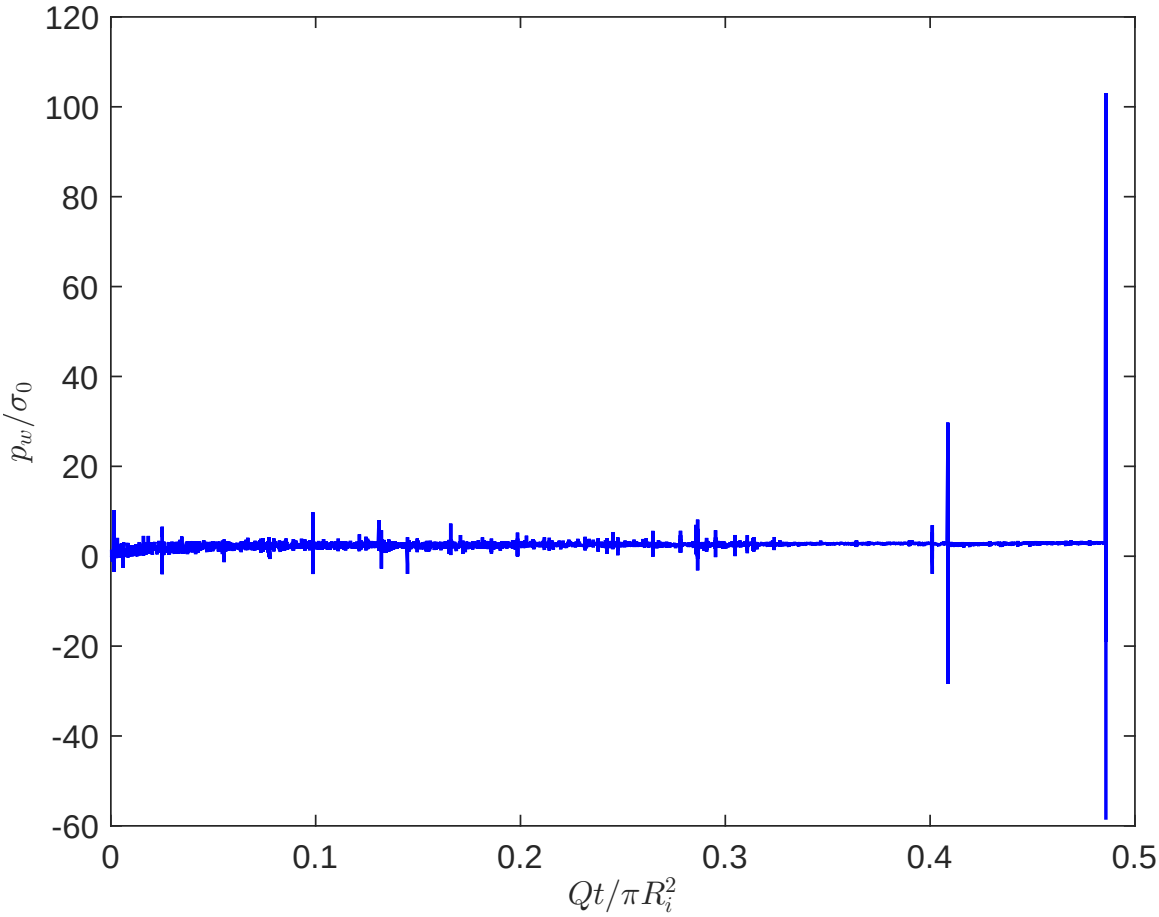

Figure 21: Wellbore pressure history for using realistic fluid bulk modulus of 2 GPa at the wellbore (scale to show large oscillation).

3.3 Model setup

A hollow circular domain is employed to model the fluid injection process. The inner and outer diameters of the domain are $D_i = 8$ mm ($D_i/\bar{R} \approx 13$) and $D_o = 160$ mm ($D_o/\bar{R} \approx 267$). The assembly consists of a total of 15,605 spherical particles (see Figure 24). A far field confining stress $\sigma_0 = 0.5$ MPa is applied through a servo-controlled wall at the outer boundary. To stimulate the injection process, a initial wellbore pressure is set to be $p_{w0} = 1.2\,\sigma_0$. All samples are generated with an identical configuration for the sake of repeatability.

The rheological parameters are chosen based on the flow curves in Figure 18. For a polyacrylamide solution with a concentration between 0.5 % and 1 %, the apparent

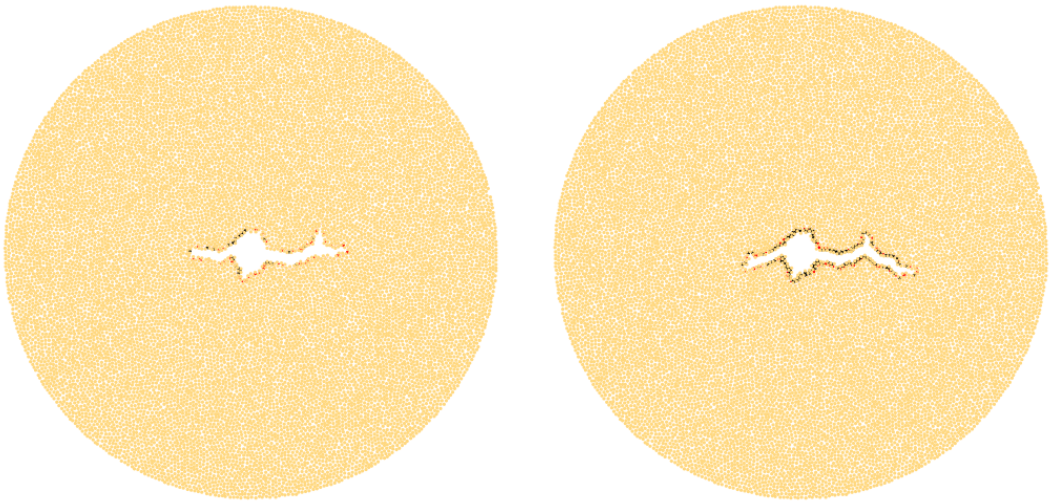

(a) (b)

Figure 22: Injection patterns for Newtonian fluid injection with $\eta = 1$ Pa·s, $Q = 0.16$ m^2/s. The wellbore bulk modulus K_f is (a) 2 GPa and (b) 5.58 MPa at a injected volume of 3×10^{-5} $m^2$and 3×10^{-4} m^2, respectively.

viscosity at shear rate $\dot{\gamma} \approx 0.01$ s^{-1} is 1000 cp. The effect of fluid rheology is first investigated by varying power law index n with the baseline Newtonian case (Test series I) and the two power law cases (Test series I2 and I3). At $\dot{\gamma} > 0.01$ s^{-1}, the Newtonian case ($n = 1$) has the highest viscosity. Due to shear thinning, the viscosity at a given shear rate is the lowest when $n = 0.8$. At $\dot{\gamma} < 0.01$ s^{-1}, the viscosity becomes the highest when $n = 0.8$. The rheology model for these three tests is depicted in Figure 26. We then investigate the effect of the consistency coefficient K by modeling fluid rheology as shown in Figure 27. Comparing with the rheology model in Test I series, the apparent viscosity at shear rate $\dot{\gamma} = 0.01$ s^{-1} is raised to 60 Pa·s, which is comparable to the case of 1 % PAAM solution ($\eta_a \simeq 60$ Pa·s at $\dot{\gamma} = 0.01$, and $n \simeq 0.36$). We study two more cases, $n = 0.8$ (Test series II1) for the effect of the consistency coefficient K and $n = 0.5$ (Test series II2) for the effect of power law index. Parameters for all test series are provided in Table 6. It should be noted that Test II2 series uses a smaller fluid time step (1/10 of other test series under the same injection rate) due to the stability issue (Eq. (8)).

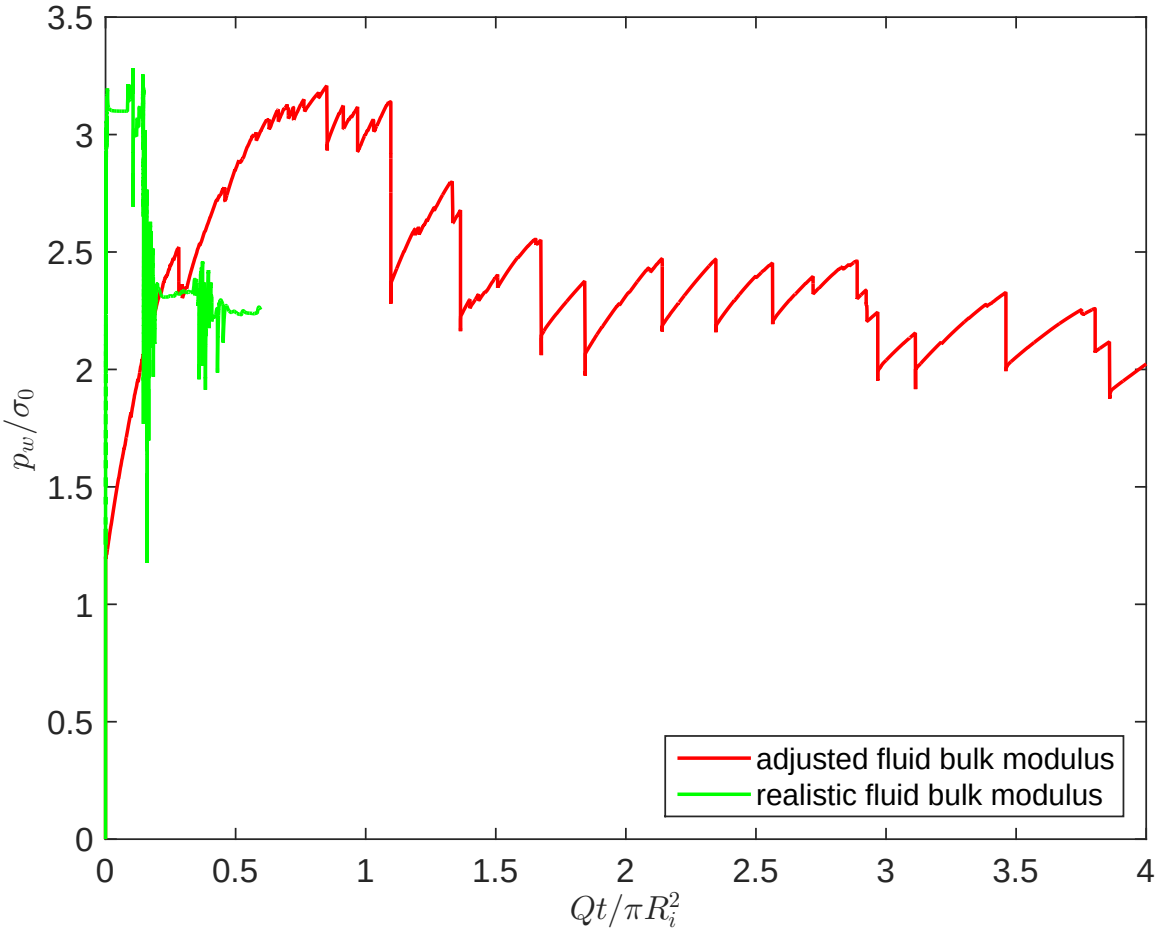

Figure 23: Wellbore pressure history for adjusted bulk modulus $K_f = 5.58$ MPa and realistic fluid bulk modulus $K_f = 2$ GPa.

Table 6: Rheology parameters for all test series. The notation a-d indicates the different injection rates as indicated in Table 5.

Test cases	K (Pa·s^n)	n	η (Pa·s) at $\dot{\gamma} = 0.01$ s^{-1}
Test I1(a-d)	1	1	1
Test I2(a-d)	0.79	0.95	1
Test I3(a-d)	0.4	0.8	1
Test II1(a-d)	23.88	0.8	60
*Test II2(a-d)	6	0.5	60

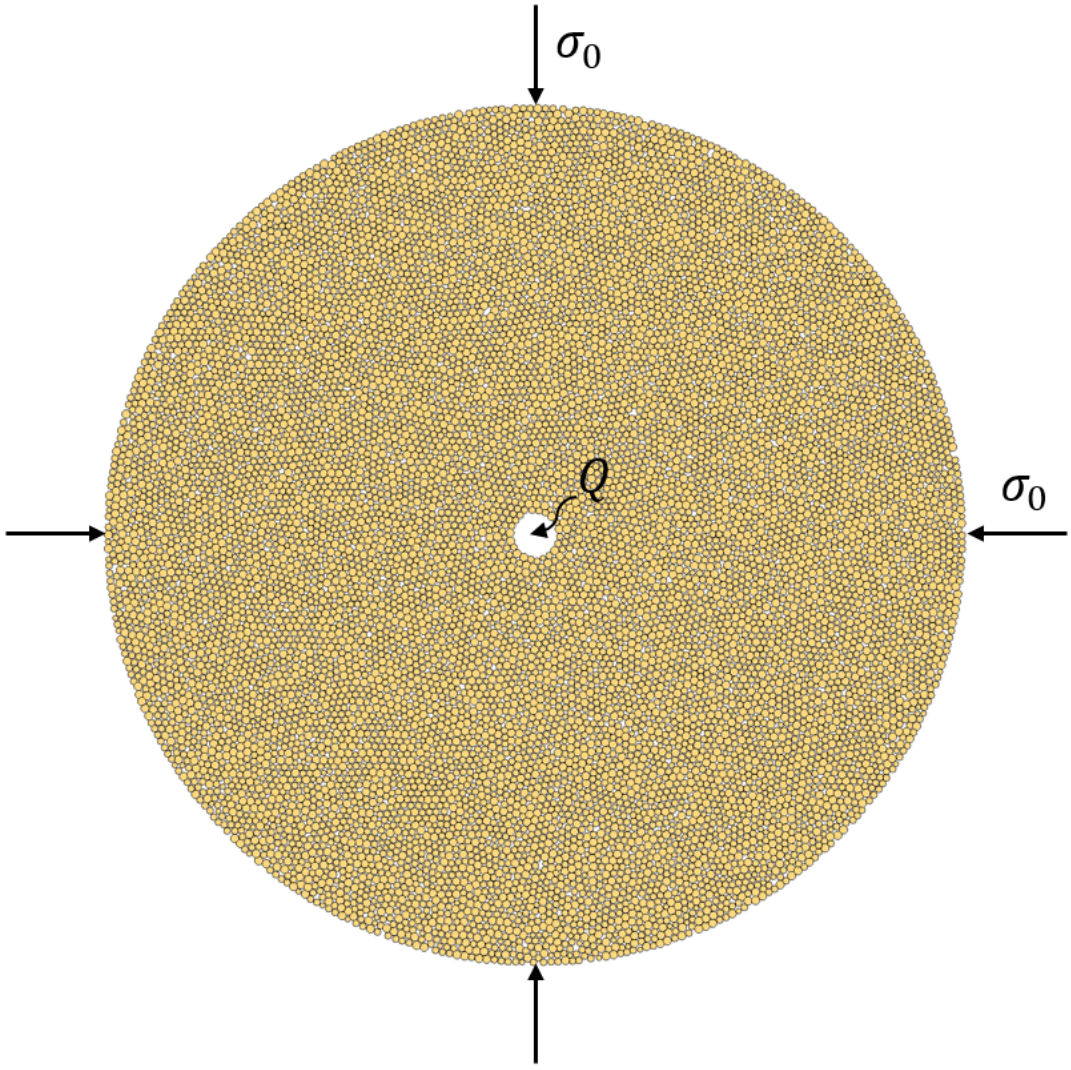

Figure 24: Model setup - cylindrical assembly.

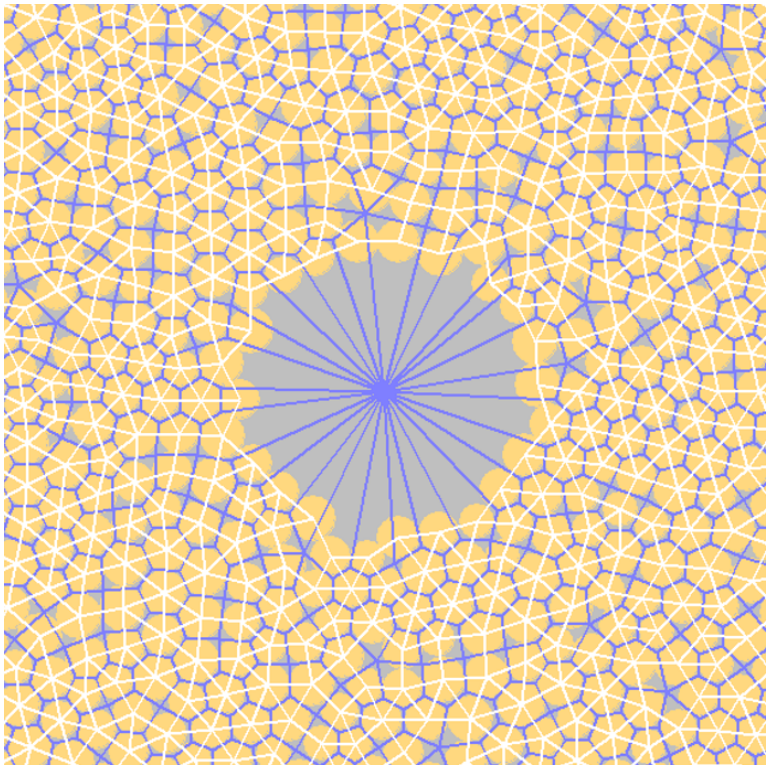

Figure 25: Pore network near the wellbore. A white line segment is the contact axis between a pair of particles. A closed chain of white lines forms a pore space. The blue lines connecting the center of adjacent pore spaces 19.

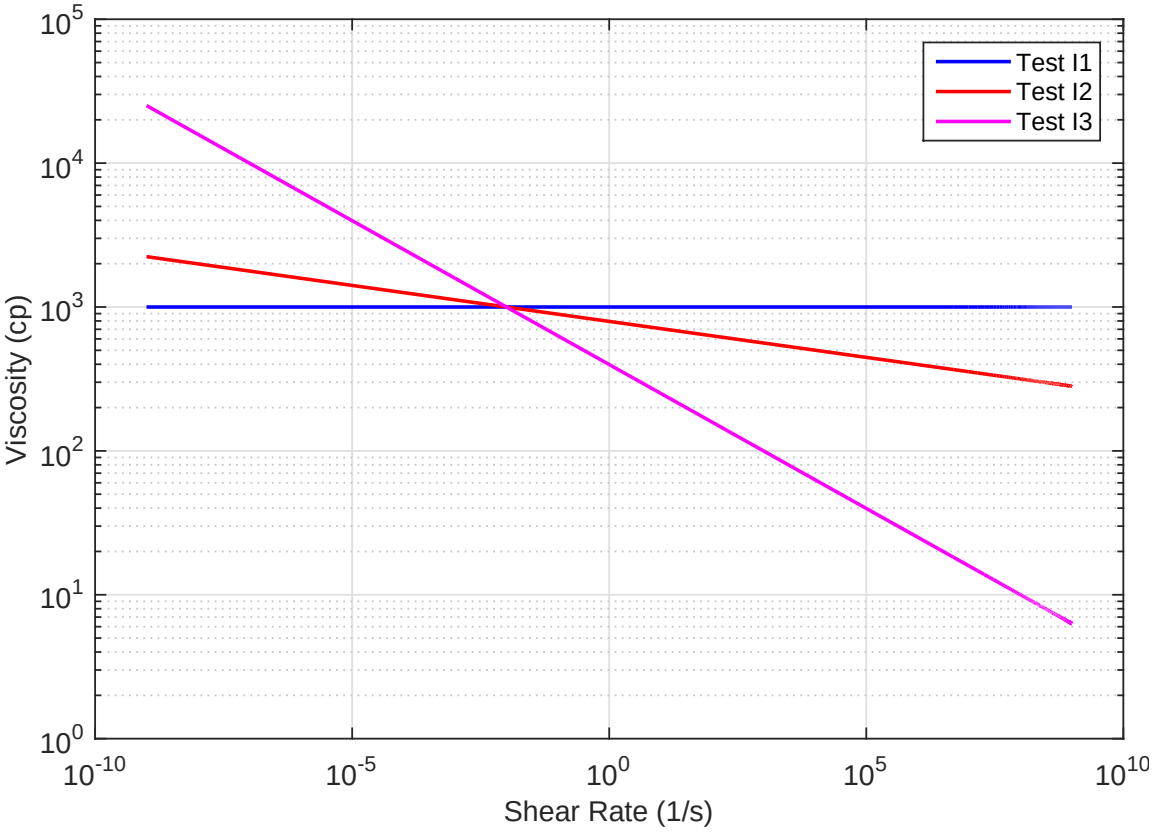

Figure 26: Rheology model for Test I series.

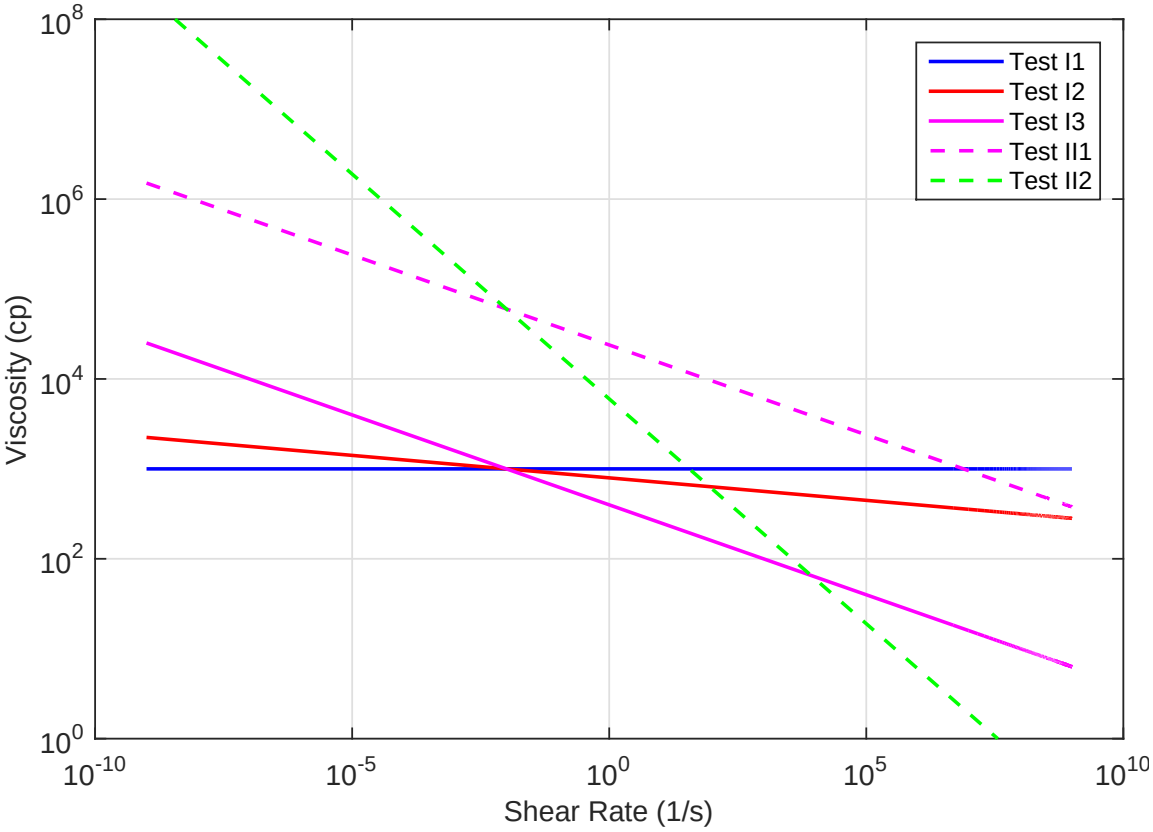

Figure 27: Rheology model for Test II series.

3.4 Fluid injection simulations

3.4.1 Displacement patterns

The displacement patterns of Test I series and Test II series at the end of simulation are shown in Figure 28 and Figure 29, respectively. The orange circles represent the particles. The dark area indicates the infiltration area. The white area connected to the wellbore indicates the fluid channels created. The numerical simulations yield results that are consistent with the experimental observations in [40, 41] that at a relatively low injection rate, e.g., $Q = 0.02$ m^2/s (Test I2(a)), the response of the granular medium is mostly infiltration governed. As the injection rate increases, the grain movements are promoted while the infiltration is limited, e.g. at $Q = 0.16$ m^2/s (Test I2(d)), the granular response is in a grain-displacement dominated regime. Meanwhile, by decreasing in power law index n, fluid infiltration could be also promoted at the same injection rate. For instance, Test I2(d) is in simple radial flow regime in contrast to Test I1(d) which is in grain-displacement dominated regime. The difference in pattern under the same injection rate demonstrates the high shear rate is governing the near the wellbore fluid behavior, and it is also consistent with the experimental observation in Figure 17, where for the PAAM solution, larger leakoff area is observed comparing to Newtonian fluid case at the same injection rate.

Furthermore, compared with Test I3 series, the granular responses in Test II1 series resemble those in injection tests of a more viscous fluid. We may therefore conclude that the effect of increase in the consistency coefficient K is similar to the effect of increase in the Newtonian viscosity. On the other hand, with a power law index with $n = 0.5$, near the wellbore fluid flow pattern is radial. That is because the power law index of Test II2 series is smaller than that of Test II1 series. Again, this shows that the high shear rate governs the near-wellbore behavior.

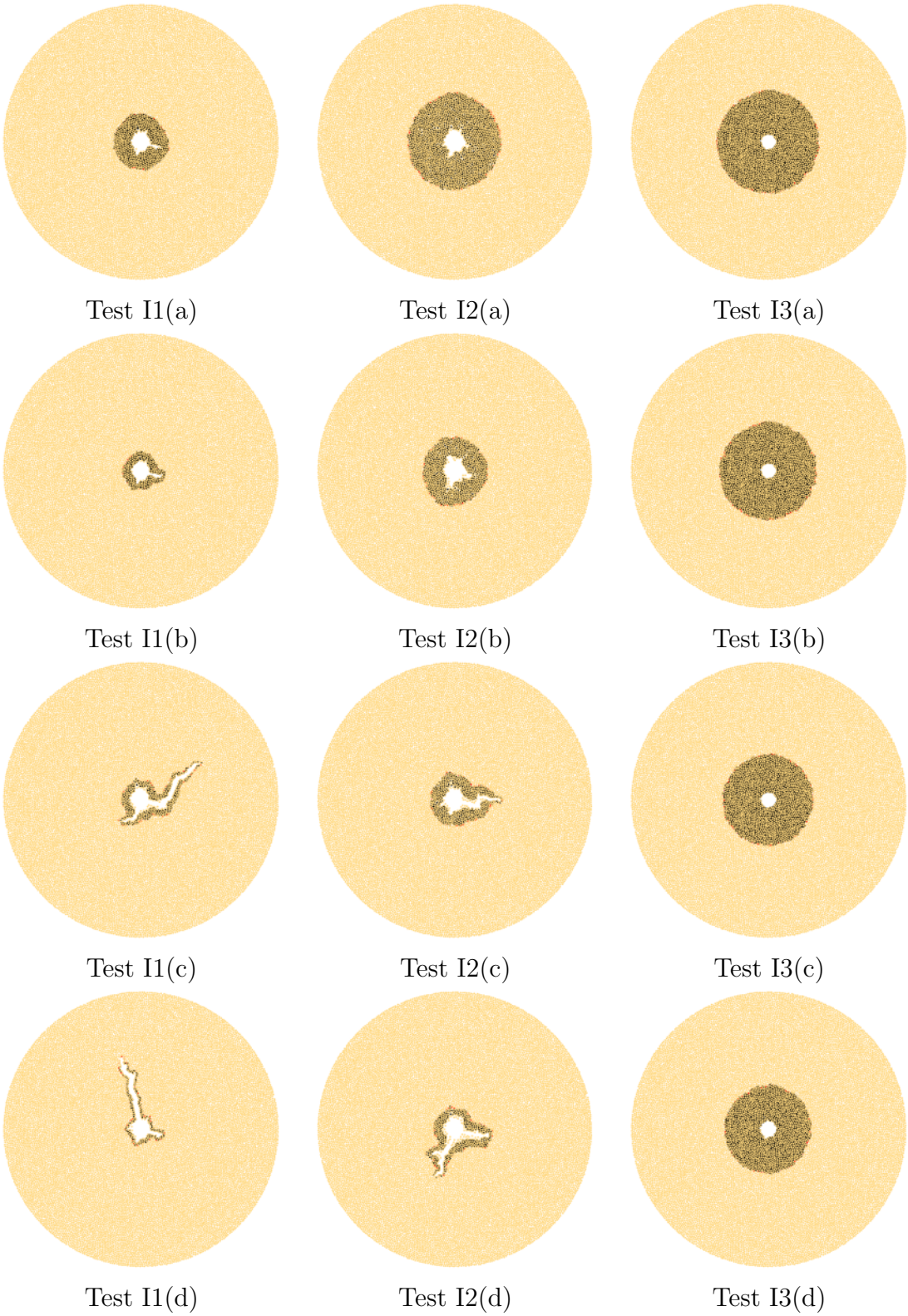

Figure 28: Test I displacement patterns at the end of the simulations at injection rates (a) $Q = 0.02$ m^2/s, (b) $Q = 0.04$ m^2/s, (c) $Q = 0.08$ m^2/s, and (d) $Q = 0.16$ m^2/s

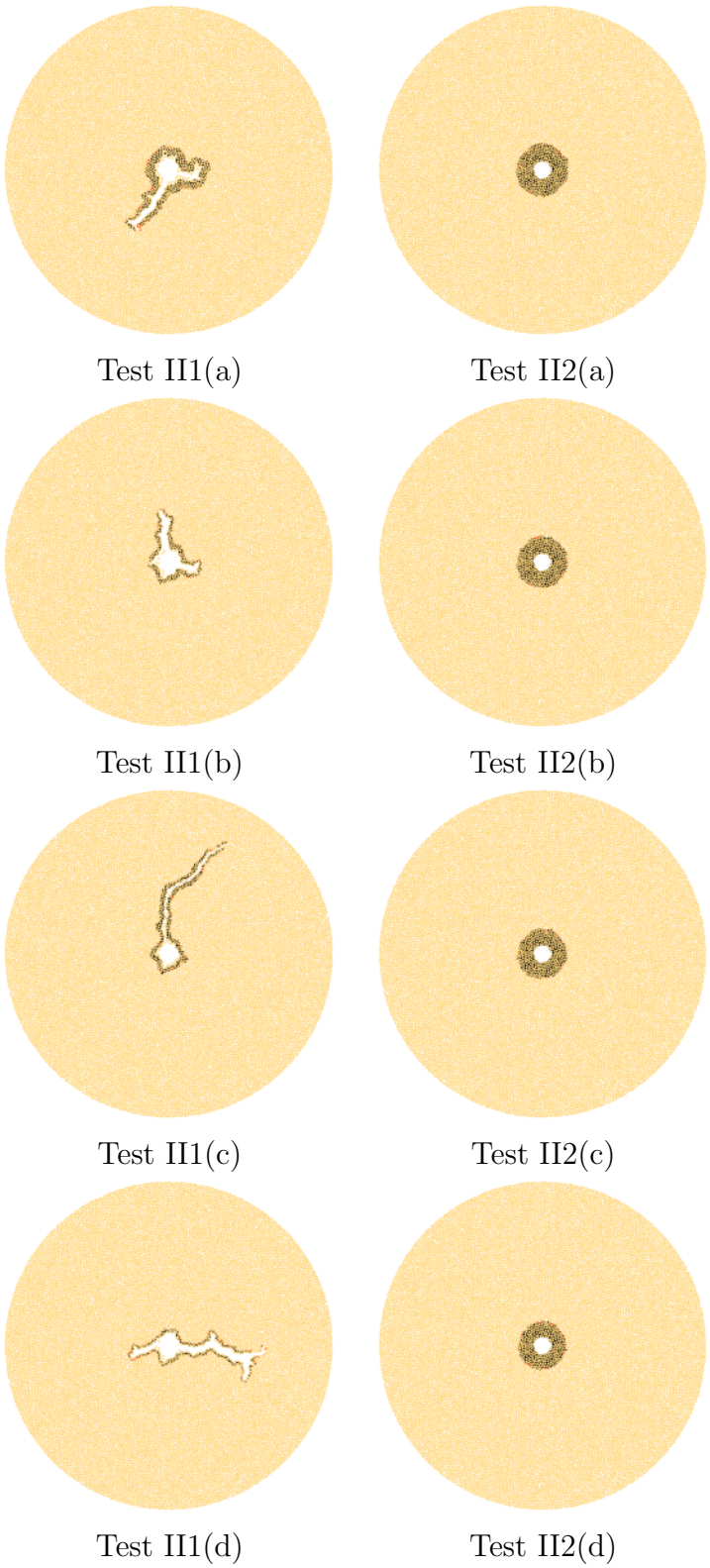

Figure 29: Displacement patterns of Test II series at the end of the simulations.

3.4.2 Effect of injection rate

As aforementioned, the injection rate causes the granular responses transition from infiltration governed to displacement governed. In the numerical simulations, the ratio of the leakoff volume V_l to the total injected volume $V_i = Qt$, where t is the injection time is monitored. As can be seen in Figure 30, after an initial period, the ratio between the leakoff and the injected volume more or less reaches a plateau. For Test II1(a), $V_l/V_i \approx 0.8$ indicating that nearly 80 % of the injected fluid is stored in the pore spaces. The ratio V_i/V_l remains nearly constant at $V_i/\pi R_i^2 > 2$. As the flow rate increases, the proportion of the injected fluid going into the pore spaces decreases. For Test II1(d), $V_l/V_i \approx 0.3$ indicating infiltration is restrained, and the fluid entering in the wellbore will remain inside and displaces the near-wellbore grains. At a later stage, e.g., after $V_i/\pi R_i^2 > 2$ at $Q = 0.08$ m^2/s, the area ratio V_i/V_l declines, which could be interpreted as the growth of the fracture or the fluid channel accelerates.

3.4.3 Wellbore pressure history

The wellbore pressure histories under injection rate $Q = 0.02$ m$^2/s$ and $Q = 0.08$ m$^2/s$ as shown in Figure 32 and Figure 33. The pressure drop indicates creation of openings. The transition from the infiltration governed to infiltration-limited behaviors is also reflected in the wellbore pressure history. For simple radial flow, Test II2a and Test I3a, the pressure increases continuously. Meanwhile the wellbore pressure history shows a distinct peak, or the breakdown pressure at larger injection rates from Figure 31. The ratio between peak breakdown pressure and the confining stress is $p_w/\sigma_0 \approx 3$, which is also observed from the simulations with fluid viscosity $\eta = 1$ Pa·s at larger injection rates [96]. The fact that the results are similar in these cases may be explained by the fact that when the injection rates are relatively high, fluid permeation near the wellbore is limited.

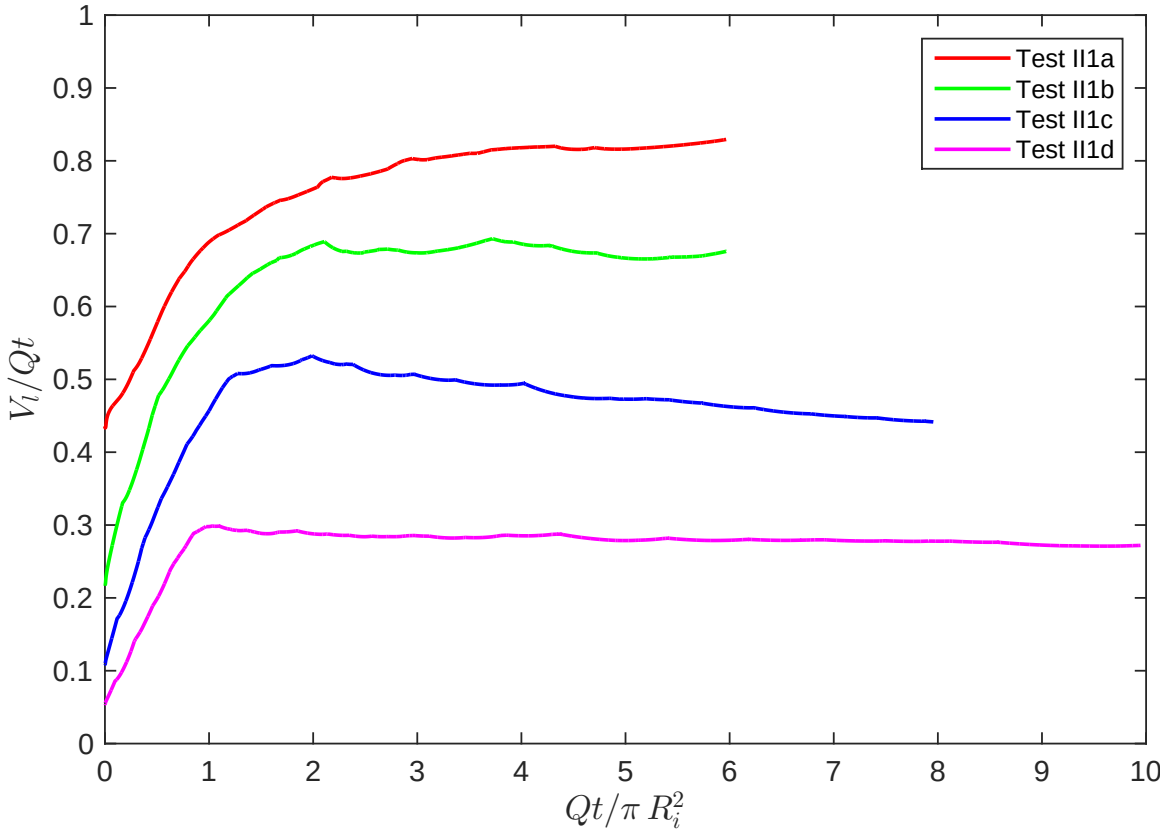

Figure 30: Normalized leakoff volume V_l/Qt versus the normalized injected volume $Qt/\pi R_i^2$ for Test II1 series.

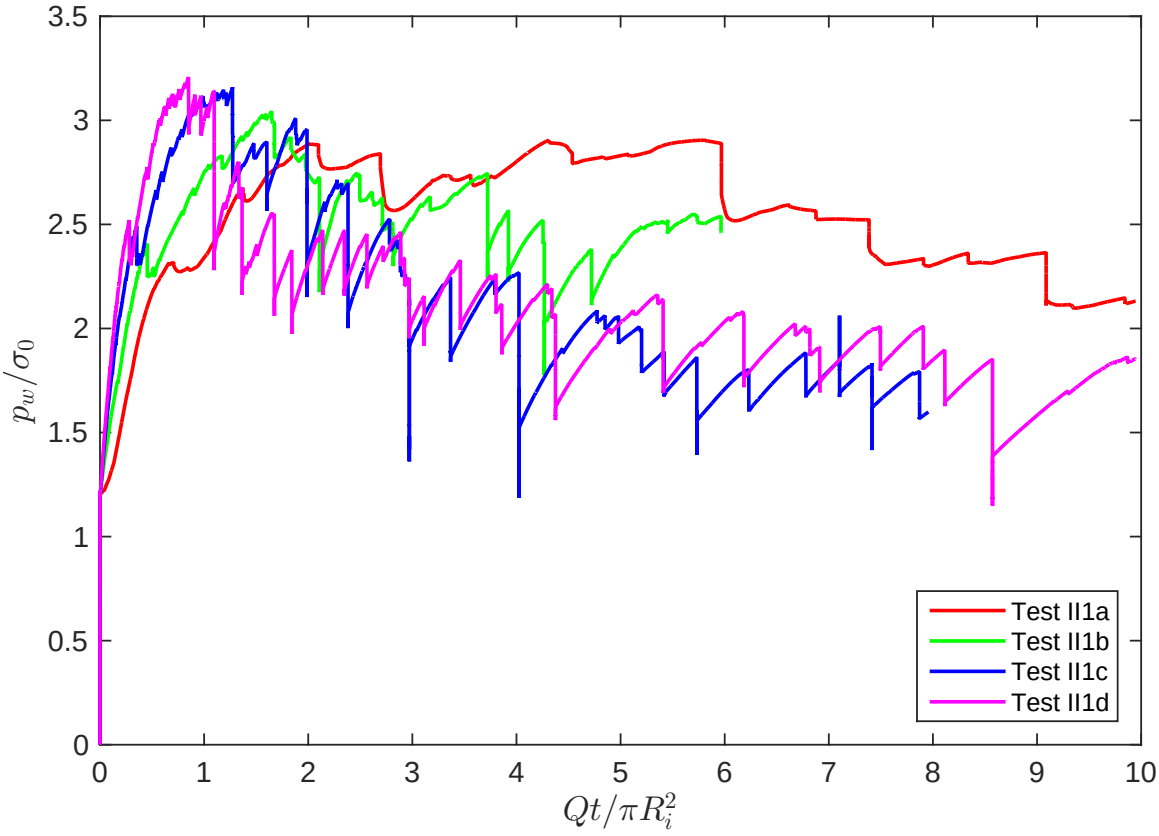

Figure 31: Wellbore pressure history for Test II1 series.

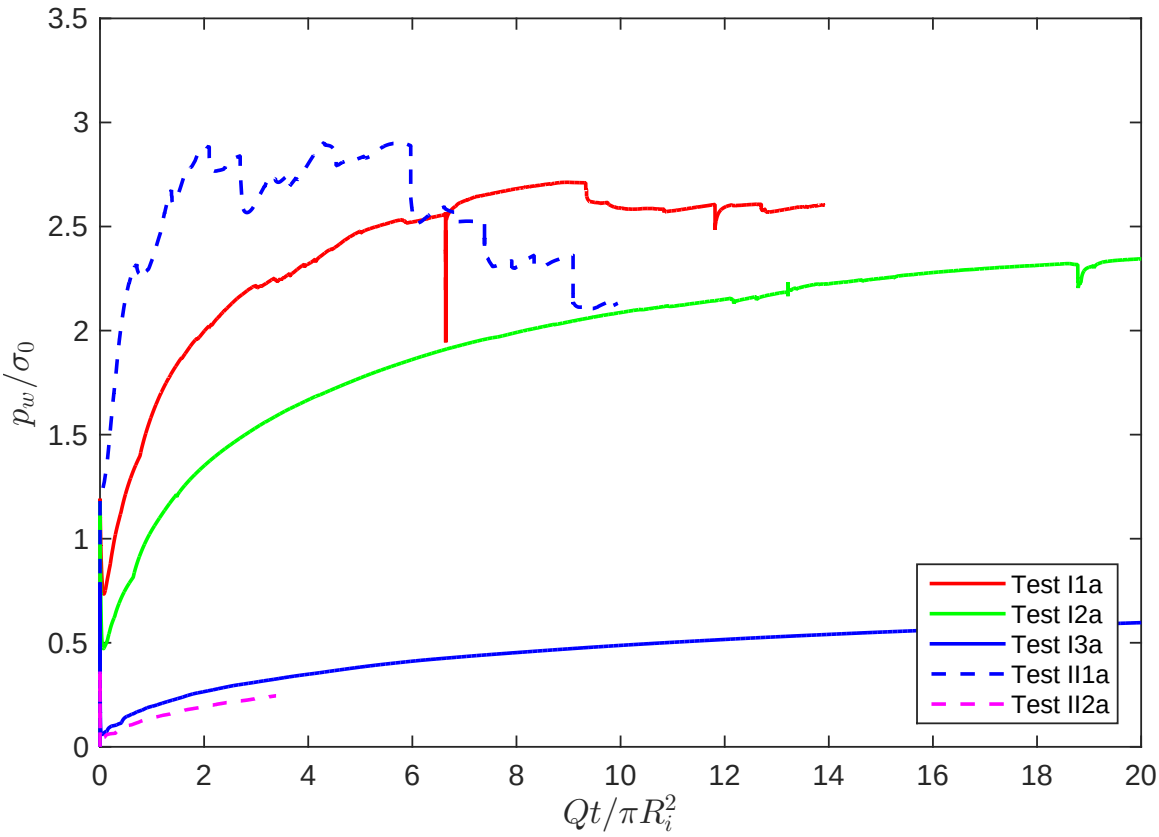

Figure 32: Wellbore pressure history under injection rate $Q = 0.02$ m^2/s.

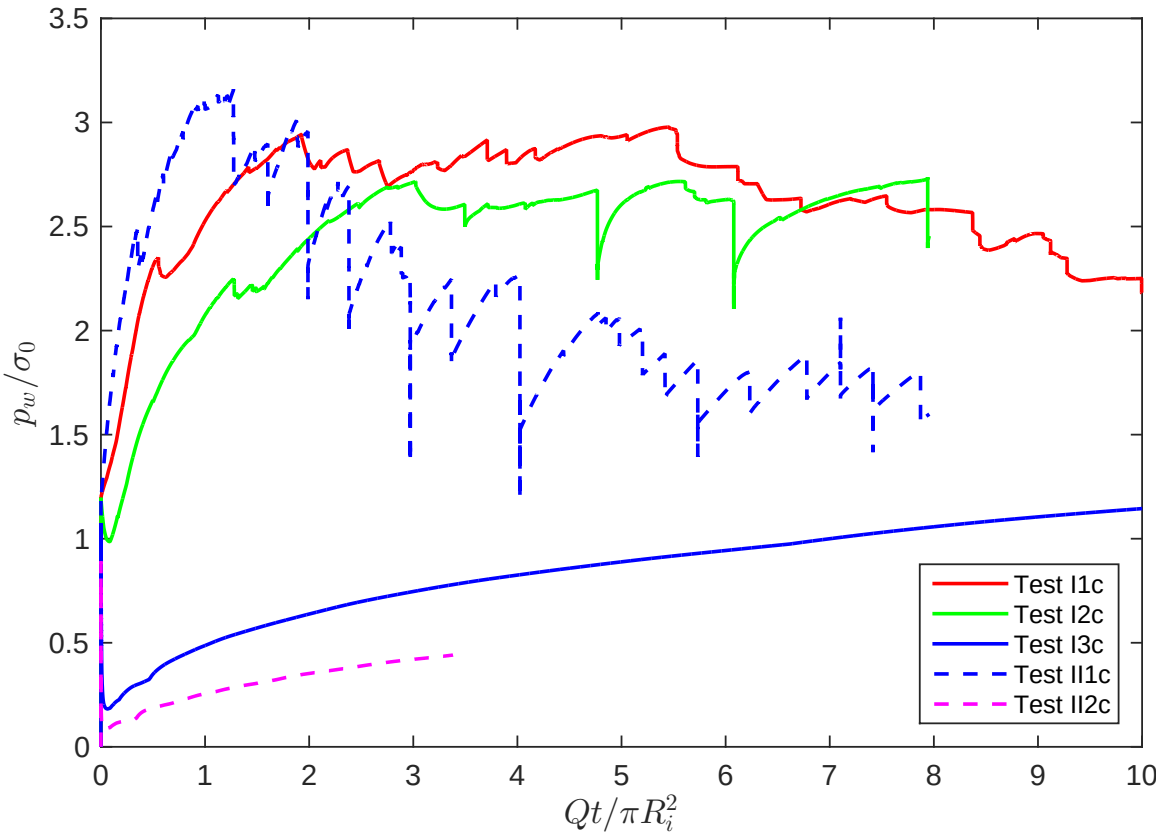

Figure 33: Wellbore pressure history under injection rate $Q = 0.08$ m^2/s.

On the other hand, at lower injection rate $Q < 0.08$ m^2/s, we find the peak breakdown pressure is affected by near-wellbore fluid behavior. At the same injection rate $Q = 0.02$ m^2/s, shear thinning fluid ($n = 0.95$) has more infiltration, so that the near-wellbore effective stress is less than the Newtonian case due to pore pressure (see Figure 34). The reduction in the effective stress means that a smaller pressure is needed to open the local defects and to initiate fractures. As a result, the peak breakdown pressure is smaller in Test I2a than that in Test I1a (see Figure 32). The ratio p_w/σ_0 at large injection rates (or when the viscosity is high) is nevertheless strongly influenced by the confining stress. For the Newtonian cases, given an intergranular friction coefficient $\mu = 0.577$, $p_w/\sigma_0 \approx 4.3$ at $\sigma_0 = 0.1$ MPa, and $p_w/\sigma_0 \approx 2.4$ at $\sigma_0 = 1$ MPa.

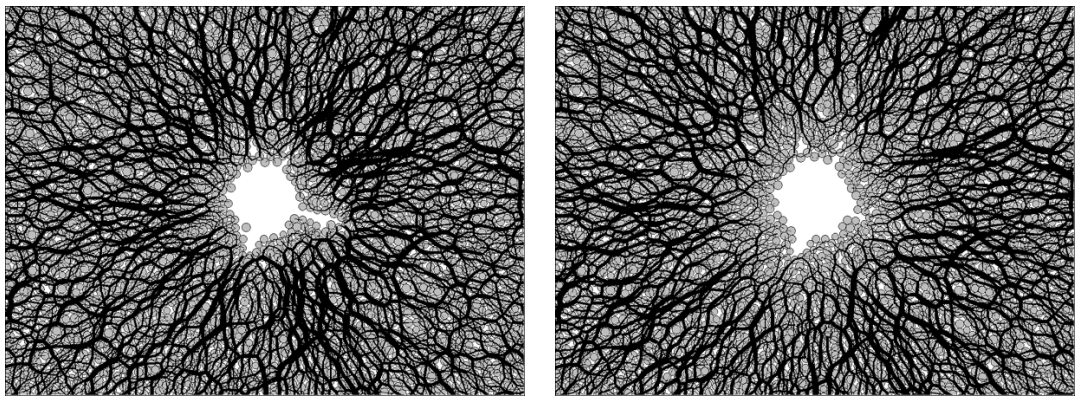

(a) (b)

Figure 34: Near the wellbore contact force chains. The darker in color indicates the larger the contact force is. (a) Test I1a at $V_i = 7 \times 10^{-4}$ m^2, and (b) Test I2a at $V_i = 2 \times 10^{-3}$ m^2.

3.4.4 Energy partition

As discussed in Zhang et al.[96], the viscous energy competes with the work done by fluid drag force to form different displacement patterns. We have also observed the same energy competition as can be seen through Test II1a to Test II1d in Figure 35, where E_b is body force work done by the fluid drag force; E_f is the energy loss due to friction; E_k is the kinetic energy in the system; $E_c$is the strain energy; E_w is the

energy input at the outer boundary; and E_v is the viscous dissipation along the flow paths. For Test series II1, at $Q = 0.02$ m^2/s, the main energy dissipation mechanism is through flow in the porous media, where as at $Q = 0.16$ m^2/s, the work done by the fluid drag force becomes the primary energy dissipation mechanism. For Test II1(c) and Test II1(d), at $Qt/\pi R_i^2 > 3$, we find that the body force work done by the fluid drag force fluctuates at high injection rate and high apparent viscosity. Such fluctuation may have been a result of the fact that, in this numerical analysis, the pressure in the fluid channel is set to be the same as that in the wellbore when the fluid channel grows unstably. In the case of Test I3(d) and Test II2(d), the system energy dissipates mainly in the form of viscous dissipation, which is consistent with grain displacement pattern as the simple radial flow regime in Figure 28 and 29.

3.5 Apparent viscosity to characterize the injection process

Comparing Test II1 series with Test I1 series, we find variations of the leakoff ratio V_l/V_i during the injection are close to each other (see Figure 37 and pattern similarity in Figure 36). If we define a nominal shear rate based on the pore throat size l and set $l \simeq \sqrt{k}$, which yields,

$$\dot{\gamma}_a = \frac{Q}{\pi D_i \sqrt{k}}. \tag{10}$$

Therefore, given the power law model, Test II1(a) has an apparent viscosity $\eta_a = 3.097$ Pa·s, and $\eta_a = 2.696$ Pa·s for Test II1(b). Accounting for the effect of the injection rate, we can characterize the fluid behavior through $Q\eta_a$. Recalling the viscosity of the Newtonian fluid in this simulation is 1 Pa·s, $Q\eta_a$ for Test I1(c) and Test I1(d) can be calculated as 0.08 Pa $\cdot$ m^2 and 0.16 Pa $\cdot$ m^2 at injection rates $Q = 0.08$ Pa $\cdot$ m^2 and $Q = 0.16$ Pa $\cdot$ m^2 respectively. For non-Newtonian fluid the $Q\eta_a$ for Test II1(a) and Test II1(c) gives 0.062 Pa $\cdot$ m^2 and 0.108 Pa $\cdot$ m^2. We find $Q\eta_a$ of Test II1(a) is similar to that of Test I1(c). Test II1(a) which has slightly smaller $Q\eta_a$ has slightly larger

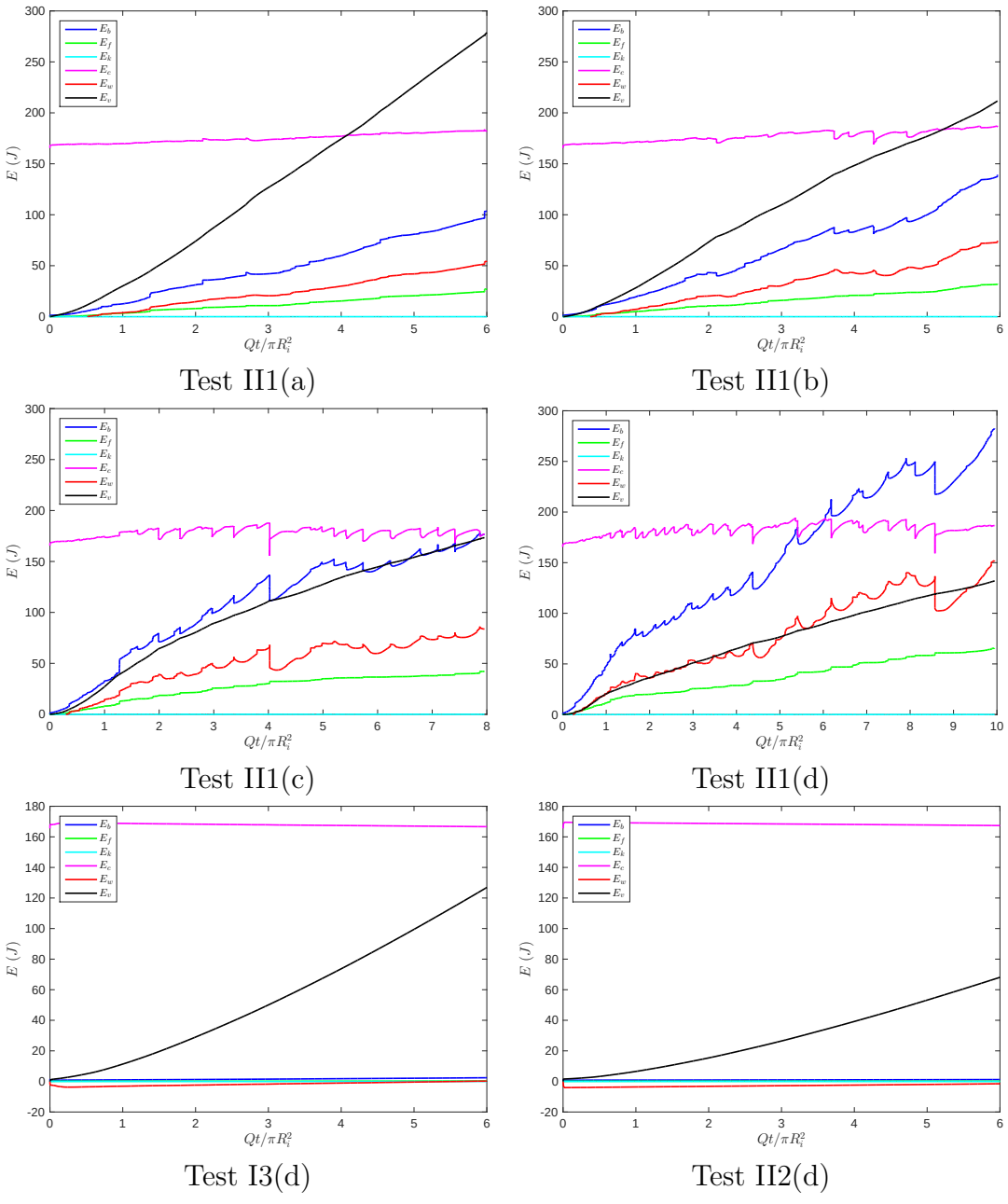

Figure 35: Energy partition.

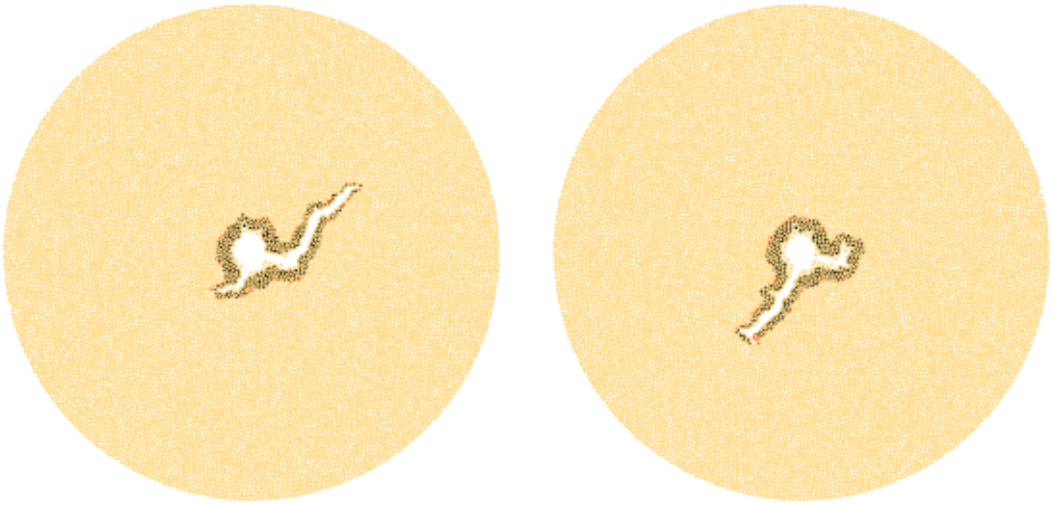

Test I1c

Test II1a

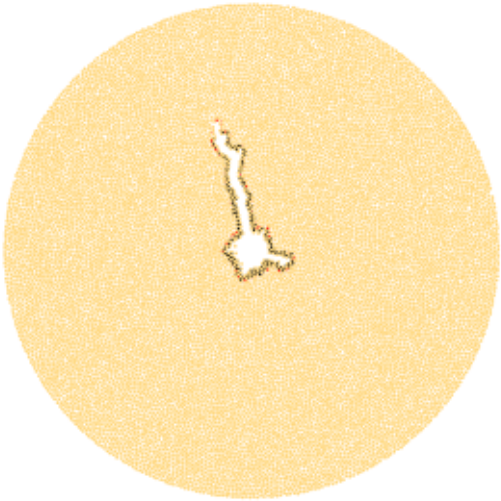

Test I1d

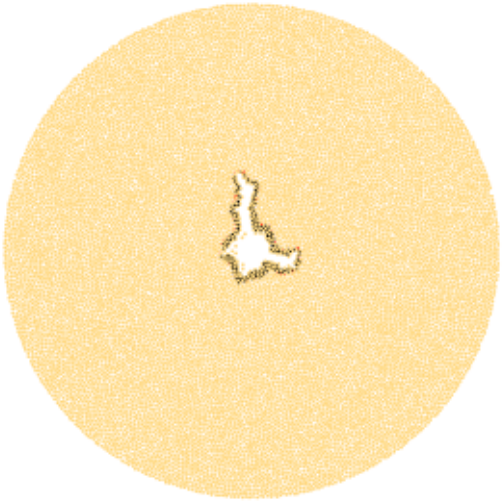

Test II1b

Figure 36: Displacement patterns under similar leakoff ratio.

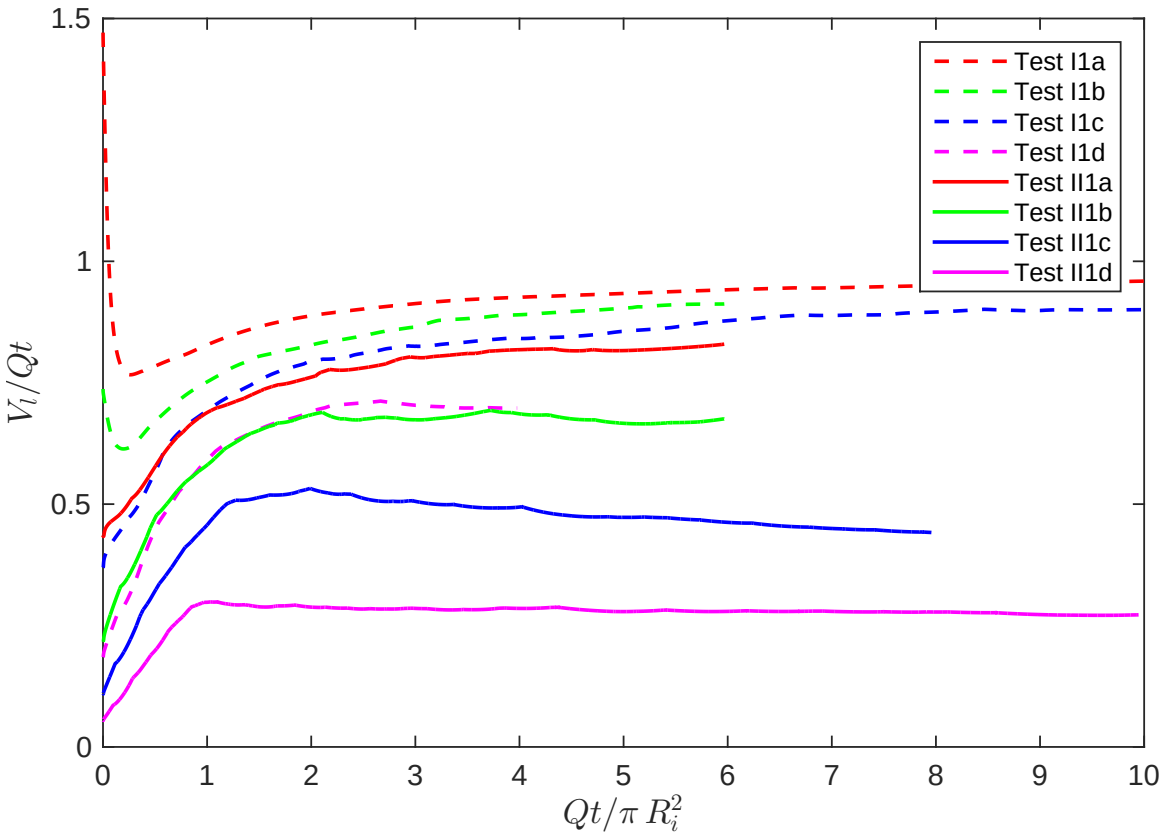

Figure 37: Comparison between the cases with a Newtonian fluid and a non-Newtonian fluid on normalized leakoff volume V_l versus the injected volume V_i. The dips at initial stage are caused by the non-zero initial pressure setup in the wellbore as $p_w = 1.2\,\sigma_0$.

Table 7: Apparent viscosity η_a (Pa·s) near the wellbore. (a) $Q = 0.02$ m^2/s, (b) $Q = 0.04$ m^2/s, (c) $Q = 0.08$ m^2/s, and (d) $Q = 0.16$ m^2/s.

Test cases	(a)	(b)	(c)	(d)
Test I1	1	1	1	1
Test I2	0.477	0.460	0.445	0.430
Test I3	0.052	0.045	0.039	0.034
Test II1	3.097	2.696	2.347	2.043
Test II2	0.036	0.026	0.018	0.013

leakoff ratio V_l/V_i at early stage (see Figure 37), but as the injection continues, the ratio of non-Newtonian case falls below indicating fracture growth is faster than that in Newtonian fluid. $Q\eta_a$ of Test II1b is also similar to that of Test I1d, consequently, resemblance in pattern can be observed (see Figure 36). $Q\eta_a$ for all tests is provided in Table 8. From the table, the similarity in grain displacement can be also found in Test I1(a) and Test I2(b) as well as Test I2(d) and Test II1(a). $Q\eta_a$ can also describe the simple radial flow observed in Test I3 and Test II2 series, where the values of $Q\eta_a$ in these tests are one order of magnitude less than that in Newtonian fluid case. As $Q\eta_a$ increases, the grain displacement is promoted in a sense of increasing in fluid viscosity and injection rate in Newtonian fluid injection tests. As an another example, Test I1(d) has larger $Q\eta_a$ comparing to that of Test II1(d). Although the infiltration is limited for both cases, the granular fingers created in the former case is wider than the latter one indicating grain displacement is more dominant in the former case. In addition, due to limited permeation, the leakoff size is in the scale of grain size, so infiltration amount cannot be accurately differentiated. Therefore, it is possible to use the apparent viscosity, combined with the injection rate, to predict the grain displacement patterns during non-Newtonian fluid invasion into dry granular media.

Furthermore, the characterization of shear thinning fluid with $Q\eta_a$ is also reflected in the wellbore pressure history. Looking into the case of TestI1c (Figure 38) and Test

Table 8: $Q\eta_a$ ($\text{Pa} \cdot \text{m}^2$) near the wellbore. (a) $Q = 0.02$ m^2/s, (b) $Q = 0.04$ m^2/s, (c) $Q = 0.08$ m^2/s, and (d) $Q = 0.16$ m^2/s.

Test cases	(a)	(b)	(c)	(d)
Test I1	0.020	0.040	0.080	0.160
Test I2	0.010	0.018	0.036	0.069
Test I3	0.001	0.002	0.003	0.005
Test II1	0.062	0.108	0.188	0.327
Test II2	0.001	0.001	0.001	0.002

II1a (Figure 39), the similar pattern has almost identical pressure history (see Figure 31 and Figure 33).

3.6 Conclusions

The process of fluid injection into dense granular media is modeled using the DEM code PFC2D® coupled with a pore network model with the focus on the effect of non-Newtonian rheology. The numerical analysis shows that for a shear thinning fluid, the high shear rheology is critical to the early time near-wellbore behaviors. The transition in the fluid flow and granular response is reflected not only in the partition of the injected fluid volume between the pore spaces and the newly created openings, but also in the wellbore pressure history and the energy partition in the system. As the injection rate becomes large, the breakdown pressure becomes insensitive to the fluid rheology. An apparent viscosity of non-Newtonian shear thinning fluid is defined to characterize the fluid-grain displacement patterns during fluid injection into a densely packed granular medium. The DEM coupled analysis provides valuable insights into the effect of shear thinning rheology on the injection process. Nevertheless, it should be recognized that the numerical simulations in this work capture only the early time response near the wellbore. The role of rheology at late time needs to be further explored.

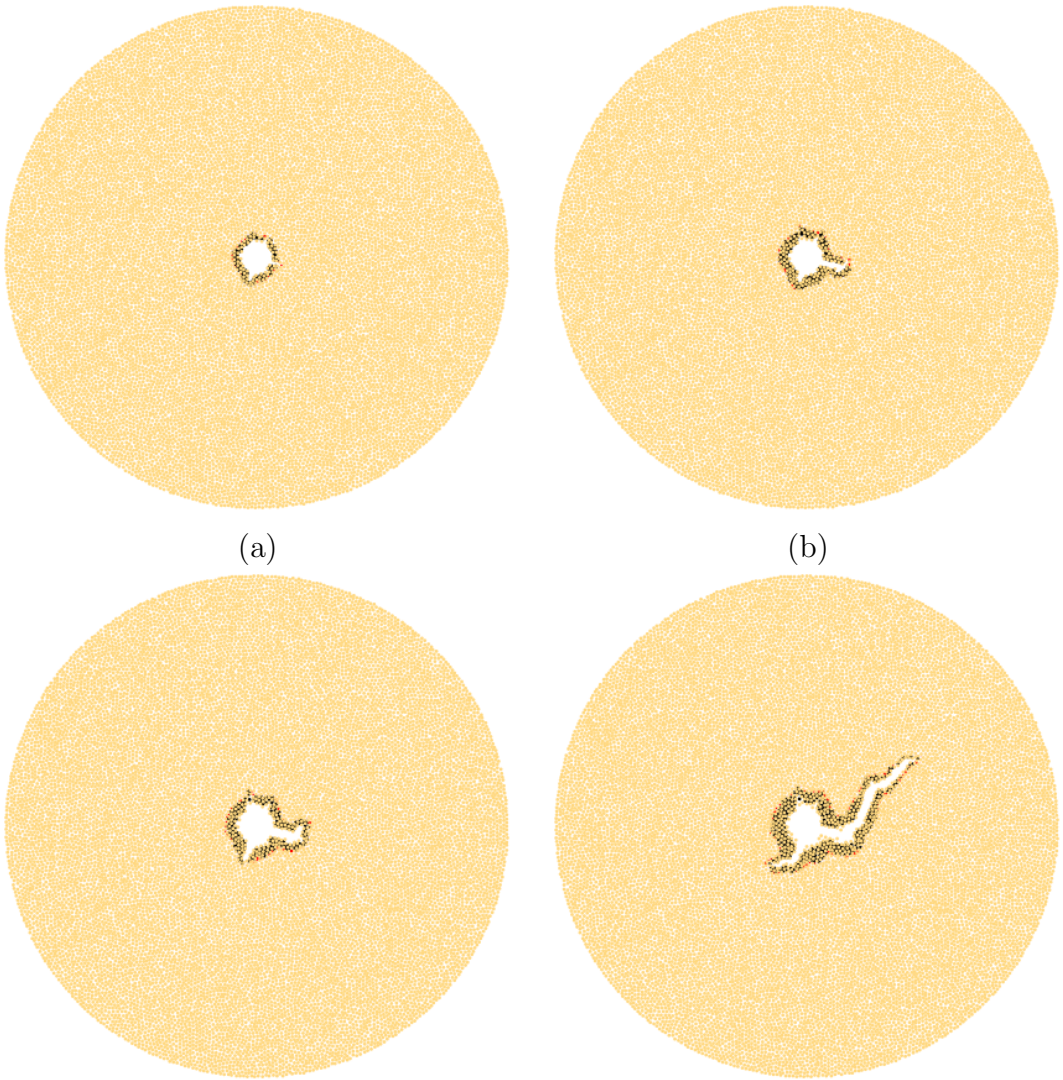

Figure 38: Pattern formation under Newtonian fluid injection - Test I1c at injected volume V_i: (a) 1×10^{-4} m^2, (b) 2×10^{-4} m^2, (c) 3×10^{-4} m^2, and (d) 6×10^{-4} m^2.

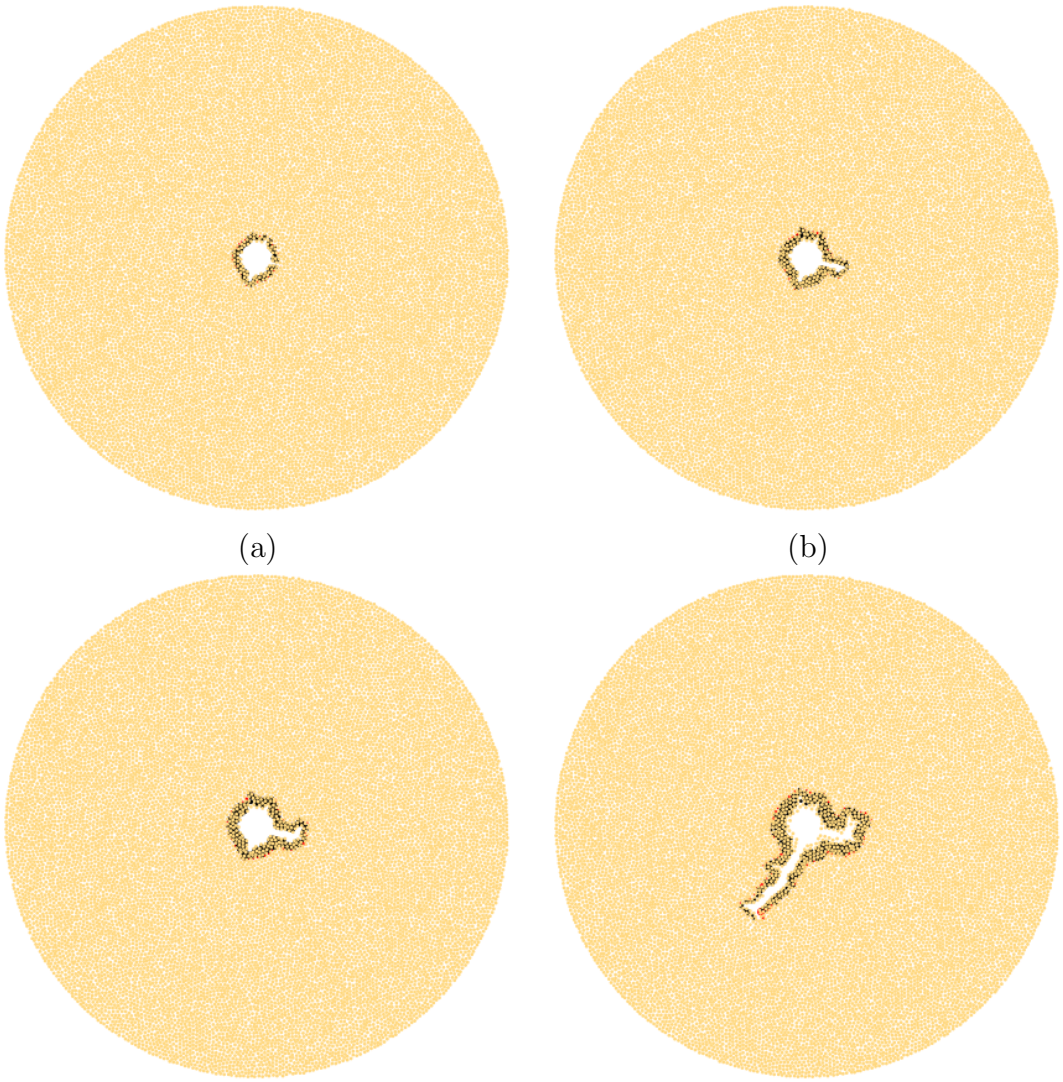

Figure 39: Pattern formation under non-Newtonian fluid injection - Test II1a at injected volume V_i: (a) 1×10^{-4} m^2, (b) 2×10^{-4} m^2, (c) 3×10^{-4} m^2, and (d) 6.9×10^{-4} m^2.

CHAPTER IV

PHASE FIELD METHOD FOR PRESSURIZED FRACTURE PROPAGATION IN POROUS MEDIA

4.1 Introduction

Phase field method is to regard the material's different states or phases (sharp discontinuity) as continuous phase field (order parameter) that it can evolve in a continuum domain [94]. For fractures in solids, the sharp interface can be regularized by an phase field variable ϕ, which introduces a diffused crack zone between the broken and the unbroken material. A benefit of the phase field method, which has been widely used to model the solidification process [82], is that the creation of a fracture could be modeled through explicit consideration of phase change so that the numerical scheme is free from tracking the sharp interface. Fixed grid mesh setup can be used, thereby reducing the computational cost [73].

The application of the phase field method in solid mechanics has drawn much attention recently. Initially, the idea is to model fracture propagation in a similar way as the phase transition in the solidification process [24, 35, 39, 51]. In late 1990s, phase field method of brittle fracture was first developed in [27, 6], and a thermodynamically consistent frame work is later constructed by Miehe et al.[70]. Evolution of the phase field variable can be modeled as either quasi-static (rate-independent) or viscous (rate-dependent) [70]. Quasi-static phase evolution has been recently adopted to simulate the hydraulic fracturing process [10, 73, 74, 56, 57, 95]. However, it was shown [70] that viscous regularization provides a more stable scheme, compared to the quasi-static process. Furthermore, various forms of the constitutive law have been used with the assumption that fractures can be only created in tension. Compared

Table 9: Model Comparison for different phase field approaches to fluid filled crack propagation.

	Constitutive law	Phase Field Evolution
Bourdin et al.[10]	Isotropic	Quasi-static
Mikelić et. al[73]	Isotropic	Quasi-static
Mikelić et. al[74]	Anisotropic [4]	Quasi-static
Lee et al.[57, 56]	Anisotropic [4]	Quasi-static
Current work	Hybrid [2]	Viscous

to non-linear forms in [4, 70], the linear form of the hybrid scheme [2] significantly reduces computational costs. In this work, a hybrid phase field method is developed by adopting viscous phase evolution and the hybrid scheme for constitutive law to investigate the pressurized fracture propagation problem. The numerical algorithm is implemented using COMSOL.Multiphysics® as a numerical platform.

The chapter is structured as follows. Section 4.2 introduces phase field model similar to that by Miehe et al.[70]. Section 4.3 illustrates the mathematical model for the problem of interest (see Eq. (43)). First, it revisits the derivation of energy partition in pressurized fracture propagation problem by Mikelić [73, 75], then further extends the work with adding features as viscous regularization, maximum history field [71], and hybrid model [2] to improve the stability, seize the irreversible condition, and improve the computational efficiency. Section 4.4 provides the overall algorithm of the simulation. Section 4.5 provides the calibration of the model which compares the results from phase field model with the classic Griffith's theory, and briefly discusses about the effect of mobility. Also, the section shows the capability of the phase field method to produce the crack formation from an intact sample without assigning initial phase values on nodes to indicate crack phase. After that, the displacement of a stationary crack filled with pressurized fluid is compared with classic Sneddon's solution. In Section 4.6, a series of injection tests into the brittle media are conducted to show the capability of the phase field method to capture the interaction between cracks and fracture propagation patterns, including initiation, propagation, merging,

and tip spitting. Also, crack growth from a wellbore is modeled under various stress conditions.

4.2 Governing equations for phase field method

4.2.1 Crack in one dimensional domain

In a one dimensional domain, the crack acts as a single point of the discontinuity in the domain $\Omega = \Gamma \cup L$. Γ is the crack surface, and L is the domain along x. We here introduce a phase field variable ϕ, $\phi = 0$ for a fracture phase and $\phi = 1$ for an intact solid phase. The sharp discontinuity can be approximated as a smooth transition in phase field [70],

$$\phi = 1 - e^{-|x|/l_c}, \tag{11}$$

where l_c is the characteristic length that determines the thickness of the diffused crack zone over domain. When $x \to 0$, $\phi \sim \frac{x}{l_c} + \mathrm{O}(x^2)$. The constructed phase transition relation in Eq. (11) is actually the solution of Euler's equation:

$$[1 - \phi(x)] + l_c^2 \phi''(x) = 0. \tag{12}$$

If we follow the variational approach, we can construct a weak form equation in terms of functional:

$$I(\phi) = \frac{1}{2} \int_\Omega \left[(1-\phi)^2 + l_c^2 \phi'^2 \right] d\Omega, \tag{13}$$

which can be written in another form with $d\Omega = \Gamma dx$,

$$I(\phi) = \frac{1}{2} \int_L \left[(1-\phi)^2 + l_c^2 \phi'^2 \right] \Gamma dx. \tag{14}$$

Substituting the proposed regularized phase equation (Eq. (11)) into Eq. 14 yields

$$I(\phi) = \Gamma l_c. \tag{15}$$

Eq. (15) connects the crack topology Γ with a functional $I(\phi)$ and the crack length scale l_c.

$$\Gamma_l = \frac{1}{2l_c} \int_\Omega \left[(1-\phi)^2 + l_c^2 \phi'^2 \right] d\Omega. \tag{16}$$

4.2.2 General description of the phase field model for a crack

In a general form,

$$\Gamma_l = \frac{1}{2l_c} \int_\Omega \left[(1-\phi)^2 + l_c^2 \left|\nabla\phi\right|^2 \right] d\Omega. \tag{17}$$

It was shown in [3] that the diffused crack reduces to a sharp discontinuity when the length scale $l_c \to 0$. Next for convenience, we introduce crack surface density γ, which relates that translate the crack surface geometry to the diffused crack domain.

$$\gamma = \frac{1}{2l_c}(1-\phi)^2 + \frac{l_c}{2} \left|\nabla\phi\right|^2. \tag{18}$$

$$\Gamma_l = \int_\Omega \gamma \, d\Omega. \tag{19}$$

Figure 40 depicts a crack with sharp interfaces is transformed to a diffused mush zone. Figure 41 gives an example of a regularized crack, where the phase field is obtained by solving Eq. (17). The size of the simulation domain Ω is 0.1×0.16 m, and the crack length is 0.025 m. $\phi = 0$ denotes the crack phase and $\phi = 1$ denotes the solid phase. Non-flux condition for phase field $\partial\phi/\partial\boldsymbol{n} = 0$ at all boundaries. A slut is installed and set $\phi = 0$ on its nodal points and $\phi = 1$ as the initial value for the remaining nodes. It can be seen that as the characteristic fracture thickness l_c increases, the larger the diffused crack zone.

Along the leftmost boundary, the distribution of the crack phase along the edge matches perfectly with the exponential distribution as proposed in the Eq. (11) (see Figure 42). As $l_c \to 0$, the crack is close to a sharp discontinuity.

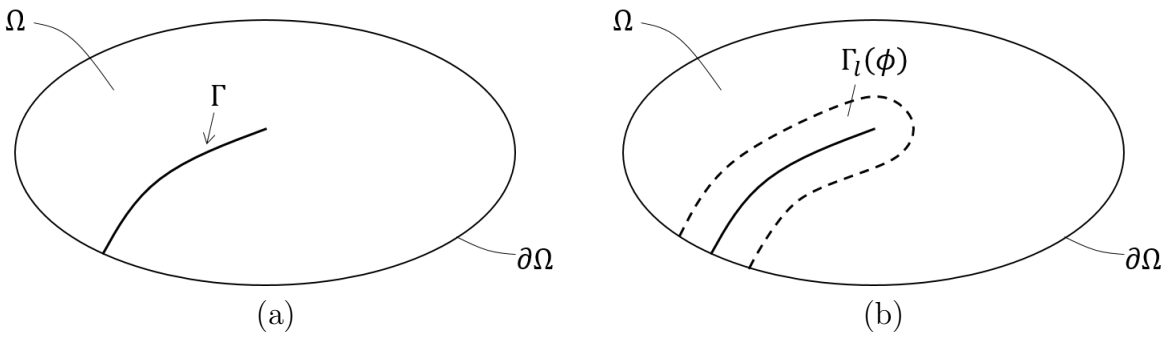

Figure 40: Crack regularization. (a) sharp crack, (b) diffused crack.

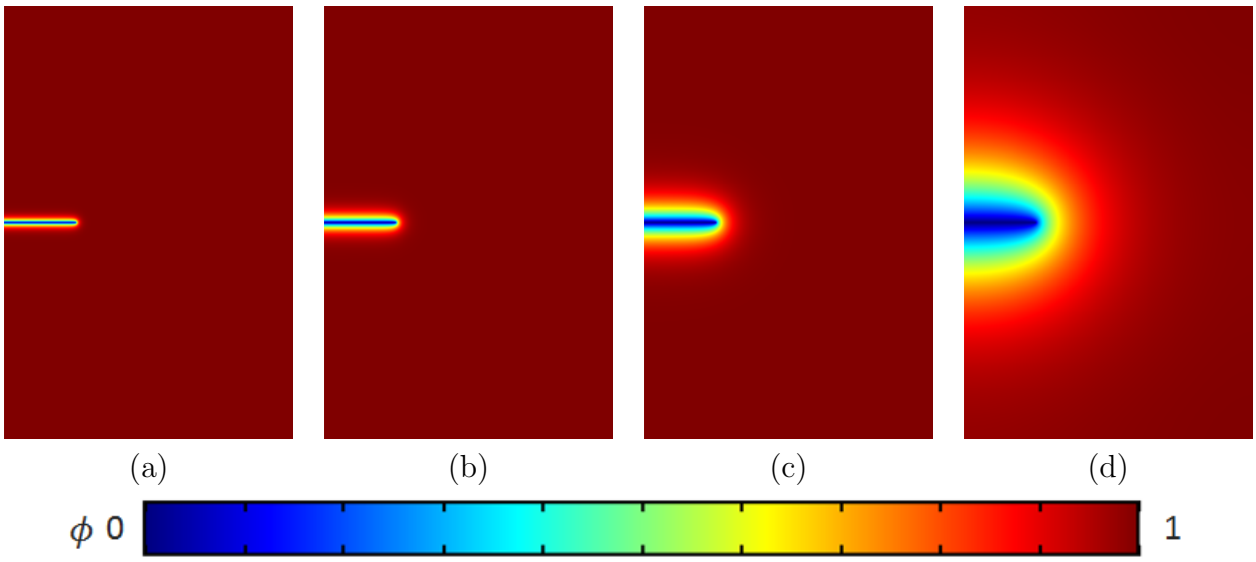

Figure 41: A regularized stationary crack Γ_l - with different length scales l_c: (a) 0.001 m, (b) 0.002 m, (c) 0.005 m, and (d) 0.02 m.

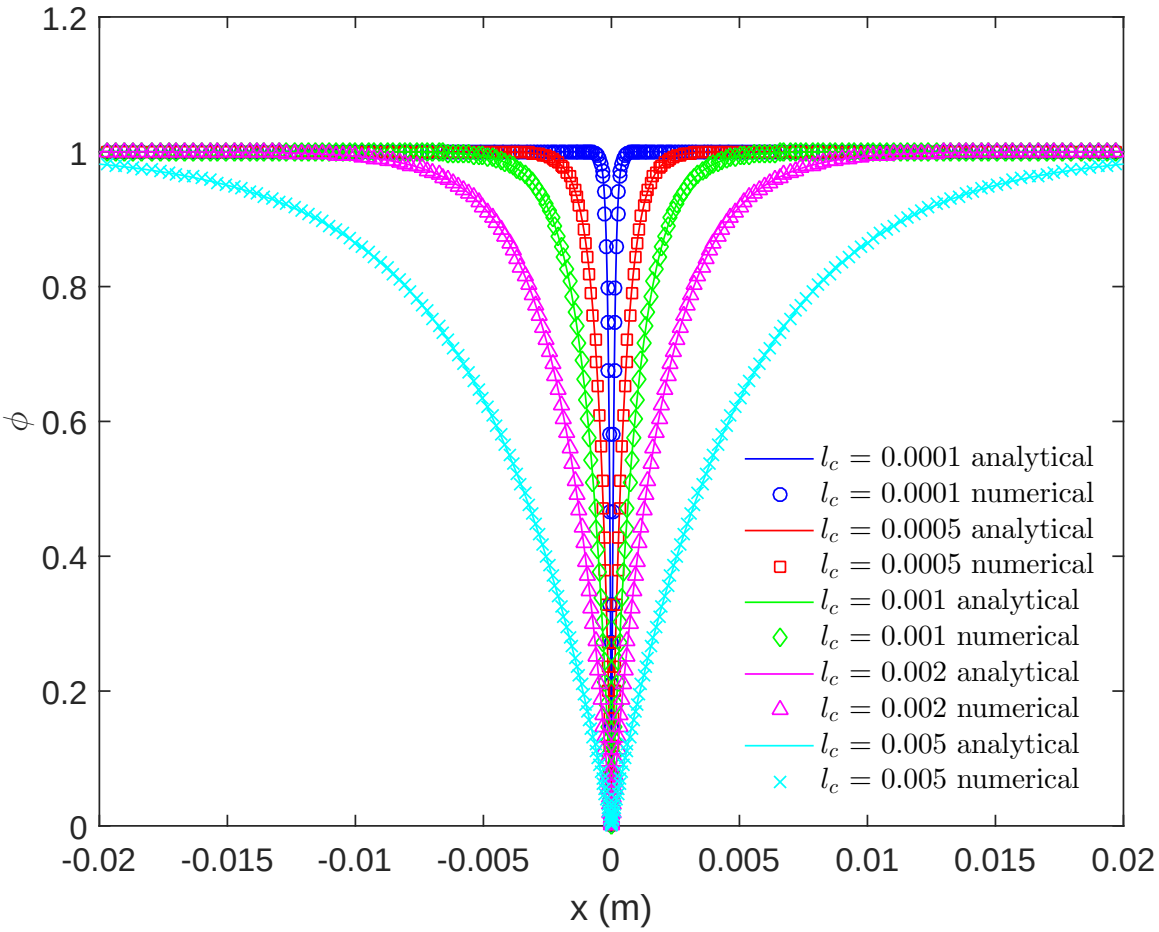

Figure 42: Diffused crack interface at 1D stationary crack with different length parameter l_c.

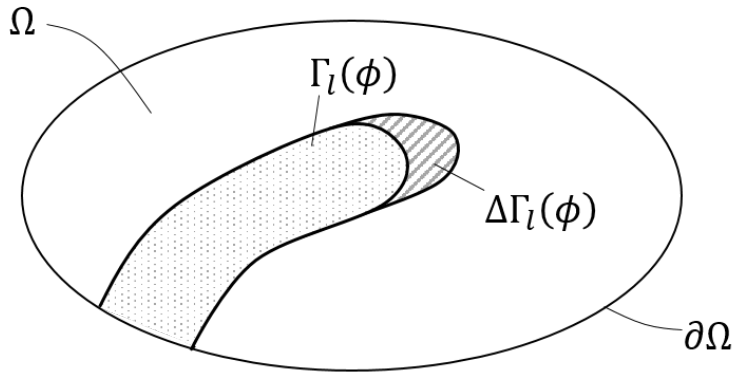

Figure 43: Growth of a diffused crack. Γ_l denotes a regularized crack at a given time t. $\Delta\Gamma_l$ denotes the increment of the crack as the crack propagates at time $t + \Delta t$.

4.2.3 Crack growth condition

Recall the crack geometry follows the expression in Eq. (19). The crack propagation can be written as,

$$\frac{d}{dt}\Gamma_l = \int_\Omega \frac{\partial \gamma}{\partial \phi}\frac{d\phi}{dt}\, d\Omega. \tag{20}$$

As crack propagates, the diffused zone grows near tip (see Figure 43). The increment in the area leads to positive sign of the left hand side of Eq. (20), i.e., $d\Gamma_l/dt \geq 0$. Phase transition always happens from solid to crack, i.e., ϕ always changes from 1 to 0, and therefore $\dot{\phi} \leq 0$. This constraint leads to an irreversible constraint:

$$\frac{\partial \gamma}{\partial \phi} \leq 0. \tag{21}$$

It follows from thermodynamics that crack formation is an irreversible process if no other physical process is introduced.

4.3 Formulation of the hybrid model

4.3.1 Weak form of viscous regularization

The phase field evolution equation can be given as non-conserved Ginsberg-Landau-type evolution as [82],

$$\frac{d\phi}{dt} = -M\frac{\partial \psi}{\partial \phi}, \tag{22}$$

whereψ is the total free energy density. For $\frac{\partial \psi}{\partial \phi} \geq 0$, since ϕ at the fracture tip decreases as the fracture propagates, the total free energy density ψ also decreases. Eq. (22) means that the crack propagates by maximizing the energy dissipation, i.e., the propagation direction is determined by where the gradient of dissipation is the largest. M is the mobility which determines the propagation speed, which is the reciprocal of viscosity, in an effect similar to cause damping of the propagation. The larger the mobility M, the faster the propagation speed [54]. For the case of $\frac{d\phi}{dt} = 0$, Eq. (22) reduces to quasi-stationary crack propagation condition following Griffith's

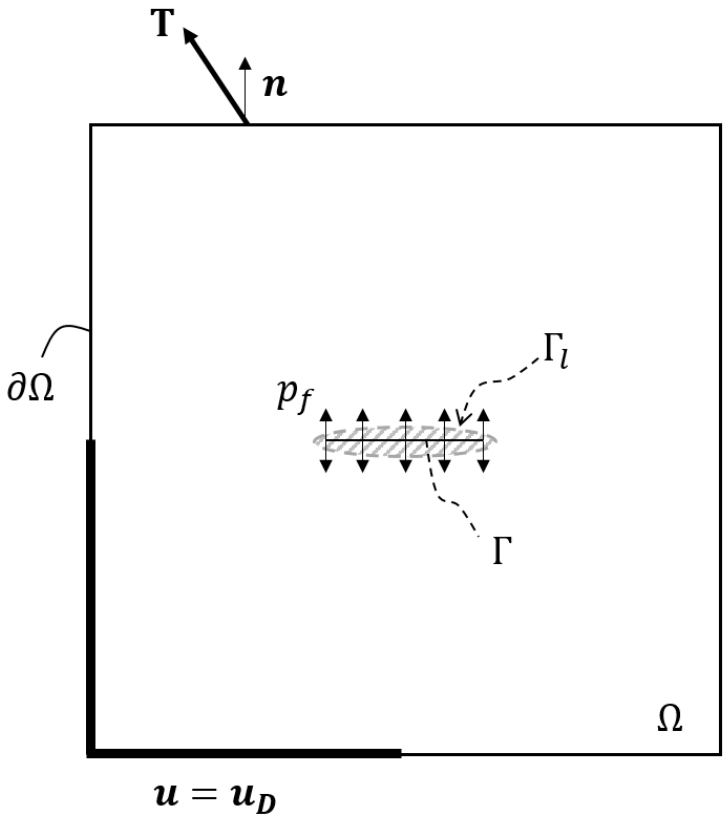

Figure 44: Schematic of a pressurized crack. **T** is the traction applied on the outer boundary, and the displacement boundary is specified as $u = u_D$.

theory. Especially for a pressurized crack as shown in Figure 44, the total free energy F of the system can be found as,

$$F = \int_{\Omega} \left[h\left(\phi\right) + s\right] \psi_0(\epsilon)\, dV - \int_{\Omega - \Gamma_l} \alpha p \nabla \cdot \boldsymbol{u}\, dV + G_c \Gamma - \int_{\Gamma_l} -p_f \boldsymbol{n} \cdot \boldsymbol{u}\, dA - \int_{\partial\Omega} \boldsymbol{T} \cdot \boldsymbol{u}\, dA, \tag{23}$$

$$F = \int_{\Omega} \psi\, dV. \tag{24}$$

$h(\phi)$ is a degradation function that degradation of the elastic energy where the crack is located. In general, a 4^{th} order weight function is chosen with the double well potential approach for the description of the phase field in solidification process [11, 13, 82] and the similar concept has been applied in fracture modeling [24, 35, 39, 51]. A simpler degradation function, which has been widely used [54, 56, 57, 70, 71, 73], is

$$h\left(\phi\right) = \phi^2. \tag{25}$$

which has properties that $h\left(0\right) = 0$, $h\left(1\right) = 1$, and $h'(0) = 0$. s can be chosen$0 \leq s \ll 1$ to avoid numerical calculation become ill-posed when $\phi = 0$. In our hybrid model, we found that the residual stiffness can be actually set to zero.$\psi_0\left(\epsilon\right)$ is the elastic energy density, which in an isotropic form is,

$$\psi_0\left(\epsilon\right) = \frac{1}{2} \boldsymbol{\sigma'} : \boldsymbol{\epsilon}. \tag{26}$$

$\boldsymbol{\sigma'}$ is the effective stress in the solid skeleton:

$$\boldsymbol{\sigma'} = \lambda \epsilon_{ii} + 2\mu \epsilon_{ij},\ i,\, j \in (1, 3). \tag{27}$$

λ and μ are Lamé constants. $G_c \Gamma_l$ is the fracture surface energy. If apply the regularized crack form Γ_l, we can introduce the fracture energy density ψ_f stored the regularized crack zone as,

$$G_c \Gamma_l = \int_{\Omega} \psi_{frac}\, d\Omega, \tag{28}$$

and

$$\psi_f = G_c \gamma. \tag{29}$$

The work of fluid pressure inside the crack is

$$W_{fluid} = \int_{\Gamma_l} -p_f \boldsymbol{n} \cdot \boldsymbol{u}\, dA. \tag{30}$$

p_f is the fluid pressure inside the fracture. We note that, indeed, by creating $\phi = 0$, at a line segment inside the domain, due to $\underline{u = 0}$ at the segment, no work is done by the boundary pressure. However, by integrating the diffused zone, the work done by the boundary pressure can be created. From Gauss divergence theorem,

$$W_{fluid} = \int_{\Omega - \Gamma_l} -\nabla \cdot (p_f \boldsymbol{u})\, dV. \tag{31}$$

In order to take into consideration of the phase variation in the domain, we here choose the same degradation functional $h(\phi)$ in Eq. (25) to include the fracture phase to the entire domain:

$$W_{fluid} = \int_{\Omega} -h(\phi)\, \nabla \cdot (p_f \boldsymbol{u})\, dV. \tag{32}$$

The second term in Eq. (23) is the energy contribution from the work done by pore pressure. Similar to the degrading the work done by the fluid pressure inside fracture, we can use degradation function $h(\phi)$ to interpret the energy contribution from pore pressure p, i.e.,

$$\int_{\Omega - \Gamma_l} \alpha p \nabla \cdot \boldsymbol{u}\, dV = \int_{\Omega} h(\phi)\, \alpha p \nabla \cdot \boldsymbol{u}\, dV \tag{33}$$

α is the Biot coefficient, which relates the total stress to the effective stress and the pore pressure (tensile positive) through

$$\boldsymbol{\sigma} = \boldsymbol{\sigma}' - \alpha p \boldsymbol{I}. \tag{34}$$

Substitute all into Eq. (22) and integrate with an admissible test function $\delta\phi$ to a weak form,

$$\int_{\Omega} \dot{\phi} \delta\phi\, dV = -M \left[\int_{\Omega} 2\phi \frac{1}{2} \boldsymbol{\sigma}' : \boldsymbol{\epsilon} \delta\phi\, dV - \int_{\Omega} 2\phi \alpha p \nabla \cdot \boldsymbol{u} \delta\phi\, dV + \int_{\Omega} 2\phi \nabla \cdot (p_f \boldsymbol{u})\, \delta\phi\, dV \right.$$
$$\left. + \int -\frac{G_c}{l_c} \left((1-\phi)\, \delta\phi - l_c^2 \nabla\phi \cdot \nabla\delta\phi \right)\, dV \right]. \tag{35}$$

In the case of quasi-stationary crack propagation problem ($d\phi/dt = 0$),

$$\int_\Omega 2\phi\psi_0(\epsilon)\delta\phi\, dV - \int_\Omega 2\phi\alpha p\nabla\cdot\boldsymbol{u}\delta\phi\, dV + \int_\Omega 2\phi\nabla\cdot(p_f\boldsymbol{u})\,\delta\phi\, dV + \int_\Omega -\frac{G_c}{l_c}\left((1-\phi)\,\delta\phi - l_c^2\nabla\phi\cdot\nabla\delta\phi\right)\, dV = 0. \quad (36)$$

which reproduces the formula devised by Mikelić [73, 74].

The elastic energy term (Eq. (26)) cannot differentiate whether the energy done by compression or tension, which could lead to unrealistic crack propagation. Such *isotropic* model can be modified with the *anisotropic* model presented by Miehe [70], i.e., separating energy into compression part and tension part. We also note here that the split algorithm can also follow by the work by Amor [4]. We here follow the anisotropic model by Miehe, which presents:

$$\psi_0(\epsilon) = (h(\phi)+s)\psi_0^+(\epsilon) + \psi_0^-(\epsilon). \quad (37)$$

$$\psi_0^\pm(\epsilon) = \frac{1}{2}\left(\lambda\left\langle\epsilon_{ii}\right\rangle_\pm^2 + \mu\left\langle\epsilon_{ij}\right\rangle_+\left\langle\epsilon_{ij}\right\rangle_+\right), \quad (38)$$

where $\langle\epsilon_{ij}\rangle_\pm$ is defined as,

$$\left\langle\epsilon_{ij}\right\rangle_\pm = \sum_{k=1}^{D}\left\langle\epsilon^k\right\rangle_\pm n_i^k\otimes n_j^k. \quad (39)$$

D =1, 2, 3. ϵ^k are the eigenvalues of the strain tensor, and n_i^k are the corresponding eigenvectors. Operator $\langle\ \rangle_\pm$ stands for the operation:

$$\left\langle z\right\rangle_\pm = \frac{(z\pm|z|)}{2}. \quad (40)$$

z is a random real number. The energy split in Eq. (37) with the degradation function only attached in tensile failure ensures the fracture propagates only under tensile condition. This can be verified easily by substituting the equation into the evolution equation (Eq. (22)) so that the compression part of energy contribution to the propagation is zero.

Considering the irreversible condition of the crack phase $d\phi/dt \leq 0$, the propagation can be expressed as,

$$\dot{\phi} = -M \left\langle \frac{\partial \psi}{\partial \phi} \right\rangle_+ , \tag{41}$$

where $\langle z \rangle_+ = (z + |z|)/2$ enforces the irreversible condition $d\phi/dt \leq 0$.

In order to satisfy the irreversible evolution Eq. (41), we followed the work presented by Miehe [71] to introduce a local history maximum H, which has the form:

$$H\left(\boldsymbol{x}, t^{n+1}\right) = \begin{cases} \psi_0^+(\epsilon\left(\boldsymbol{x}, t^{n+1}\right)), & \psi_0^+(\epsilon\left(\boldsymbol{x}, t^{n+1}\right)) > H \\ H\left(\boldsymbol{x}, t^n\right), & otherwise \end{cases} . \tag{42}$$

t^{n+1} is the current time step and t^n is the previous time step. It has been proved that the use of the application of maximum history field automatically satisfies the irreversible condition in Eq. (41) [71]. So the final form of the evolution equation of the phase field becomes,

$$\frac{1}{M}\dot{\phi} = -\left[h'\left(\phi\right) H - h'\left(\phi\right) \alpha p \nabla \cdot \boldsymbol{u} + h'\left(\phi\right) \nabla \cdot \left(p_f \boldsymbol{u}\right) + G_c \frac{\partial \gamma}{\partial \phi}\right]. \tag{43}$$

The first term on the right side of the Eq. (43) is the driving force from the elastic storage, the second is from pore pressure, the third is from the fluid pressure inside fracture, and the last term is the resistance of the fracture. Here we are only interested in the total stress response, the phase field evolution equation can be simplified into,

$$\eta\dot{\phi} = -\left[h'\left(\phi\right) H + h'\left(\phi\right) \nabla \cdot \left(p_f \boldsymbol{u}\right) + G_c \partial_\phi \gamma\right]. \tag{44}$$

$$G_c \partial_\phi \gamma = -G_c \left(\frac{1}{l_c}\left(1 - \phi\right) + l_c \Delta \phi\right) \tag{45}$$

The weak form of the final phase field equation applied in the current model is then,

$$\int_\Omega \dot{\phi} \delta\phi \, dV = -M \left[\int_\Omega 2\phi H \delta\phi \, dV + \int_\Omega 2\phi \nabla \cdot \left(p_f \boldsymbol{u}\right) \delta\phi \, dV + \int -\frac{G_c}{l_c}\left(\left(1 - \phi\right)\delta\phi - l_c^2 \nabla\phi \cdot \nabla\delta\phi\right) dV\right]. \tag{46}$$

4.3.2 Force equilibrium

Since we are interested in quasi-static fracture propagation problem, the stress equilibrium is (neglecting body force),

$$\nabla \cdot \boldsymbol{\sigma} = 0 \tag{47}$$

The total stress in the form of energy splitting [70] is

$$\boldsymbol{\sigma} = h(\phi)\frac{\partial \psi^{+}}{\partial \boldsymbol{\epsilon}} + \frac{\partial \psi^{-}}{\partial \boldsymbol{\epsilon}}. \tag{48}$$

It was pointed out that an alternative phenomenological stress formula can be used to increase the computational efficiency and meet a reasonable agreement [2], i.e., take the isotropic stress form, while adding a phase field constraint when $\psi_0^- > \psi_0^+$ to preserve the feature of tensile failure only. More specifically, we can set the phase field $\phi = 1$ so that when compression dominates, the material will not be degraded to lose its stiffness. This is so called "hybrid model" where the stress is in isotropic formula, while the phase field evolution is still governed by the tensile failure only. The advantage of such model is the linear form of the stress equilibrium equation, which reduces the computational cost [2]. The hybrid model is,

$$\boldsymbol{\sigma} = g(\phi)\frac{\partial \psi}{\partial \boldsymbol{\epsilon}}. \tag{49}$$

$$g(\phi) = \begin{cases} 1, & \forall \boldsymbol{x} : \psi_0^- (\epsilon) > \psi_0^+ (\epsilon) \\ h(\phi) + s, & otherwise \end{cases}. \tag{50}$$

For simple cases, where there is applied monotonic loading like pure tension or compression, Eq. (50) resembles the same formulation as Eq. (37). We note that for single-edge notched shear tests, the hybrid model delivers an intermediate results between isotropic and anisotropic model [2].

Regarding to the weak form for the virtual work of the system,

$$\int_{\partial\Omega} T \cdot \delta \boldsymbol{u}\, dA = \int_{\Omega} g\left(\phi\right) \boldsymbol{\sigma} : \boldsymbol{\epsilon}(\delta \boldsymbol{u}) + \min\left(h\left(\phi\right), 1\right) \nabla \cdot \left(p_f \delta \boldsymbol{u}\right)\, dV \tag{51}$$

The constraint $\min\left(h\left(\phi\right), 1\right)$ works as the cut-off of the phase field to be bounded by [0, 1] for the purpose of minimizing numerical error.

4.4 Computational algorithm

The weak form equations Eq. (46) and (51) are then implemented into COMSOL solver. We use the segregated scheme to decouple the problem. The overall algorithm of simulation process are provided in Figure 45.

4.5 Verification of the model

4.5.1 Selection of crack diffused length scale l_c and mesh

Mesh has been identified the most sensitive to capture the sharp gradient at crack interface both in our work and in literature. As aforementioned, the length scale l_c should be large enough to approximate the real crack, and should be big enough for the consideration of the capability of computation. However, if l_c is too large, the crack will be over-dissipated to the domain, so the sharp discontinuity nature of the crack is lost. It has been found that the mesh size should be at least $1/2\, l_c$ to conserve the accuracy of the dissipated crack topology [70]. The sharp crack interface only affects the zone near the crack.

4.5.2 An edge crack in a plate subjected to uniaxial tension

The first verification problem is the problem of an edge crack in a plate subjected to tension in the far-field (see Figure 46).the popularized Mode I fracture propagation. The simulation results are compared to the critical tensile strength [31]. The model follows the setup in [54]. The characteristic length l_c is set to be 0.000625 m ($l_{cD} = 0.025$) and the mesh size h_{max} is set to $1/2l_c$ in the zone where the fracture propagates. Free triangular mesh is selected as the base mesh element for the model.

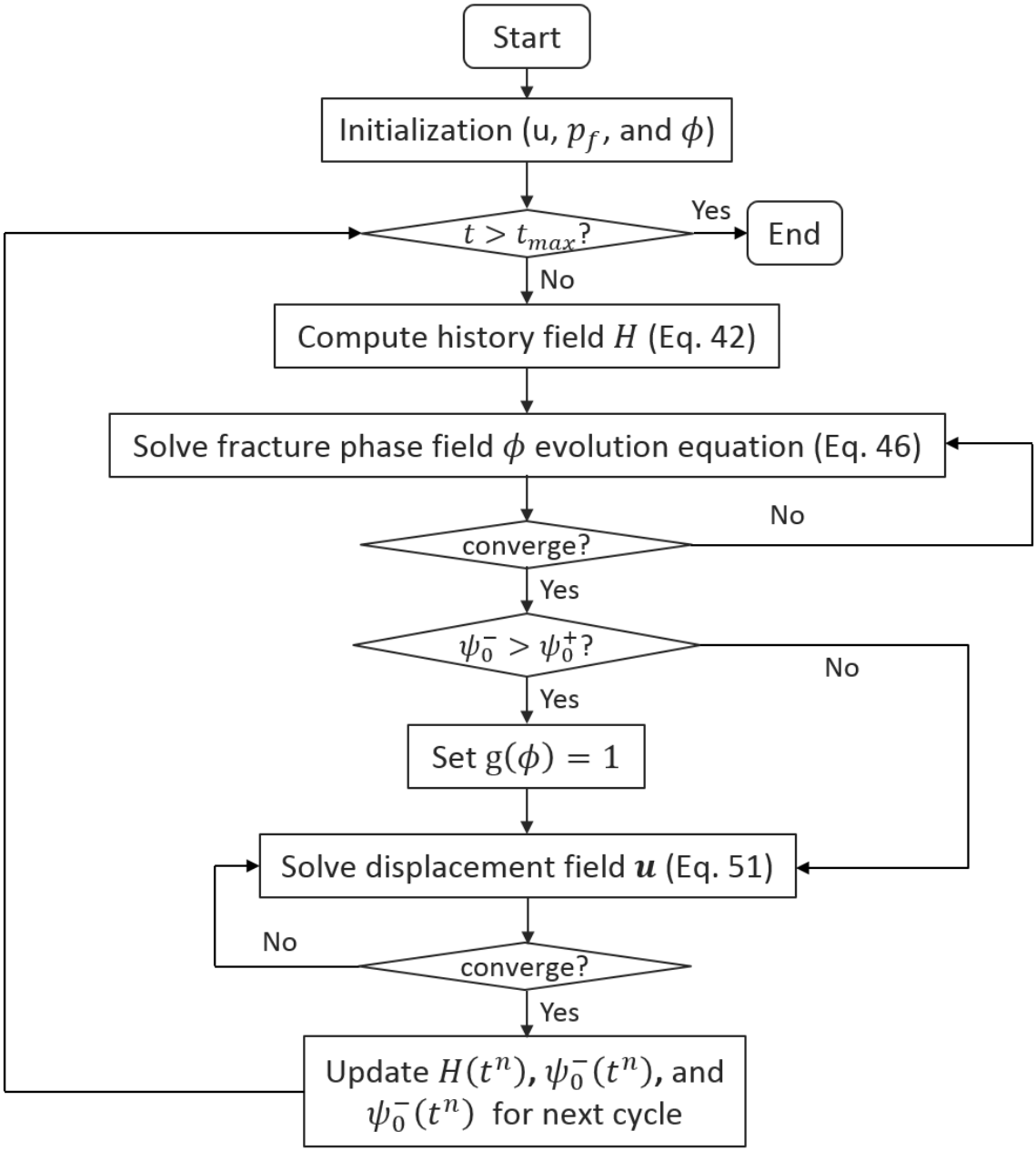

Figure 45: Solution scheme for the pressurized fracture propagation

The other domains are set with coarse mesh in the consideration of reducing degree of freedom in calculation. A line segment is created with phase field variable $\phi = 0$ on its nodal points to indicate a pre-installed crack. the initial crack to indicate the crack phase, and non-flux condition for the phase variable at the outer boundary. For the boundary conditions, constant stress loading is applied on the top and the bottom of the specimen with a loading rate of $\dot{\sigma} = 6$ MPa/s, and a fixed displacement condition at the crack to add the transnational and rotational constraints. This is different with the model in [54], where the symmetric condition is used, so that the 1/2 of the model is analyzed. The Lamé parameters of the model is $\lambda = \mu = 2.2 \times 10^{10}$ Pa. The mobility M is set to be 5×10^{-4} $1/(\text{Pa} \cdot \text{s})$. The residual stiffness ratio s is set to 10^{-5} for the sake of consistency with the literature. The crack initiation time is measured when the phase field ϕ of the first node in front of the crack tip falls below threshold $\phi_{thr} < 0.05$.

In a finite plate, the critical stress under a certain value of G_c can be evaluated as (see Table 2.4 in [5]),

$$f\left(\frac{a}{b}\right) = \frac{0.752 + 2.02\frac{a}{b} + 0.37\left(1 - \sin\left(\frac{\pi a}{2b}\right)\right)^3}{\cos\left(\frac{\pi a}{2b}\right)}. \tag{52}$$

$$\sigma_c = \sqrt{\frac{E}{1-\nu^2}\frac{G_c}{2b\tan\left(\frac{\pi a}{2b}\right)}} f^{-1}\left(\frac{a}{b}\right). \tag{53}$$

Correspondingly, the critical time for crack initiation is,

$$t_c = \frac{\sigma_c}{\dot{\sigma}}. \tag{54}$$

The numerical results are in good agreement with the analytical solution (see Figure 48). The slight difference can be either caused by numerical errors or the scale of l_c.

Propagation of the edge crack is shown in Figure 49. It can be identified that mobility M controls the speed of fracture propagation, as discussed in [54]. The more viscous regularization (smaller mobility M) causes the more damping in the fracture propagation so that it delays the propagation.

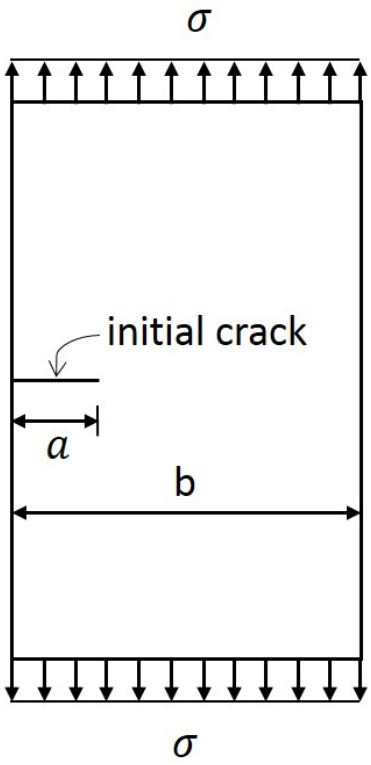

Figure 46: Mode I tensile test with constant stress loading. The size of the simulation domain is 0.1×0.16 m (width×height) with a crack length of 0.025 m. Crack initial length $a = b/4$. Two tensile stress is applied on the top and the bottom to tear apart the specimen, and the displacement field at initial crack is fixed.

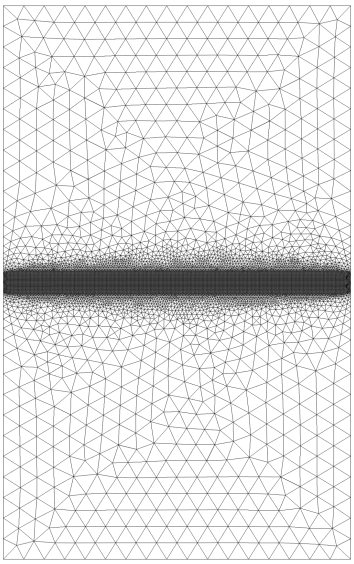

Figure 47: Mesh setup for Mode I tensile test.

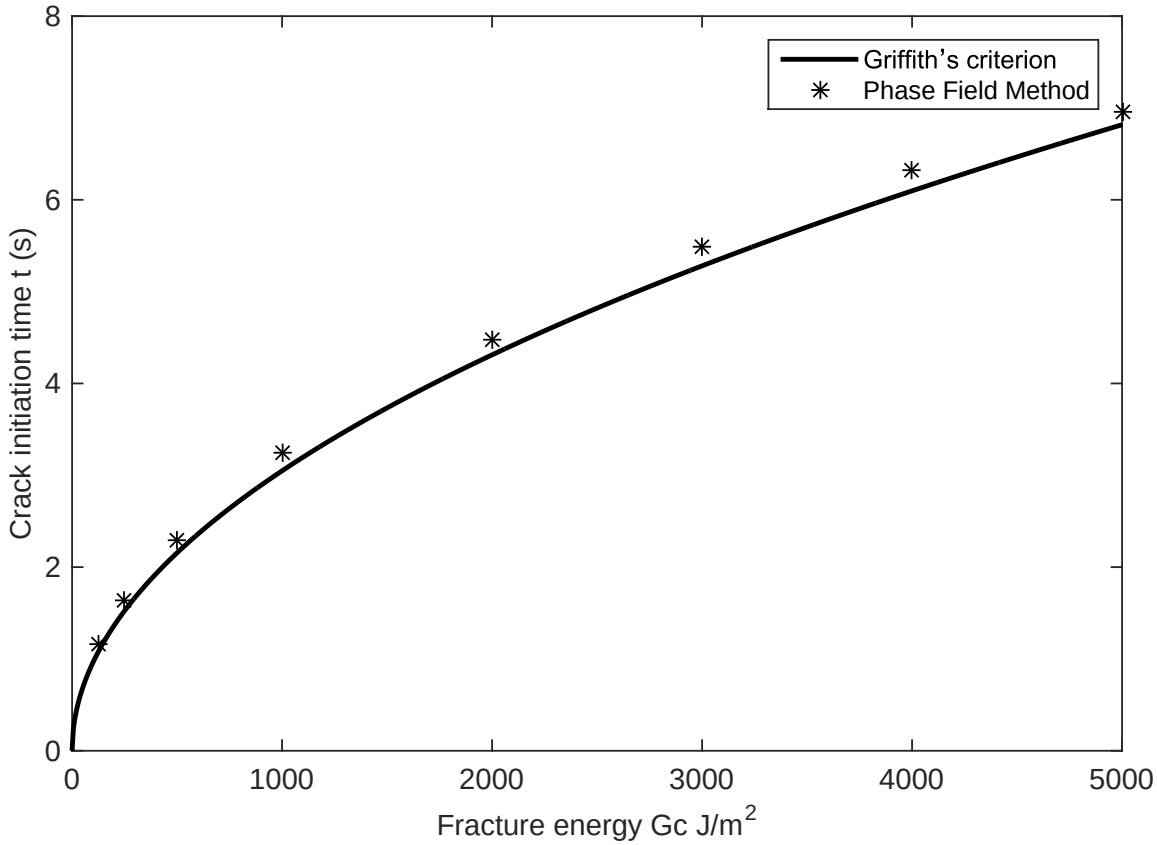

Figure 48: Crack initiation time t (s) for different values of fracture energy G_c (J/m^2) with a loading rate of 6 MPa/s. The critical stress is determined when the phase field ϕ of the first node in front of the crack tip.

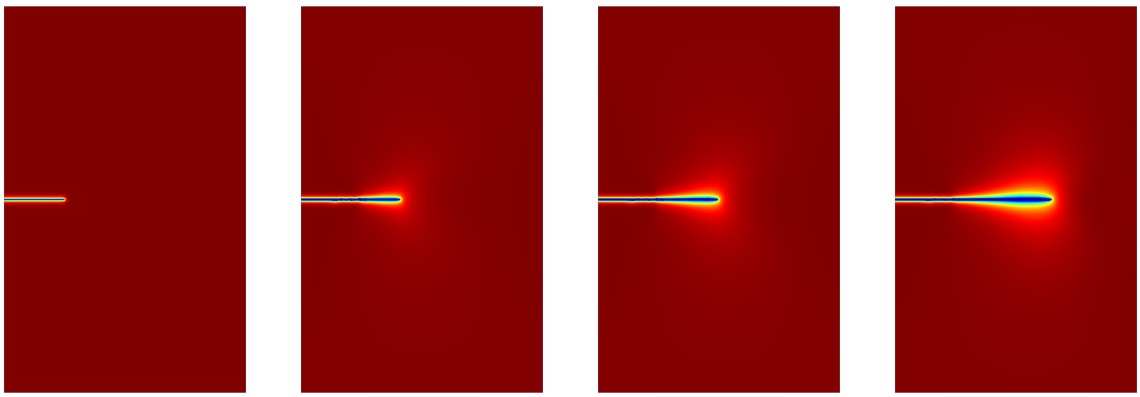

(1a) (1b) (1c) (1d)

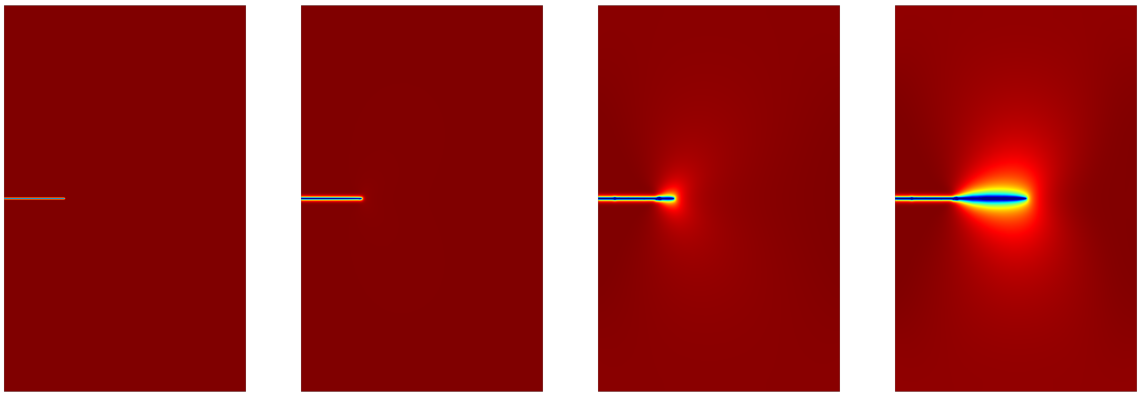

(2a) (2b) (2c) (2d)

Figure 49: Crack propagation under tension. For series 1, the mobility is set to 5×10^{-4} $\frac{1}{Pa \cdot s}$, and for series 2, the mobility is 5×10^{-7} $\frac{1}{Pa \cdot s}$. The color scheme is same as Figure 41, where the dark blue indicates the crack phase $\phi = 0$, and the dark red indicates the solid phase $\phi = 1$. The time snapshot for the series 1 are: (1a) 0.10 s, (1b) 1.28 s, (1c) 1.29 s, and (1d) 1.296 s. For series 2: (1a) 0.10 s, (1b) 1.28 s, (1c) 2.70 s, and (1d) 3.25 s.

4.5.3 Constant displacement tests: Mode I and Mode II

This section is to show the capability of the phase field method in simulating the process of crack initiation and propagation without setting the phase field variable $\phi = 0$ as an initial condition. In other words, algorithm allows the phase field to transit from a pure solid phase to a crack phase only based on the evolution equations and boundary conditions. The model follows the setup in [70]. Unlike the previous case by inserting a line segment with phase field variable $\phi = 0$ as the pre-installed crack, a slot notch is created with finite thickness $(l_c/2)$ while the initial condition of the phase field of the entire material domain is $\phi = 1$. A constant displacement rate of 10^{-5} mm/s is applied at the top of the specimen. Roller support is placed at the bottom. Mobility M is set to be 10^{-5} $1/(\text{Pa} \cdot \text{s})$ to capture the propagation. The Lamé parameters of the model is $\lambda = 121.15$ GPa, $\mu = 80.77$ GPa. The critical energy release rate G_c is set to 2.7 KJ/m^2. Figure 51 shows the transition of the phase field from pure solid to crack phase once the energy release rate exceeds a critical value of G_c.

For Mode II shear test, the model setup and boundary conditions are described in Figure 52. The unrealistic fracture propagation is also mentioned in [2, 4, 70]. Isotropic model results in a bifurcated fracture in Figure 53(1a) - (1d). The upper part is the unrealistic fracture creation from from compression, and the lower part is the fracture creation from tensile.

4.5.4 Verification: stationary crack opening

The verification of the crack opening is discussed. The model setup is depicted in Figure 54. The domain is set to be large enough that the infinite domain assumption holds. Symmetric boundary condition is applied at the bottom, and fixed displacement condition at the remaining boundaries. $E = 10^6\ Pa$, $\nu = 0.25$, and $p_f = 1\ kPa$.

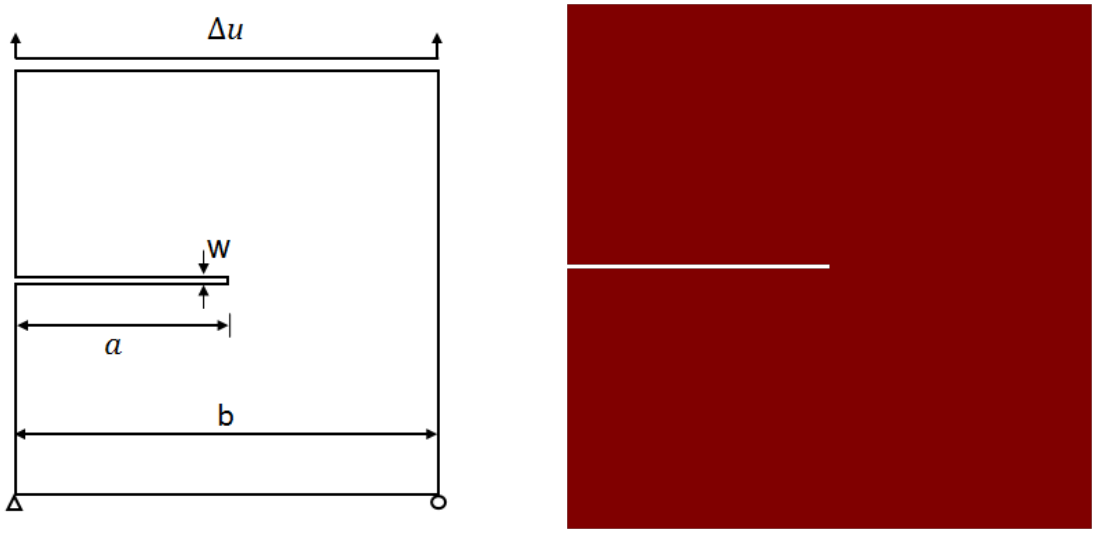

(a) (b)

Figure 50: Constant displacement test setup. (a) model setup, (b) initial condition of the phase field. The color scheme for the phase field is same in Figure 41. The red color interprets $\phi = 1$ that the domain initially contains solid phase only. The simulation domain Ω is 1×1 mm, the crack size $a = 1/2\, b$, and the thickness of the crack $w = l_c/2$. The characteristic length of the crack is given as $l_c = 0.015$ mm.

By setting phase field variable equals to fracture phase $\phi = 0$ indicating the discontinuity, does not generate the discontinuity in displacement field. However, because of the diffused crack zone, the crack opening displacement can be approximated by the following two methods.

1. Crack opening displacement can be approximated to the vertical displacements at a location of $1/2\ l_c$ above the crack elements.

2. Crack opening displacement can be approximated as that suggested by Bourdin [10], where the displacement is defined as, $v = \int_{-\infty}^{+\infty} \boldsymbol{u}(x, y) \cdot \nabla\phi\, dy$.

The numerical results are then compared with Sneddon's solution [89],

$$v = \frac{2p_f a}{E'} \left(1 - \frac{x^2}{a^2}\right)^{1/2}, \tag{55}$$

where v is the vertical displacement, and E' is the plane strain modulus, $E' = E/(1-\nu^2)$.

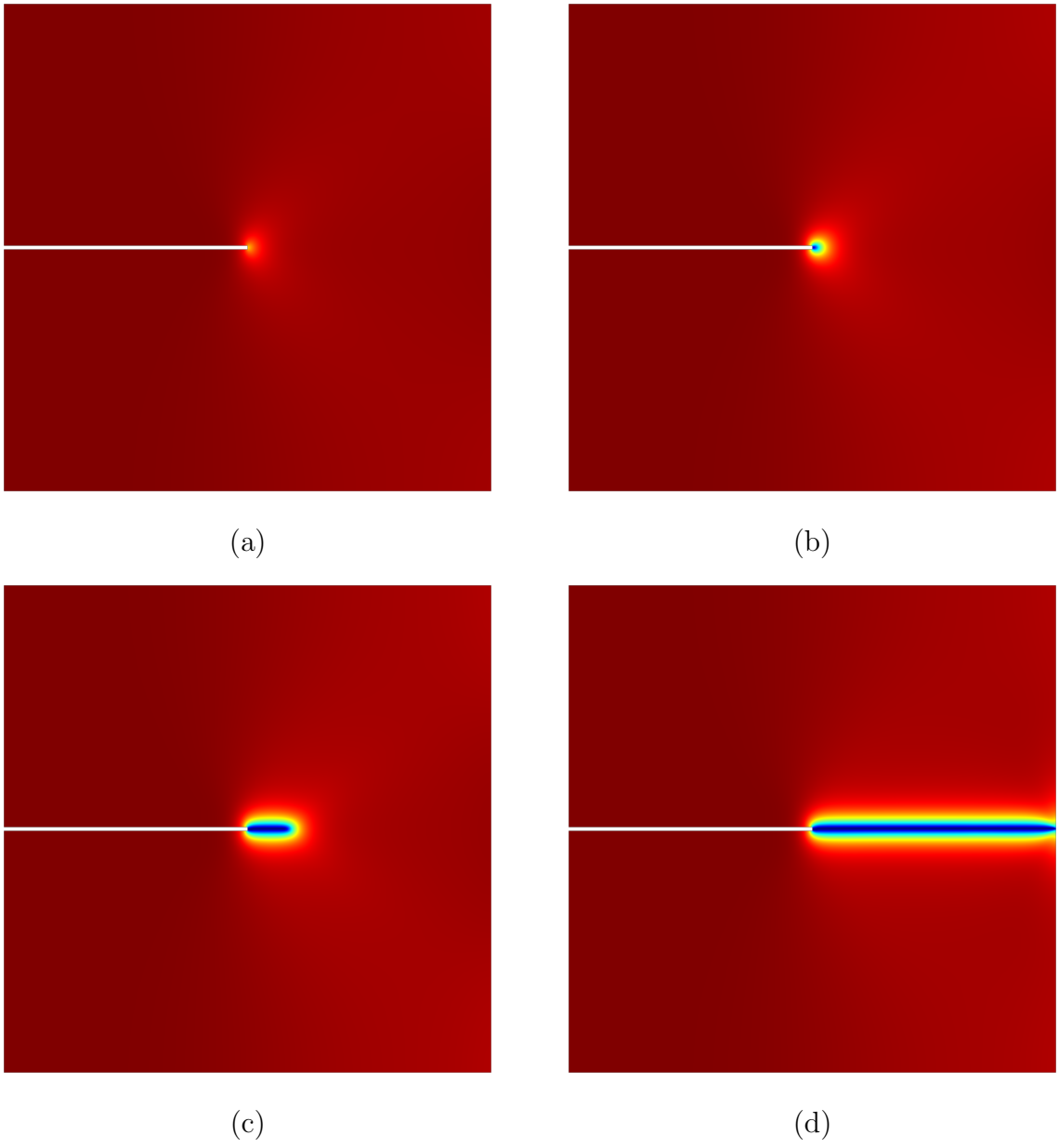

Figure 51: Simulation results for constant U Mode I tensile test. Figures are the snap shot of the displacement of the top plate at (a) 4×10^{-3} mm, (b) 4.65×10^{-3} mm, (c) 4.6501×10^{-3} mm, and (d) 4.6506×10^{-3} mm. The color scheme is the same as the Figure 41. It can be seen that the gradual change in phase field from solid phase to crack phase as the displacement loading increases.

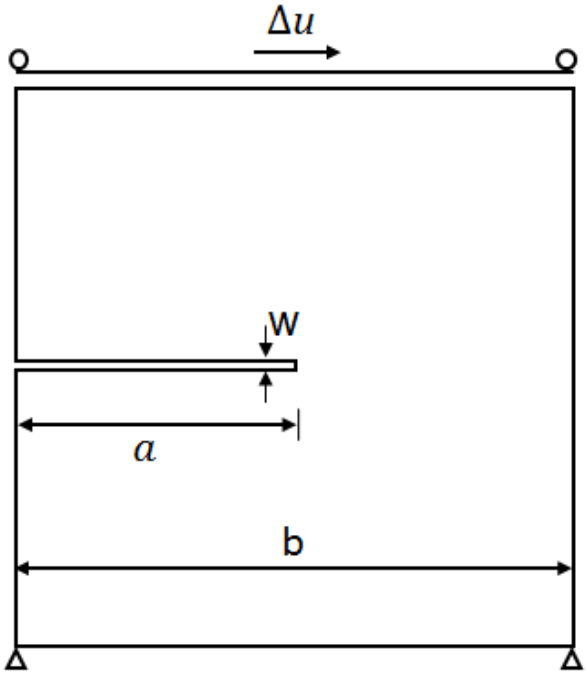

Figure 52: Constant U Mode II shear test setup. The material properties are identical to constant U Mode I tension test. The characteristic length scale l_c is 0.015 mm ($l_{cD} = 0.03$). The maximum element size in the zone of interest is $l_c/5$ for isotropic case and $l_c/2$ for hybrid. For the boundary conditions of displacement field, the bottom plate is completely fixed, and the top plate is roller support with a displacement rate of 10^{-5} mm/s. Non-flux condition for all boundaries for phase field.

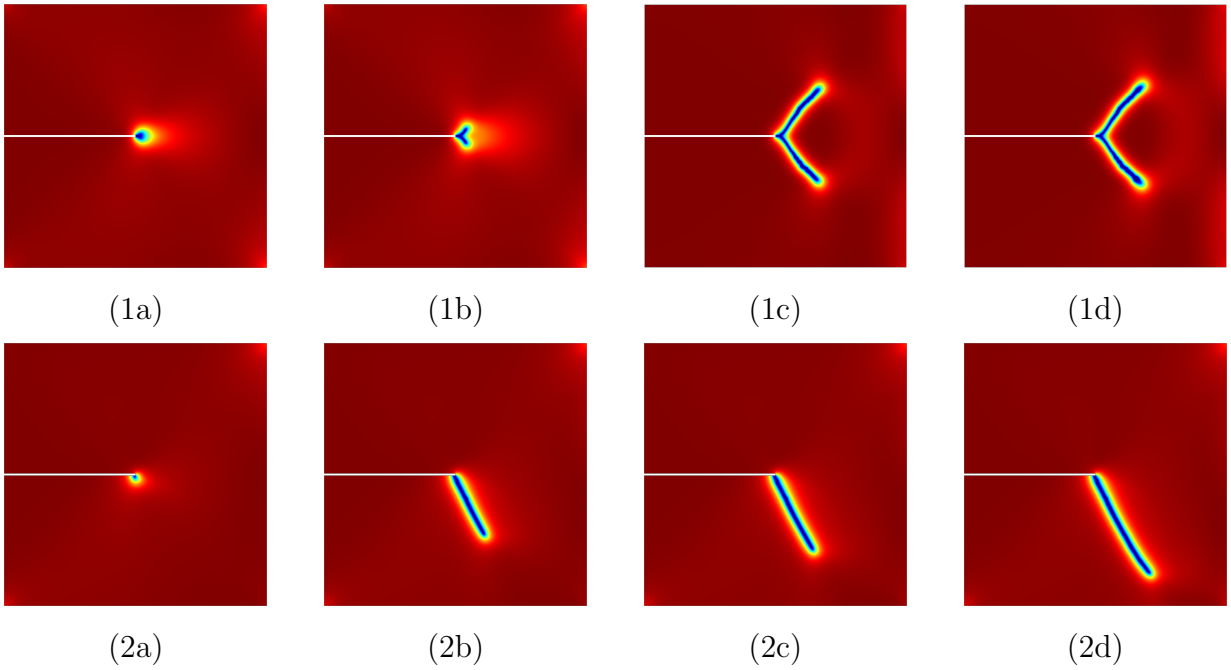

Figure 53: Mode II shear tests. Series (1) isotropic, (2) hybrid at horizontal displacement of (a) 9.9×10^{-3} mm, (b) 1.1×10^{-2} mm, (c) 1.2×10^{-2} mm, (d) 1.4×10^{-2} mm.

The corresponding study of the effect of l_c and the mesh size effect are presented in Figure 56 - 58. Namely, at the larger l_c settings, a more diffused crack can lead to the existence of a non-zero opening at the real crack tip. As $l_c \to 0$, the crack opening displacement at the crack tip falls toward zero and agrees the theoretical solution for brittle fractures [89]. However, a smaller l_c requires the use a finer mesh to indicate the maximum displacement at the center. If we are interested in the maximum opening displacement, it might be unnecessary to have a extremely fine mesh for certain characteristic l_c values. For instance, in the case $l_c = 0.02$ m in Figure 56, when finding the maximum opening displacement, a mesh size of $1/4\, l_c$ is the optimum, a mesh size of $1/10\, l_c$ produces overestimates, and a mesh size of $1/2\, l_c$ produces underestimates. When a smaller l_c is assigned to present the diffused crack (compare the cases of mesh size $1/2\, l_c$ in Figure 56-58), the required mesh is even finer. Indeed, it is more accurate use an infinitely small l_c to get rid of the artificial crack tip displacement, but from the perspective of computational cost, it

might be in an acceptable range of study by using a large l_c but small enough with a corresponding reasonable mesh size.

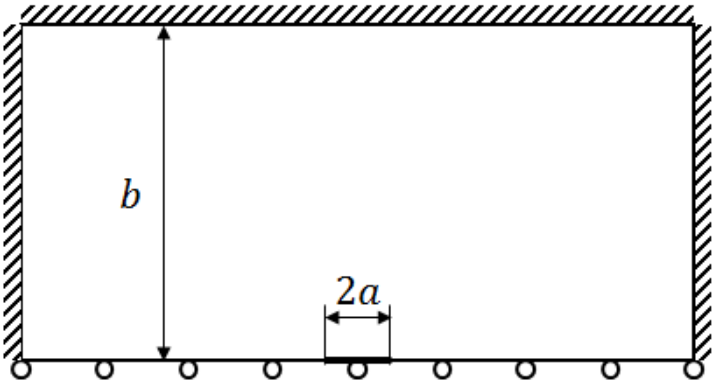

Figure 54: Model setup. Half domain size 0.5×1 m (height×width) with a half crack length of $a = 0.05$ m.

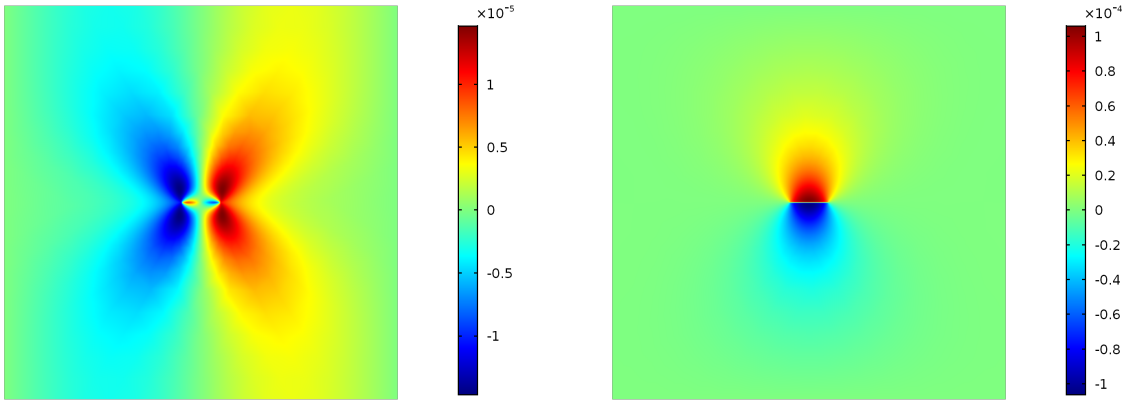

(a) (b)

Figure 55: Displacement field $\boldsymbol{u}$ of a fluid filled fracture with $l_c = 0.02$ m ($l_{cD} = 0.2$). (a) horizontal displacement, (b) vertical displacement. The crack is included in mesh. The continuous domain generates a similar result of discontinuous crack opening displacement.

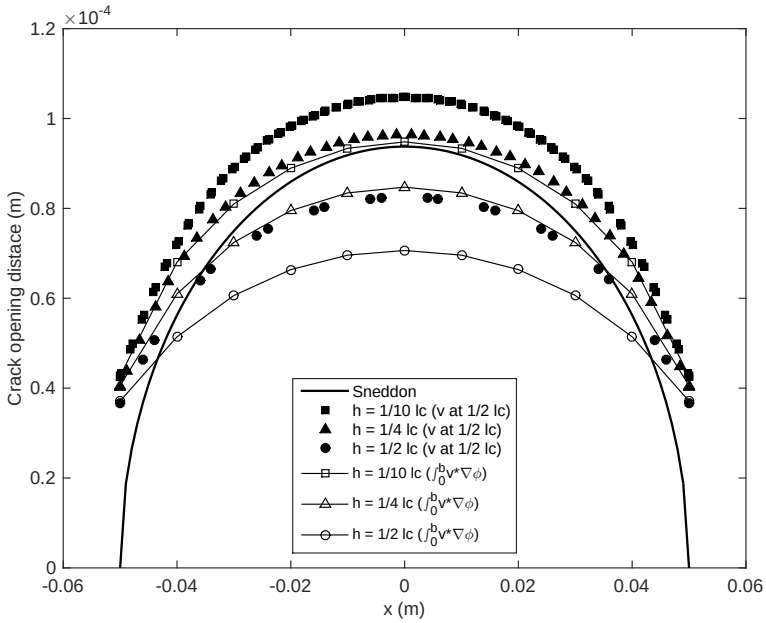

Figure 56: Crack opening displacement - $l_c = 0.02\ m$.

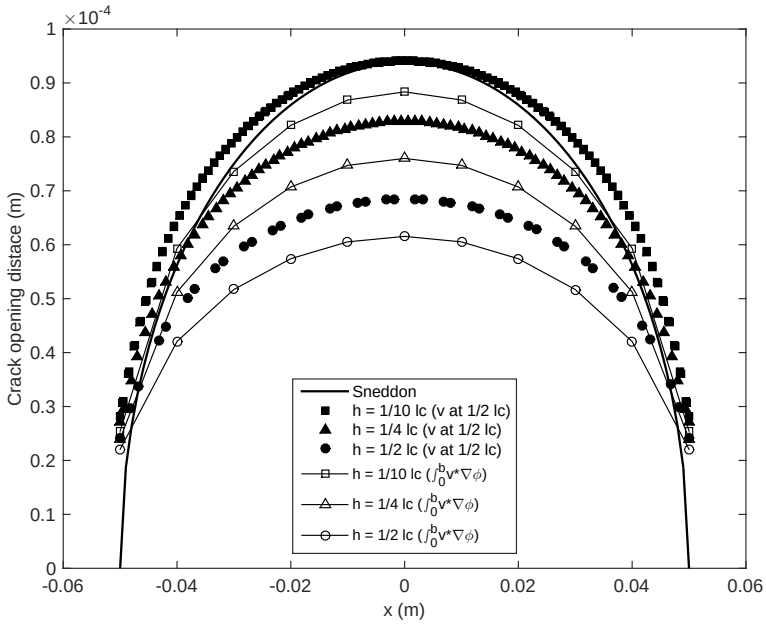

Figure 57: Crack opening displacement - $l_c = 0.01\ m$ ($l_{cD} = 0.1$).

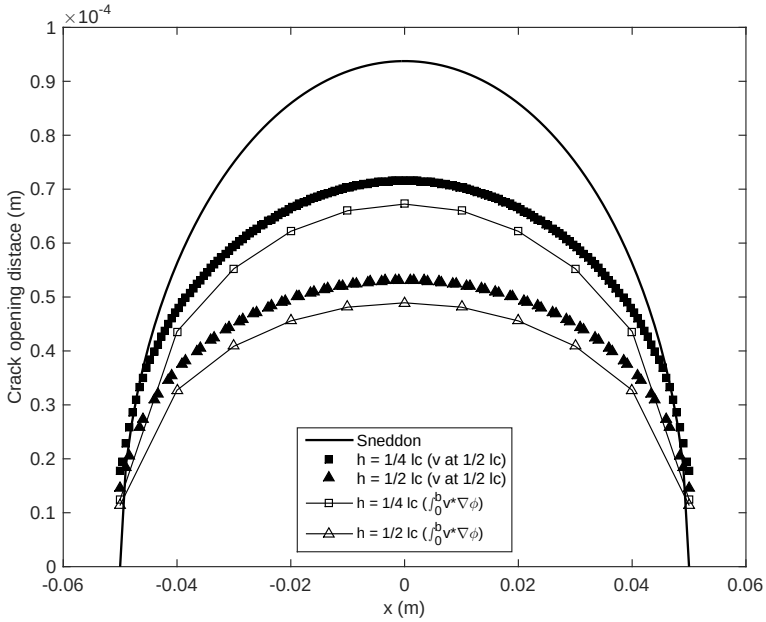

Figure 58: Crack opening displacement - $l_c = 0.005\ m$ ($l_{cD} = 0.05$). $h = 1/10\, l_c$ is not provided since it reaches the limit of the feasible element numbers.

4.6 Numerical tests

4.6.1 Pressurized inclined crack

The first simulation of pressurized fracture growth is analyzed under biaxial far field confining stress condition. The corresponding model setup and parameters are provided in Figure 59. The fluid pressure gradually increases at a rate of 0.1 MPa/s. Under the circumstance of an isotropic stress field, the inclined crack propagates along its original path. However, in an anisotrpopic stress field, the inclined crack should grow to become perpendicular to the minimum stress direction. These phenomena are well captured in our phase field model (see Figure 62).

4.6.2 Pressurized crack interaction in a homogeneous medium

Next, a more complicated case for the interaction between existing fractures are simulated. This section is to present the capability of the phase field model to observe numerically fracture inclination because of the regional stress influence. A fixed boundary condition is applied to the outer boundary of the domain, and the fluid

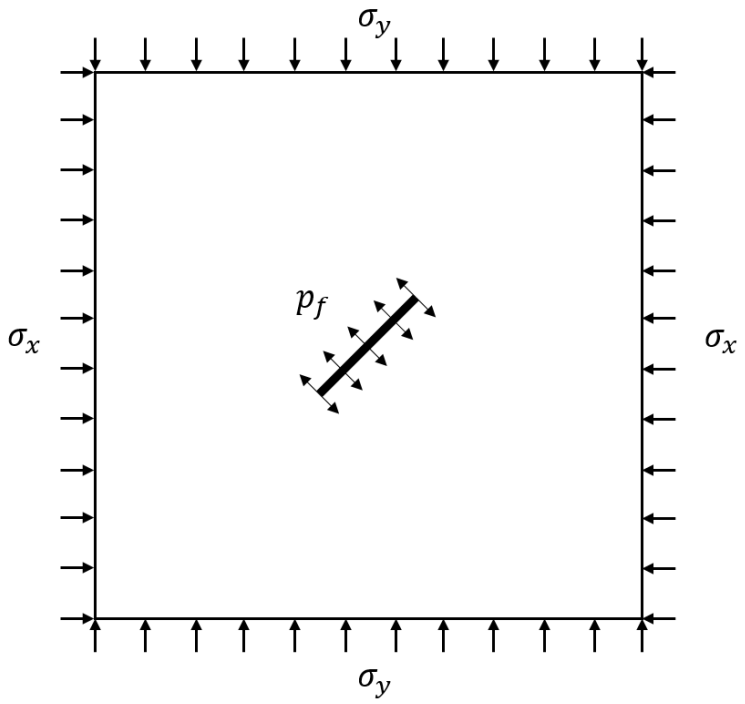

Figure 59: Model setup for a pressurized inclined crack. The domain Ω is $(0, 1)^2$ m. The fracture is inclined with an angle 45° at the center of the domain, and the location of the crack is from the point (0.45, 0.45) to the point (0.55, 0.55). The Lamé parameters are λ =28 MPa and μ = 18.7 MPa. The critical energy release rate G_c = 100 J/m^2. The mobility $M = 1.25 \times 10^{-8}$ $1/Pa \cdot s$ for isotropic and $M = 10^{-7}$ $1/Pa \cdot s$ for anisotropic case. The mobility is chosen to find a stable growth of the fracture.

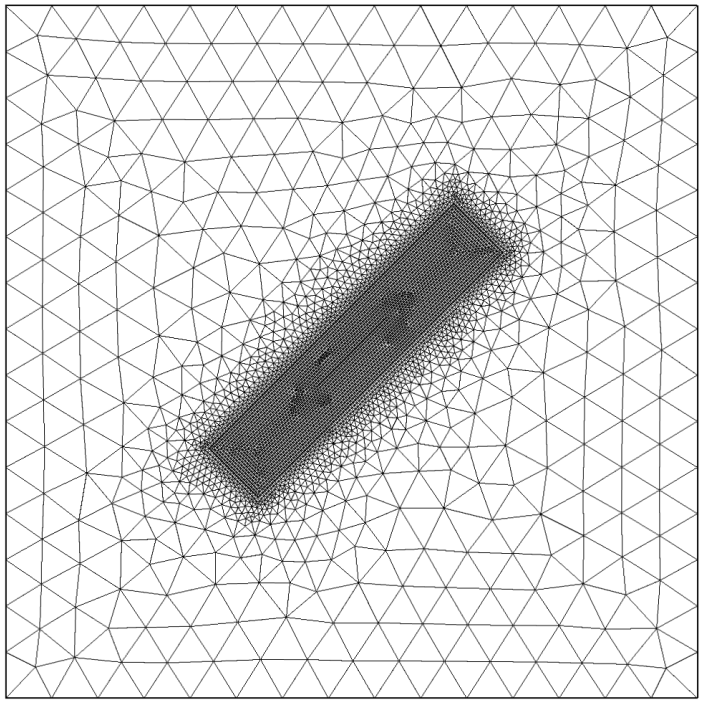

Figure 60: Mesh setup for a pressurized inclined crack. The mesh size at critical zone is 0.005 m (isotropic $1/10\,l_c$ and anisotropic $1/4\,l_c$), and the total mesh of 8636 elements.

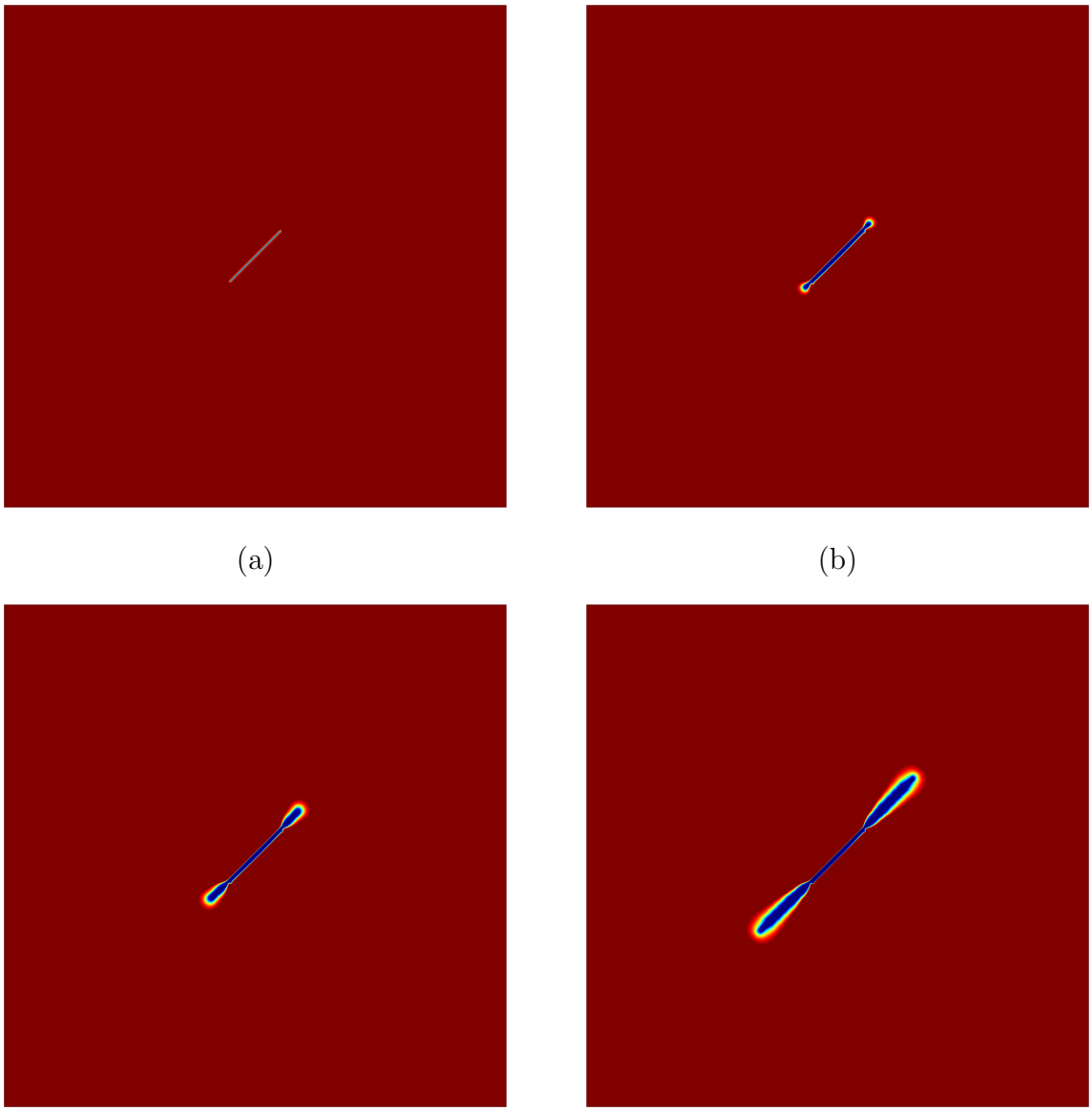

(a) (b)

(c) (d)

Figure 61: Evolution of the phase field under isotropic far field stress ($\sigma_x = \sigma_y = 1.5$ MPa). (a) 10 s, (b) 70 s, (c) 80 s, and (d) 90 s. The color scheme is the same as Figure 41.

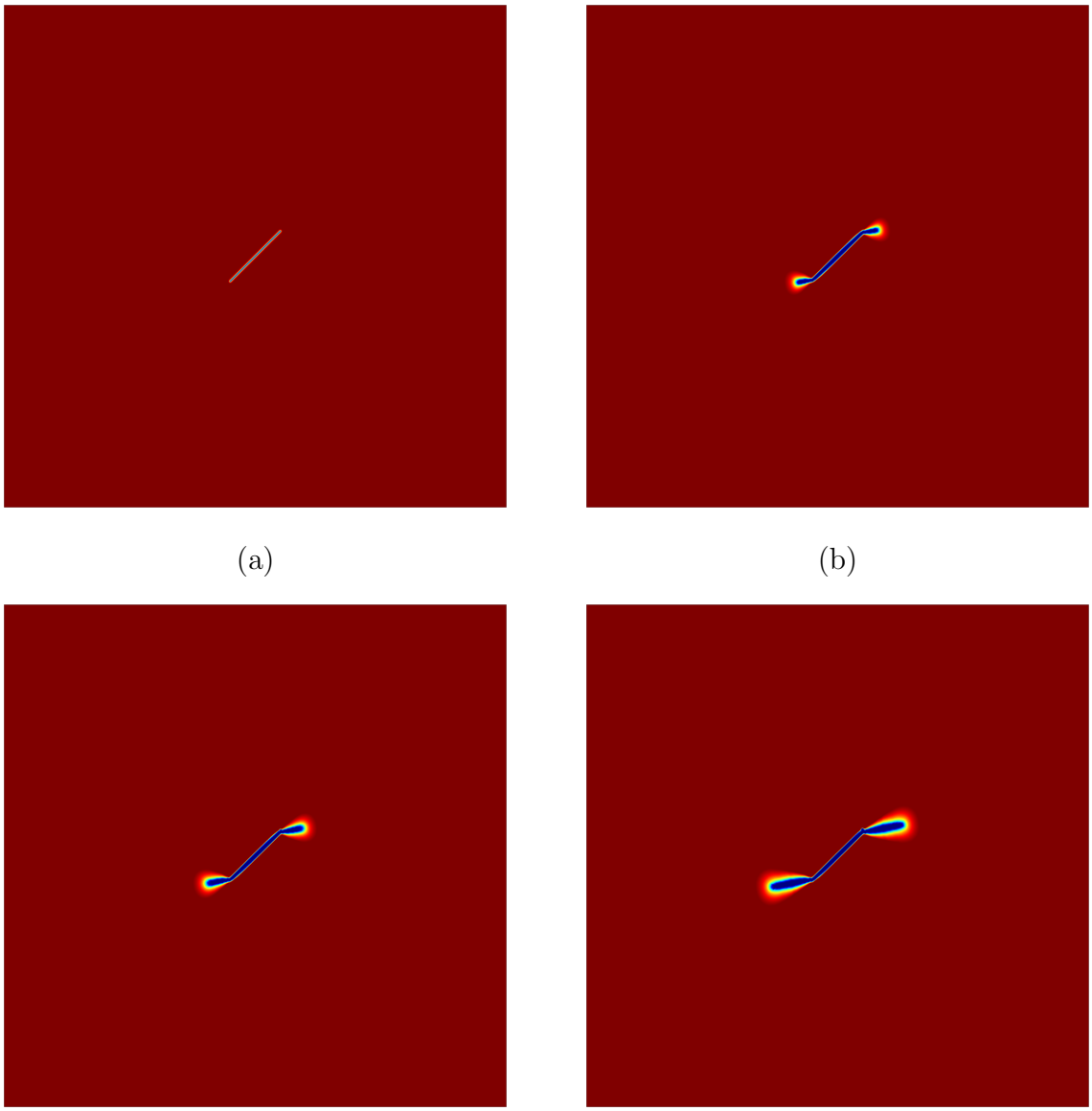

(a) (b)

(c) (d)

Figure 62: Evolution of the phase field under anisotropic far field stress ($\sigma_y = 1.5$ MPa, $\sigma_x = 0$ MPa). (a) 10 s, (b) 30 s, (c) 32 s, and (d) 35 s.

pressure gradually increases at a rate of 0.1 MPa/s inside cracks. From Figure 63, it can be recognized that the inclined fracture grows without any interference from the vertical fracture. On the contrary, the vertical fracture is influenced by the compression stress field created by the inclined fracture, and grows perpendicular to the line of the inclined fracture, which is observed in Figure 62. The interfered growth of the vertical fracture provides the evidence of the capability of the phase field method to model and depict the interaction between existing fractures.

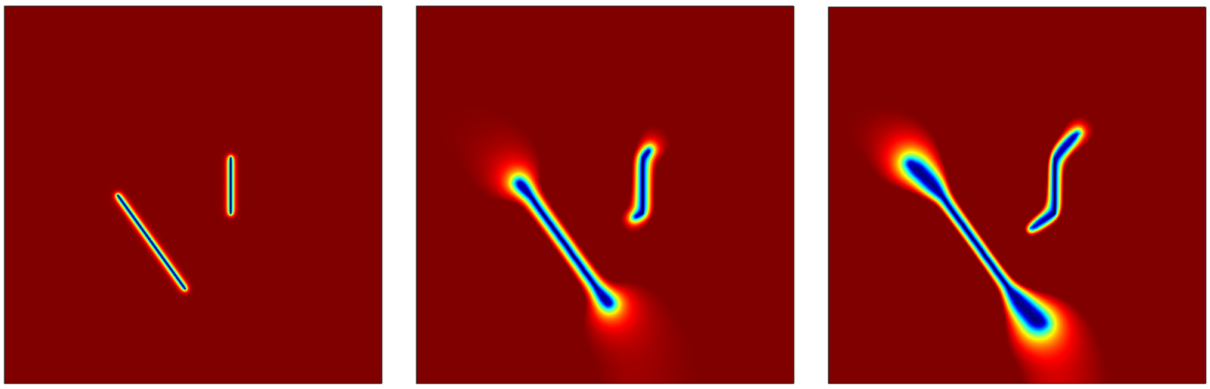

(a) (b) (c)

Figure 63: Pressurized fracture interaction in a homogeneous medium. The domain Ω is $(0,\ 4)^2$ m, and the fractures are pre-installed that the geometry of the inclined fracture is from (0.3, 0.5) to (0.48, 0.25), and the vertical fracture is from (0.6, 0.45) to (0.6, 0.3) . Fixed boundary condition is applied on the outer boundary of the model for displacement boundary. The solid parameters are E =1 Pa, $\nu = 0.2$, and residual stiffness ratio is again set to 0. The critical energy release rate $G_c = 1$ J/m^2, and the mobility $M = 10^{-3}$ 1/Pa $\cdot$ s. $l_c = 0.04$ m and the mesh size is $h_{max} = 1/4\, l_c$. It is further refined at the fracture with $h_{max} = 1/20\, l_c$. The fluid injection causes the raise of the fluid pressure inside the fractures with a rate of 0.1 MPa/s.

4.6.3 Pressurized crack interaction in a heterogeneous medium

This example follows the model setup by Mikelić [75] to present the capability of phase field method to model fracture initiation, joining, branching, and forming complex fracture patterns. The domain Ω is $(0,\ 4)^2$ m, with the first crack horizontally installed from point (1.8, 2) to (2.2, 2) and the second crack vertically installed from point (2.6, 1.8) to (2.6, 2.2). A non-displacement boundary condition is applied to the

outer boundary. The characteristic length scale $l_c = 0.04$ m, and the mesh size is $1/2\, l_c$ near the crack to regularize, and set to l_c for the sake of computational effort with a total of 27186 elements. The heterogeneity is introduced through the random distribution of the elastic properties. The distribution of the elastic properties are shown in Figure 64. The pressure inside fracture increases with a rate of 0.1 Pa/s. The mobility M is set to 10^{-4} 1/Pa $\cdot$ s to stabilize the propagation process. The corresponding pattern created are shown in Figure 65, a complex fracture pattern is generated.

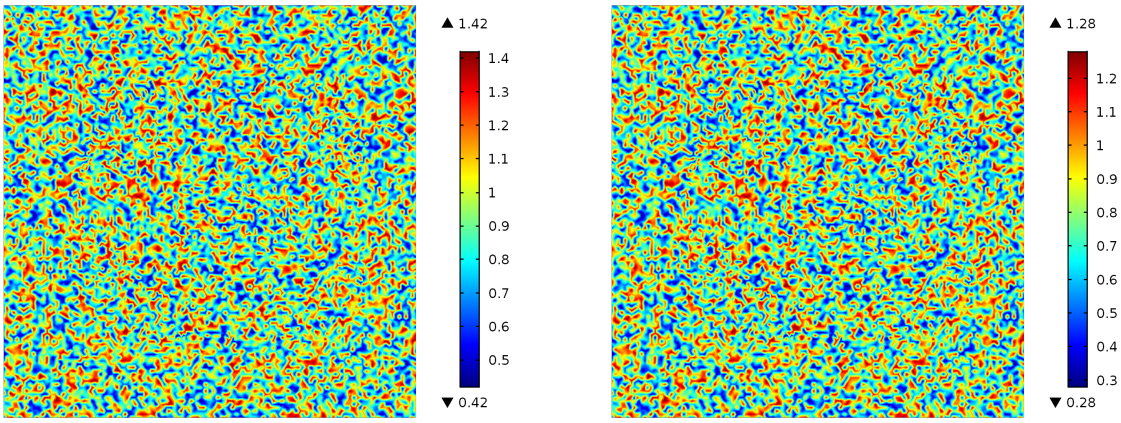

(a) (b)

Figure 64: The uniform distribution of the Lamé parameters. (a) $\lambda \in (0.42, 1.42)$ Pa, (b) $\mu \in (0.28, 1.28)$ Pa.

4.6.4 Crack initiation due to flaws at the wellbore

This section will try to combine the phase field with our experimental results to see if any common feature can be reproduced to explore the mechanism of the initiation of the fracture in granular materials. Indeed, this would be phenomenological approach to capture the similarity. At first, a well bore instability caused by the flaw on the wall of the bore hole. The instability is introduced by setting the phase field randomly distributed ($\phi \in (0, 1)$) along the surface of the well bore. The boundary condition at the outer boundary is set to fixed boundary condition for displacement field and zero-flux condition for phase field. The well bore and the corresponding mesh for the

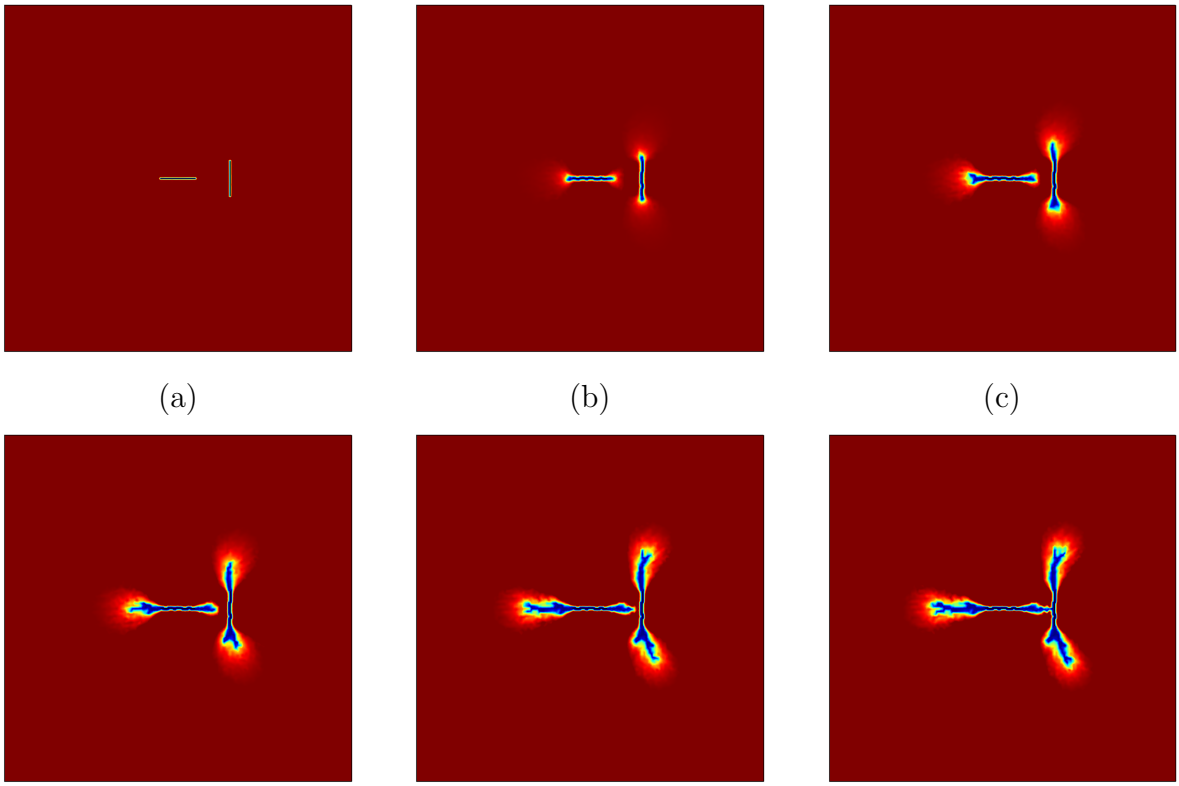

Figure 65: Pressurized crack interaction in a heterogeneous medium. The frames are taken at (a) 10 s, (b) 80 s, (c) 100 s, (d) 110 s, (e) 120 s, and (f) 123 s. The larger value of the pressure compared to the literature [75] is because of the viscous regularization delays the fracture propagation (see Section 4.5 for the discussion). The horizontal fracture grows dominantly in horizontal direction. The vertical fracture grows initially vertically, then later tilts right-wise because of the compression from the stress field of the horizontal fracture.

model are provided in Figure 66. The domain Ω is $(0,\,1)^2\ m$, with a bore hole at the center. The characteristic length scale $l_c = 0.01\ m$. The mesh size is $1/2\,l_c$ for the inner zone, l_c for the intermediate zone, and $2l_c$ for the remaining. The Lamé parameters are given as $\lambda = 28\ Pa$, and $\mu = 18.7\ Pa$. G_c is set to a relatively small value of 1 J/m^2. The pressure is applied the surface of the well bore with a rate of increment $\dot{p} = 10^5\ Pa/s$. The mobility M is set to $10^{-4}\ 1/Pa \cdot s$ to stabilize the propagation process. Again fluid pressure will be set to equal on every nodal values in domain, and $\alpha = 0$, which enables wherever fracture occurs (ϕ falls to 0), the fluid pressure will further open up the fracture.

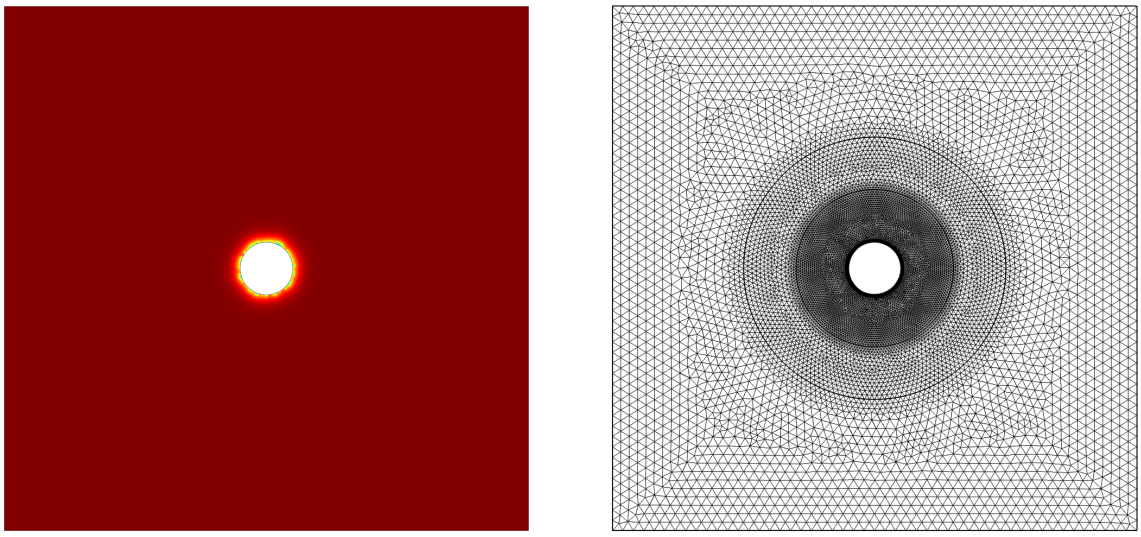

Figure 66: Model setup for crack initiation due to flaws at the wellbore.

Before the simulation of the hydraulic fracturing process near well bore, the stress distribution is first verified with the elastic solution (see Figure 67):

$$\sigma_{rr} = \frac{r_i^2 P_i - r_o^2 P_o}{r_o^2 - r_i^2} - \frac{r_i^2 r_o^2 (P_i - P_o)}{r^2 (r_o^2 - r_i^2)}, \tag{56}$$

$$\sigma_{\theta\theta} = \frac{r_i^2 P_i - r_o^2 P_o}{r_o^2 - r_i^2} + \frac{r_i^2 r_o^2 (P_i - P_o)}{r^2 (r_o^2 - r_i^2)}. \tag{57}$$

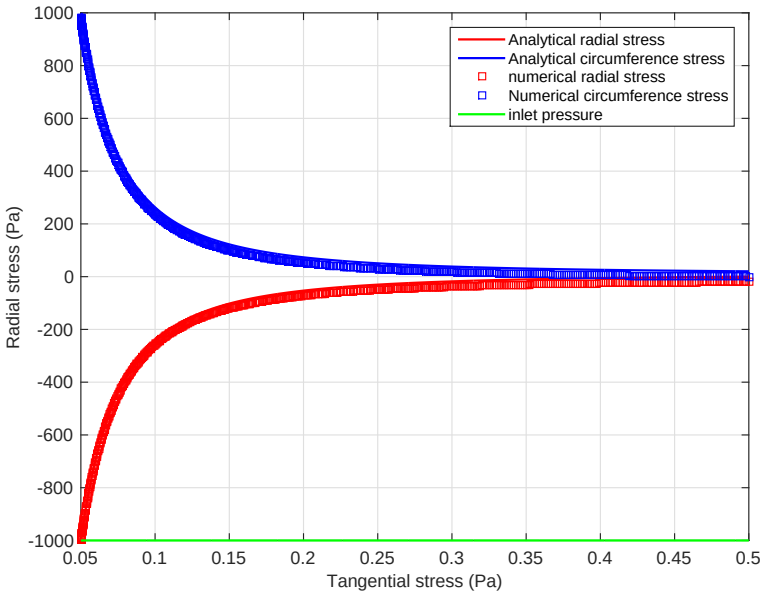

Figure 67: Stress distribution of a pressurized cylinder. The inner wall pressurized by the fluid pressure with a magnitude of 1000 Pa in compression and the outside radial stress is set to 0. Tensile stress is positive as our sign convention.

The instability of the phase field at well bore will lead to random initiation of the crack (Figure 68.b). As the pressure rises, the selection of the propagation direction is based on local energy minimization, and the dominant fractures will be formed and continue to grow (Figure 68.c and d). Initially it will be growing several micro cracks, but as the pressurization continues, some dominant fractures will continue to grow and shield will happen to the other fractures.

Phase field model shows the similarity observed in both DEM simulation of injection into cohesionless material [96] and experiments with soft rocks [9], and indicates the initial straight radial crack may have caused by the tensile failure, i.e., toughness governed. Another example of the capability of our current model is that without setting initial instability from phase field, we will study the case of the fracture initiation in a heterogeneous material. The model setup and the properties are depicted in Figure 69. The fluid pressure increment is set to $\Delta p = \dot{p}\Delta t$, with a rate $\dot{p} = 10^5$ pa/s. The heterogeneity causes the fracture initiation and later on the propagation near well bore (see Figure 69), which provides the indication of the potential of the

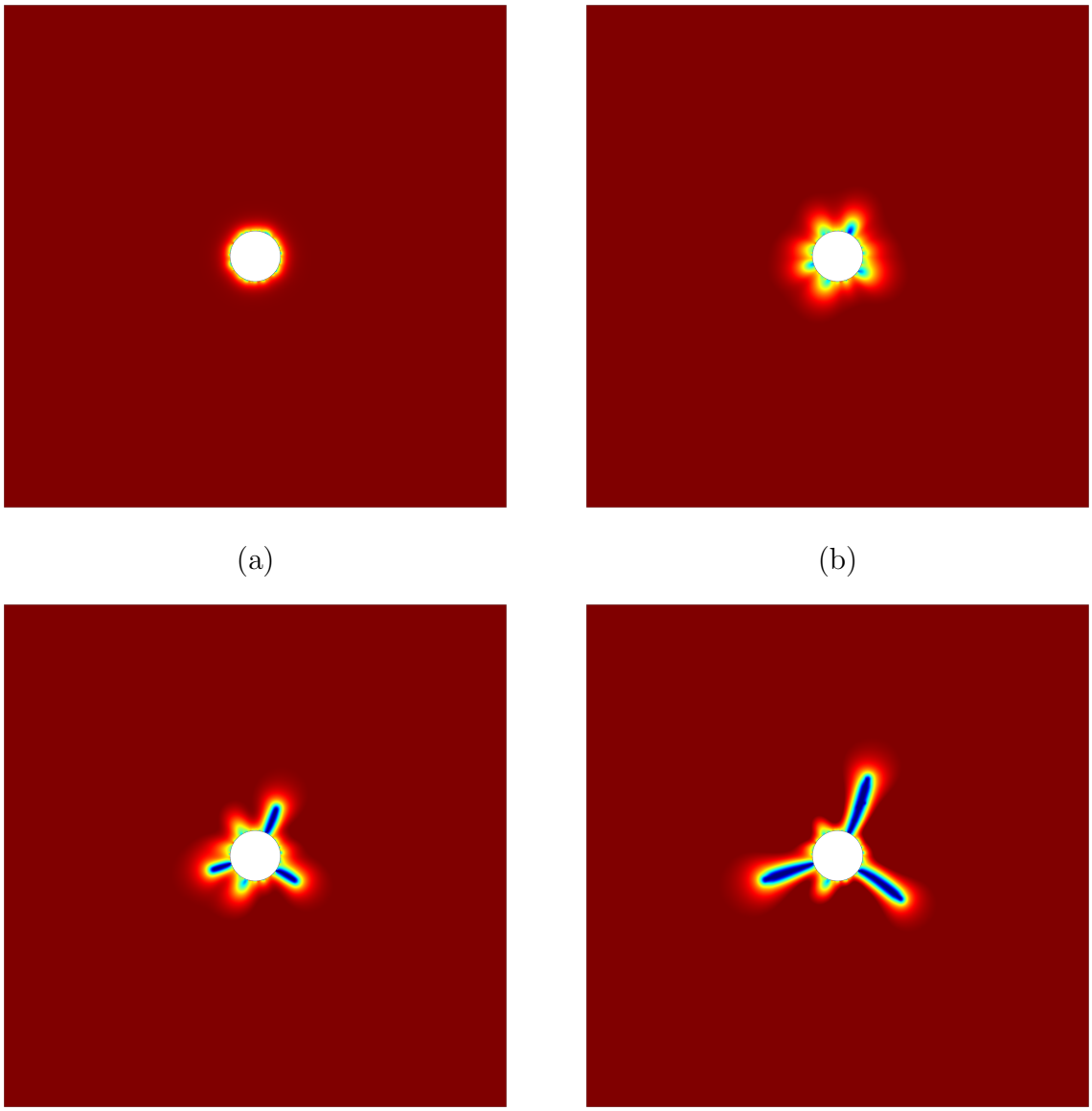

(a) (b)

(c) (d)

Figure 68: Crack growth from a wellbore (homogeneous media). The snapshots are taken at (a) 10 s, (b) 38 s, (c) 39 s, and (d) 40 s.

phase field method to model the fracturing process without any pre-installed crack or geometric treatment.

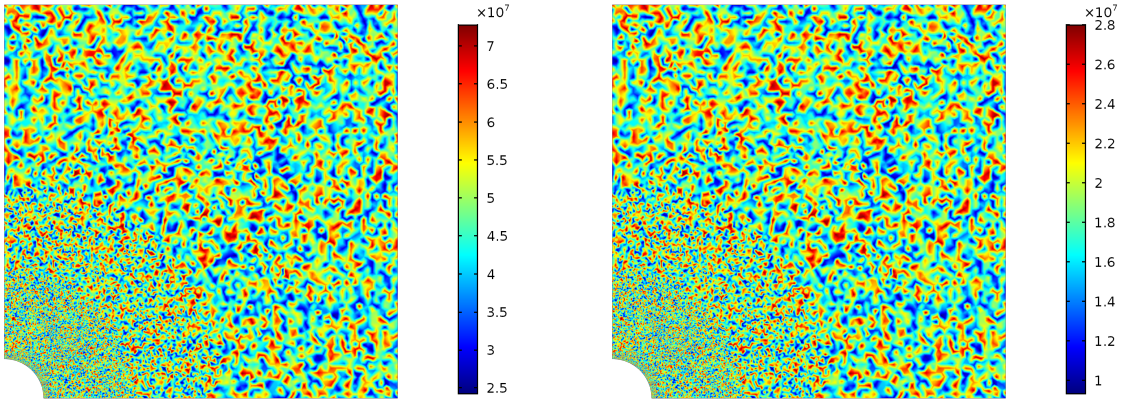

(a) (b)

Figure 69: Heterogeneous domain $\Omega \in (0,\ 1)^2\ m$. The well bore radius is 0.1 m. (a) The distribution of Lamé constant λ (average value of 48.5 MPa), (b) the distribution of Lamé constant μ (average value of 18.7 MPa), and (c) the distribution of the mesh; The characteristic length l_c is given as 0.01 m. The critical energy release rate is set to $G_c = 2.7\ kJ/m^2$, and the mobility $M = 10^{-7}\ 1/P \cdot s$. Initially phase field $\phi = 1$ for the entire domain indicating solid phase only. Fixed boundary condition on the top and right side of the domain for displacement field. Symmetric boundary condition on the bottom and the left, and applied fluid pressure boundary on the surface of the well bore.

Crack growth from a wellbore under anisotropic stress condition is shown in Figure 73 and Figure 74. The material properties are the same with the previous model shown in Figure 69, and the boundary conditions are depicted in 72. For the isotropic stress condition, the formation of the fracture is similar to the case shown in Figure 71, i.e., crack initiates randomly at the wellbore, and then a dominant crack propagates radially. In the case of anisotropic stress, the primary fracture perpendicular to the maximum principal stress direction, which illustrates that near well bore the fracture growth is governed by the stress condition.

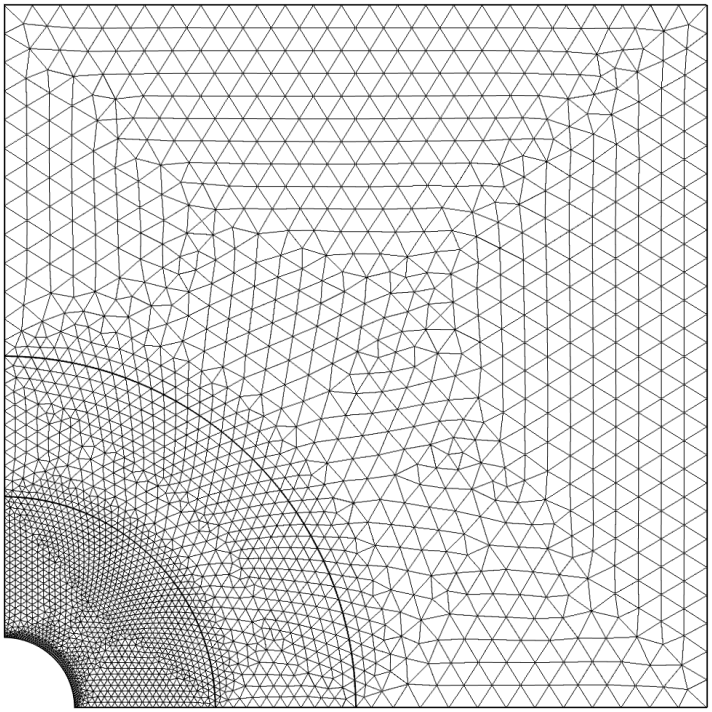

Figure 70: Mesh setup for the heterogeneous model. From inner to the outer mesh, the maximum size changes 1/10 l_c (at wall), 1/2 l_c, l_c, and $2l_c$. The mesh density determines the randomness of the distribution of the Lamé parameters.

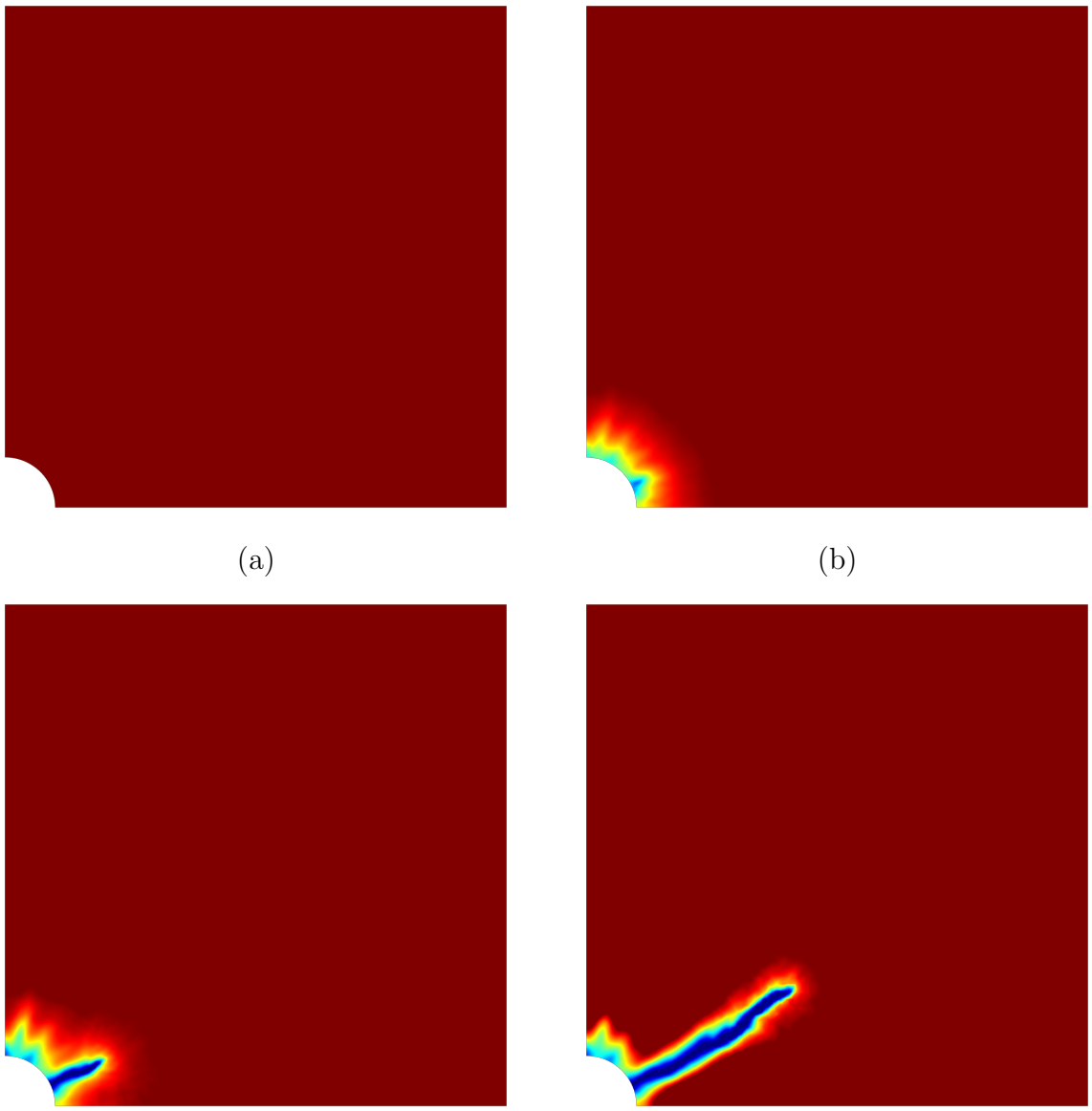

(a) (b)

(c) (d)

Figure 71: Crack growth from a wellbore (heterogeneous media). The color scheme is same as in Figure 41. The snapshots are at time (a) 0, (b) 41, (c) 45, and (d) 51 s.

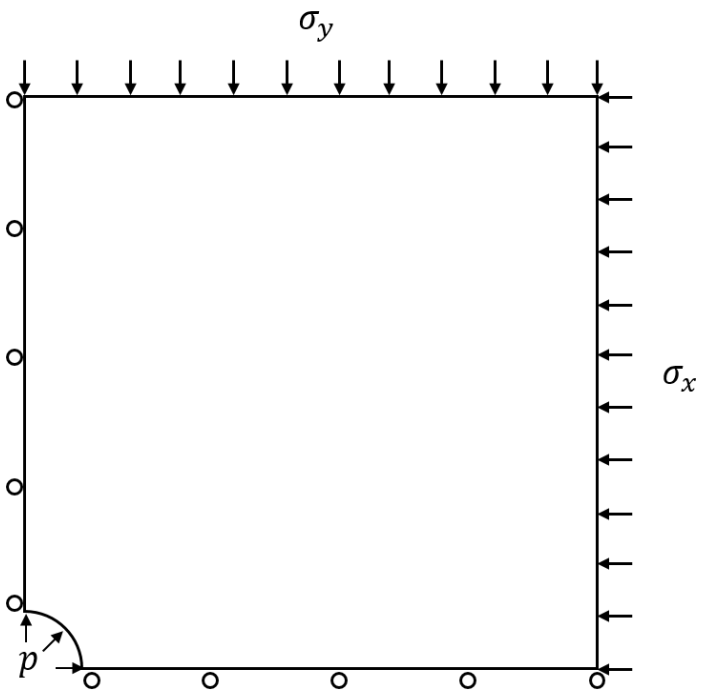

Figure 72: Model setup for crack growth from a wellbore under anisotropic stress condition (heterogeneous media).

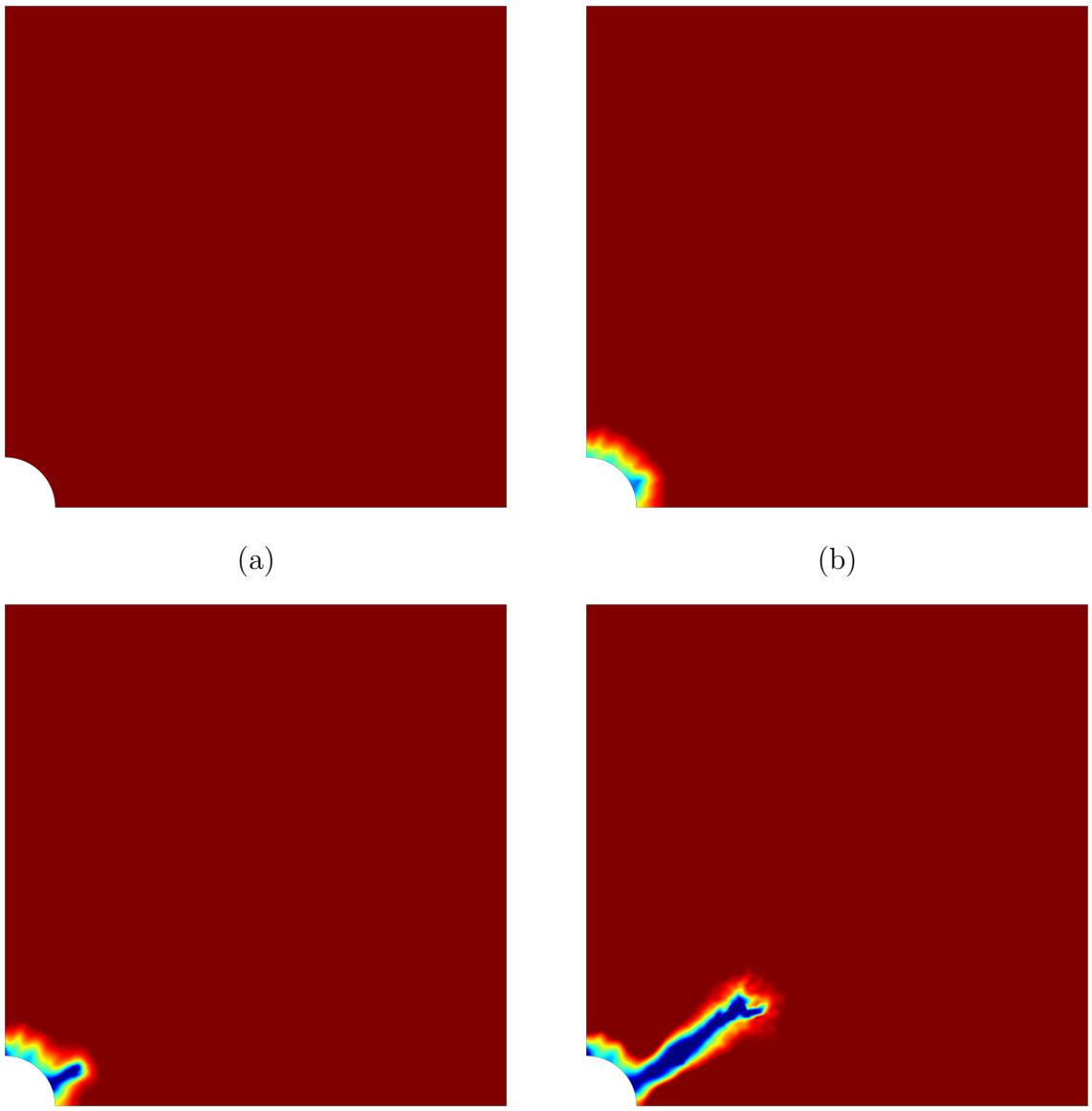

(a) (b)

(c) (d)

Figure 73: Isotropic stress condition ($\sigma_x = \sigma_y = 0.5\ MPa$). Snapshots are taken at time (a) 0, (b) 53 (initiation of the crack), (c) 56 (fracture propagation), and (d) 62 s.

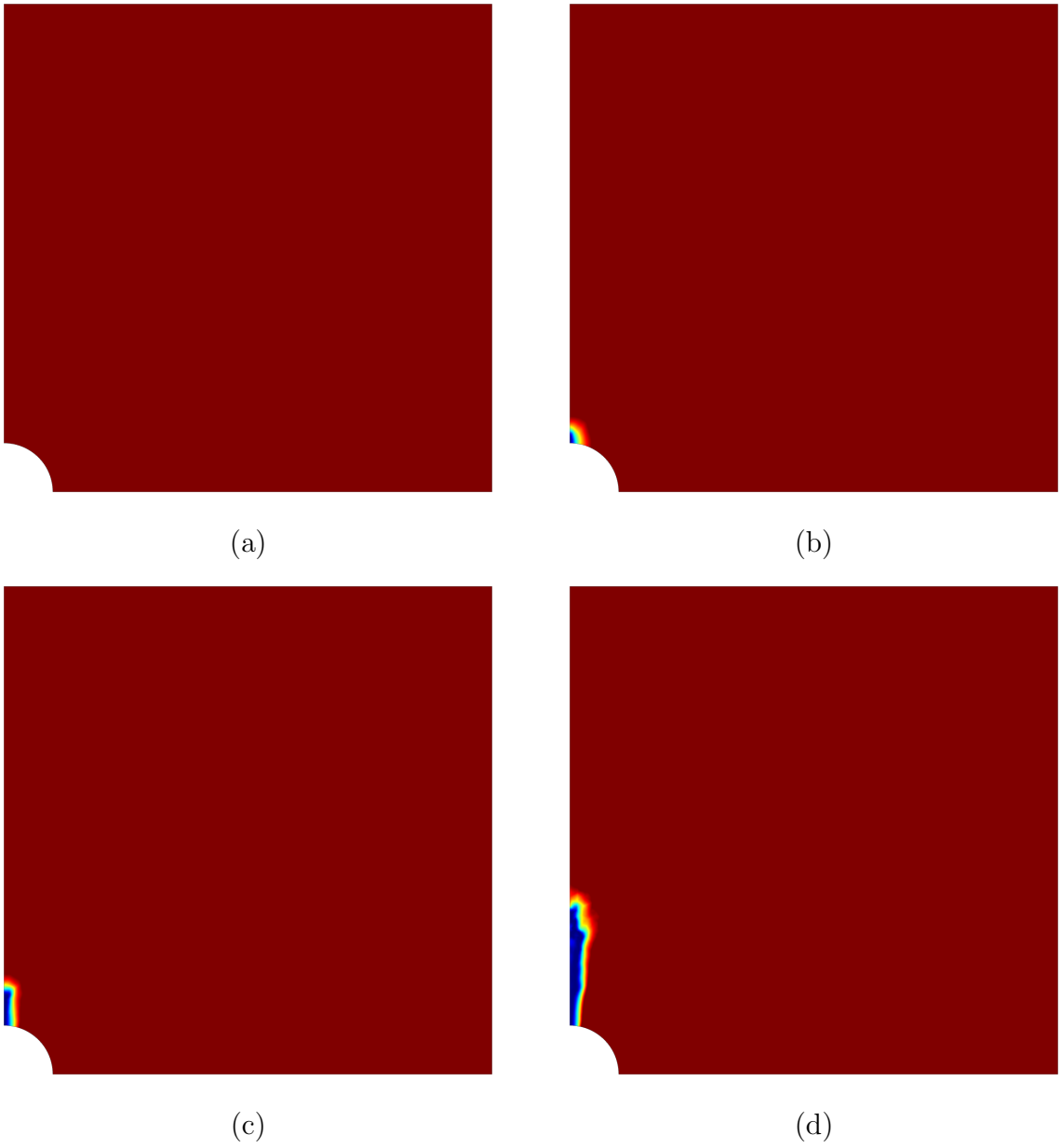

Figure 74: Anisotropic stress condition ($\sigma_x = 0.5$ MPa and $\sigma_y = 1.5$ MPa). Snapshots are taken at time (a) 0, (b) 42 (initiation of the crack), (c) 46 (fracture propagation), and (d) 52 s.

4.7 Conclusions

As a continuum approach, the pressurized fracture propagation process is simulated with phase field method. A hybrid phase field method is developed by adopting viscous phase evolution and the hybrid scheme for constitutive law to reduce the computational cost and enhance the stability. The model is constructed and implemented into the equation based solver COMSOL Multiphysics®. The model is verified with the classic Griffith's theory and Sneddon's solution. Furthermore, it is shown in this work that the constructed model is capable of modeling complicated fracture growth such as merging and tip splitting. Crack growth from a wellbore is modeled under various stress conditions.

CHAPTER V

ACID CLEANING TO RECOVER THE FRACTURE CONDUCTIVITY

5.1 Introduction

Weak formations like sandstone generally contain at least 2 to 15 % of fines by weight [78]. These fines may migrate to the fracture during production and cause clogging inside the fracture, which can significantly drop the permeability of the fracture and reduce the production. Figure 75 shows a schematic drawing of such process. Formation fines may also cause formation damage by forming filter cakes near fracture [69]. Acid cleaning has been used to recover the fracture conductivity by injecting an acid solution to dissolve fines. If the fines react with the acid and are dissolved, porosity in the fracture increases. The process is a multi-physics problem which involves fluid flow in porous media, chemical reaction, and chemical transport. Depending on the mineral of the formation and fines, different acid can be used. For example, for carbonate formations, hydrogen chloride acid (HCl) is chosen as the reactive agent, and hydrofluoric acid (HF) should be chosen to remove aluminosilicates (like Kaolinite) in rock pores. The mineral of the primary fine damage to the fracture is regarded as Kaolinite in this study, so HF is assumed as the reactive agent.

Matrix acidizing in porous media could result in not only permeability change of the porous media but also the possibility of forming a wormhole network [19, 20, 50]. However, a uniform dissolution would be more beneficial to recover the conductivity of an existing fracture, meanwhile not dissolving formation fines which causes waste of acid and thereby inefficient treatment. Reactive transport in pore scale has been studied substantially by researchers both numerically and experimentally.

Kang et. al [49] found that when Damköhler number $Da = k_r L/D_d$ is sufficiently small, it will be the process of uniform dissolution at pore scale, i.e., the reaction takes place everywhere that acid passes through. With a given surface reaction rate, L chosen as a typical pore scale $\sqrt{k} = o(10^{-4})$ m, k_r the surface reaction rate between HF and Kaolinite 6×10^{-10} $\frac{kmol(clay)}{m^2(clay)\cdot s\cdot[kmol/m^3(HF)]}$, and typical diffusion coefficient of hydrofluoric acid as 10^{-9} m^2/s, Damköhler number is calculated in a order of $o(10^{-2})$. If L is taken as pore scale, which is much smaller than fracture half width, the Damköhler is even smaller. This indicates a uniform dissolution would be the main reaction mechanism, and the growth wormhole channels is not the likely reaction scenario.

In this work, the acid cleaning process is modeled using hydro-chemically coupled scheme implemented in the equation based solver COMSOL Multiphysics® to investigate the effects of injection rate, dimensionless fracture conductivity, and reaction rate on the effectiveness of acid cleaning.

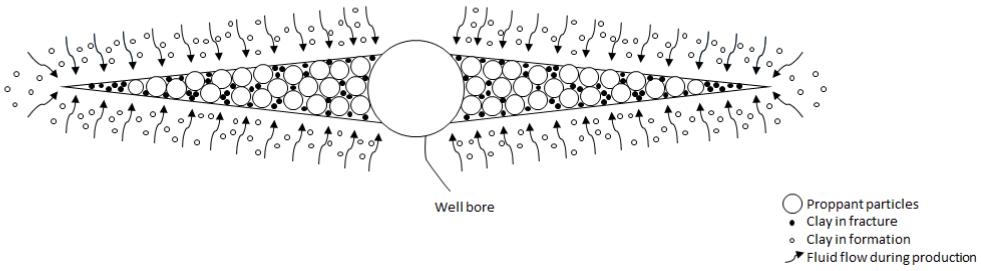

Figure 75: Damaged fracture because of the fine migration during production

5.2 Mathematical model

5.2.1 Fluid flow

For isothermal compressible fluid flow through rigid porous media, the fluid transport equations in the porous media can be written as,

$$\frac{\partial(n\,\rho)}{\partial t} + \nabla \cdot (\rho \mathbf{u}) = \dot{S}, \tag{58}$$

$$\mathbf{u} = -\frac{k}{\mu}\nabla p, \tag{59}$$

where ρ represents the density of the fluid, t the time, n_p the porosity, $\mathbf{u}$ the fluid Darcy velocity, and mass source term $\dot{S}$. The permeability k is defined as scalar implying isotropic condition of the media. After uniform dissolution, the same assumption still holds. Since our model is in isothermal condition, fluid viscosity is assumed to be constant through out the simulation, and thus Eq. (58) can be modified in terms of the independent variable p for the isothermal condition. For slightly compressible liquid, fluid density is related to pressure p through [7],

$$c_f = \frac{1}{\rho}\frac{d\rho}{dp}, \tag{60}$$

where c_f is the fluid isothermal compressibility which is independent of pressure. Therefore the density of the fluid can be given as,

$$\rho = \rho_0 exp[c_f(p - p_0)], \tag{61}$$

where ρ_0 is the reference density at a reference pressure p_0, which is set to be the same as atmospheric pressure. For the case of incompressible fluid, where $c_f = 0$, Eq. (61) gives a constant density ρ_0.

5.2.2 Chemcial transport

Chemical transport is modeled as a process of diluted species transport in porous media. General form of the transport equation can be written as,

$$\frac{\partial(n\,c_i)}{\partial t} + \mathbf{u}\cdot\nabla c_i = \nabla \cdot (D_i \nabla c_i) + R_i, \tag{62}$$

where c_i is the solute concentration of a chemical specie i, D_i the dispersion coefficient of specie i, which is assumed to be constant under isotropic homogeneous dispersion process, and R_i the reaction rate, which is the only source term in the system. The first term keeps the derivative of the porosity in order to capture the reality that the porosity inside the fracture is a time dependent variable. Second term in the equation is the advection term, which enables the convective chemical transportation with the fluid flow. Two diluted species are defined as c_{HF} and c_{tracer}, which are the concentration of HF acid and the concentration of fluid tracer that captures the fluid front and pattern. The transport equations for these two species become

$$\frac{\partial(n\, c_{HF})}{\partial t} + \mathbf{u}\cdot\nabla c_{HF} = \nabla\cdot(D_{HF}\nabla c_{HF}) + R_{HF}, \tag{63}$$

$$\frac{\partial(n\, c_{tracer})}{\partial t} + \mathbf{u}\cdot\nabla c_{tracer} = \nabla\cdot(D_{tracer}\nabla c_{tracer}). \tag{64}$$

5.2.3 Clay dissolution reaction

The main mineral of sandstone is quartz, so that the injection of HF acid indeed results in dissolution of quartz component. However, the HF acid reacts mainly with the associated minerals such as clays, feldspars and micas rather than the quartz [19], so for simplicity, it is a reasonable to assume that reaction happens only on the clay surface with a surface reaction rate k_r. further model We can convert it into bulk clay concentration reaction rate k_b (1/s/[kg moles HF/m^3]/[kg moles clay/m^3]) as

$$k_b = k_r a M_{clay}, \tag{65}$$

where a is the reactive surface area of the clay, and M_{clay} (g/mol) is the molar mass of the clay mineral, which here is 258.156 g/mol for the Kaolinte. Dissolution of a single mineral into the solution is then modeled as linear reaction kinetics (first order reaction) with a bulk reaction rate k_b:

$$\frac{\partial c_{clay}}{\partial t} = -k_b c_{HF} c_{clay}, \tag{66}$$

where c_{clay} is the converted bulk concentration of the clay mineral, and its initial value is determined by

$$c_{clay}|_{t=0} = \frac{w_{clay}}{M_{clay}} = \frac{n_f \xi G_c \rho_w}{M_{clay}}. \tag{67}$$

In the above equation, w_{clay} (kg/m^3) is the unit mass of clay per unit volume, n_{f0} is the original fracture before the fine damage, ξ is the initial clay volume portion which assumes at 30% of occupation in the pore space, G_c is the specific gravity of Kaolinite, and ρ_w is the density of water. With given values, the initial clay bulk concentration would be 1,208.6 mol/m^3. Eq. (66) would calculate a new bulk concentration, then use Eq. (67) to calculate the remaining clay bulk density, therefore the new porosity in the fracture would be obtained as

$$n_f = n_{f0} - \frac{w_{clay}}{G_c \rho_w}. \tag{68}$$

In the reservoir, we estimate the formation in this study contains 5% Kaolinite by weight according to general mineral composition of sandstone [78] and pick the overall specific gravity of the remaining mineral G_s as 2.65. The initial reservoir porosity n_{r0} is then 0.13. The real time reservoir porosity n_r is defined as,

$$n_r = 1 - \frac{w_{clay}}{G_c \rho_w} - \frac{(1-\zeta)\rho_s}{G_s \rho_w}. \tag{69}$$

The permeability update in both fracture and reservoir follows the Blake-Kozeny equation

$$k = \frac{D_{50}^2}{150} \frac{n^3}{(1-n)^2}. \tag{70}$$

The reaction of Kaolin with hydrofluoric acid (HF) can be given as [86],

$$Al_2Si_2O_5(OH)_4 + 24F^- + 14H_3O^+ \rightarrow 2Al_2F_6^{3-} + 2S_iF_6^{2-} + 23H_2O, \tag{71}$$

$$Al_2Si_2O_5(OH)_4 + 12F^- + 6H_3O^+ \rightarrow 2Al_2F_6^{3-} + 2S_iO_2 : H_2O + 9H_2O, \tag{72}$$

where Eq. (71) is for the reactions at low temperature (around 20 °C), and Eq. (72) is for the reactions at high temperature (around 50 °C). The selection of the equation

depends on the local status of reservoir temperature. We regard the reaction under high temperature case, i.e., Eq. (72) governs. Therefore, when 1 $kmol$ clay mineral reacts, it needs 12 $kmol$ of hydrofluoric acid, i.e., the bulk reaction rate of hydrofluoric acid R_{HF} is 12 times the bulk reaction rate of the clay R_{clay}. On the other hand, for the sake of low temperature, same amount of clay demands more HF consumption. However, we have found this matters little on the treatment of the fracture since the reaction takes place faster than convective transport.

5.3 Model setup

5.3.1 Simulation parameters

In order to reduce the computational effort, the symmetry condition utilized. 1/4 part of the wellbore and surrounding reservoir are selected for the study (see Figure 76). The reservoir domain size is set to be large enough to avoid any boundary effect with a length of L as 60 m and width W as 30 m. For simplicity, the fracture is regarded as a thin layer in a rectangle shape. It should be noted that, indeed the fracture width is much smaller in reality, e.g. 0.5 mm. The smaller fracture width, the smaller fracture conductivity, so that formation flow becomes bilinear, which indicates one dimensional flow inside the fracture. Therefore, the effect of b_f is negligible. On the other hand fluid flow behavior is determined by the dimensionless fracture conductivity $(k_f b_f)_D$ (see Eq. (73)). The actual reservoir may have lower permeability say 10^{-16} m^2, which compensates the change in fracture width so that the fracture conductivity is equal, and thereby the formation flow is identical. From the computational aspect, the real width of the fracture encounters a extremely fine mesh comparing to the size of simulation domain. Increasing the fracture width significantly reduces the computational cost. At the bottom leftmost corner is the inlet where the wellbore locates. Fluid is entering into the system perpendicular to the inlet surface. Symmetric boundary condition at the bottom and leftmost boundaries. A constant

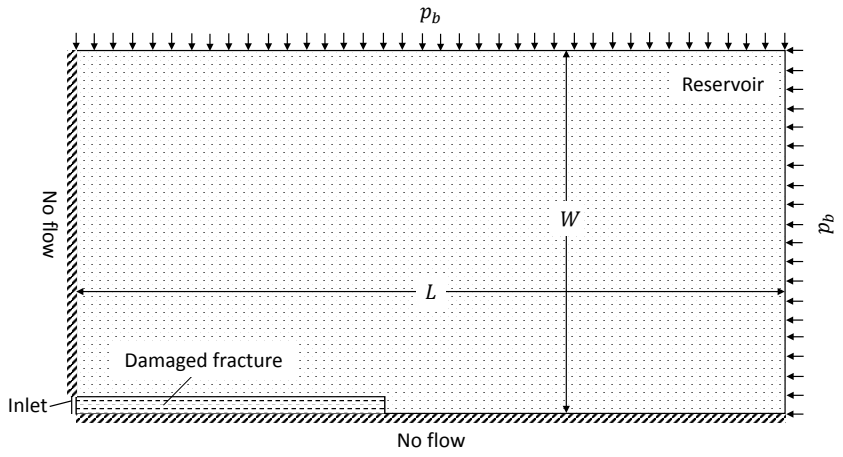

Figure 76: Simulation domain for the acid cleaning process. Plot is not drawn to the scale in order to enlarge the fracture to show the model setup.

pressure boundary set at the top and right end of the reservoir domain with back-pressure p_b. Same symmetric non-flow condition at the bottom and left boundary, and open boundary at the remaining boundaries. A detailed model parameters are provided in the Table 10.

The fracture is modeled with two different types of proppants: Ottawa F110 and Ottawa 20/40 sand. Ottawa F110 has a porosity range from 0.38 to 0.45 with a permeability about 1 *Darcy* at low confinement. Ottawa 20/40 proppant has a porosity range from 0.40 to 0.44 according to US Silica White$^{\text{TM}}$. By considering the in situ stress, we assume a value of initial porosity of the fracture $n_{f0} = 0.4$ for both cases, which is close to the minimum value. The long-term permeability of the 20/40 proppant is measured and shown dependency on the reservoir stress which ranges from 10 *Darcy* to 202 *Darcy* according to the product data sheet. We pick

Table 10: Modeling parameters for reservoir flow with Ottawa F110 proppant.

Parameters	Value	Description
G_s	2.65	Specific gravity of reservoir rock
G_c	2.60	Specific gravity of Kaolinite
k_{res0}	$10^{-15}\ m^2$ (1 mD)	Initial reservoir permeability
ζ	5 %	Reservoir fine content weight percentage
k_{f0}	$10^{-12}\ m^2$ (1 $Darcy$)	Initial fracture permeability before damage
k_{f1}	$2.38 \times 10^{-13}\ m^2$	Fracture permeability after damage
n_{f0}	0.4	Initial fracture porosity
ξ	30 %	Initial volume portion of fine in fracture
n_{res}	0.13	Initial reservoir porosity
ρ_w	$10^3\ kg/m^3$	Density of water
ρ_s	$2.3 \times 10^3\ kg/m^3$	Density of reservoir mass
μ	$10^{-3}\ Pa \cdot s$ (1 cp)	Fluid viscosity
β	$5 \times 10^{-10}\ 1/Pa$	Fluid compressibility
Q	34.98 m^3/day (220 STB/day)	Injection rate of chemical solution
H	14.94 m (49 ft)	Formation thickness
b_f	0.15 m (0.5 ft)	Fracture width
x_f	27.04 m (88.7 ft)	Fracture half length

202 *Darcy* under 2,000 *psi* closing pressure as our model input for the case of Ottawa 20/40.

Assuming the reservoir in the model is initially fully saturated with oil. Fluid properties such as density, viscosity, and compressibility are all assumed to be same for both chemical solution and original reservoir fluid, which are set as the same value as water. The viscosity of water at 25 °C is 0.89 cp that is close to a typical reservoir oil viscosity of 0.8 cp [17]. Both liquid state of oil and solution is slightly compressible, therefore, the small compressiblity assumption used in the model may meet our first order estimation purpose. Also for simplicity, the density of the water and oil is set to be equal, although the density of oil in reality should be slightly less than water.

Dimensionless fracture permeability $(k_f b_f)_D$ is defined as [32, 17],

$$(k_f b_f)_D = \frac{k_f b_f}{k_{res} x_f}. \tag{73}$$

With parameters in Table 10, we can estimate dimensionless hydraulic conductivity. If the proppant used is Ottawa F110 sand, the current fractured well has a $(k_f b_f)_D$ of 5.64 before fine damage and 1.34 after the damage. For the case of Ottawa 20/40, $(k_f b_f)_D$ before damage would be 1127, and after damage would become 269. According to previous research [17], $(k_f b_f)_D \sim o(1)$ indicates the fluid flow regime will be bilinear flow, and $(k_f b_f) \sim o(10^2)$ indicates the fluid regime is formation linear. We see these patterns in Figure 83 and Figure 84. Figure 77 shows the highest permeability achievable from the acid dissolution, i.e., when the clay content is reacted and dissolved completely in HF acid solution, the optimum permeability of the fracture can be recovered up to its initial value k_{f0}. Figure 77 provides the permeability recovery after dissolution. It can be found that the fracture permeability drop can be nearly 80% after fine damage.

Chemical transport input parameters are provided in Table 11. Inside the fracture, it is a mixed process of advection, dispersion, and reaction. The coupled problem is

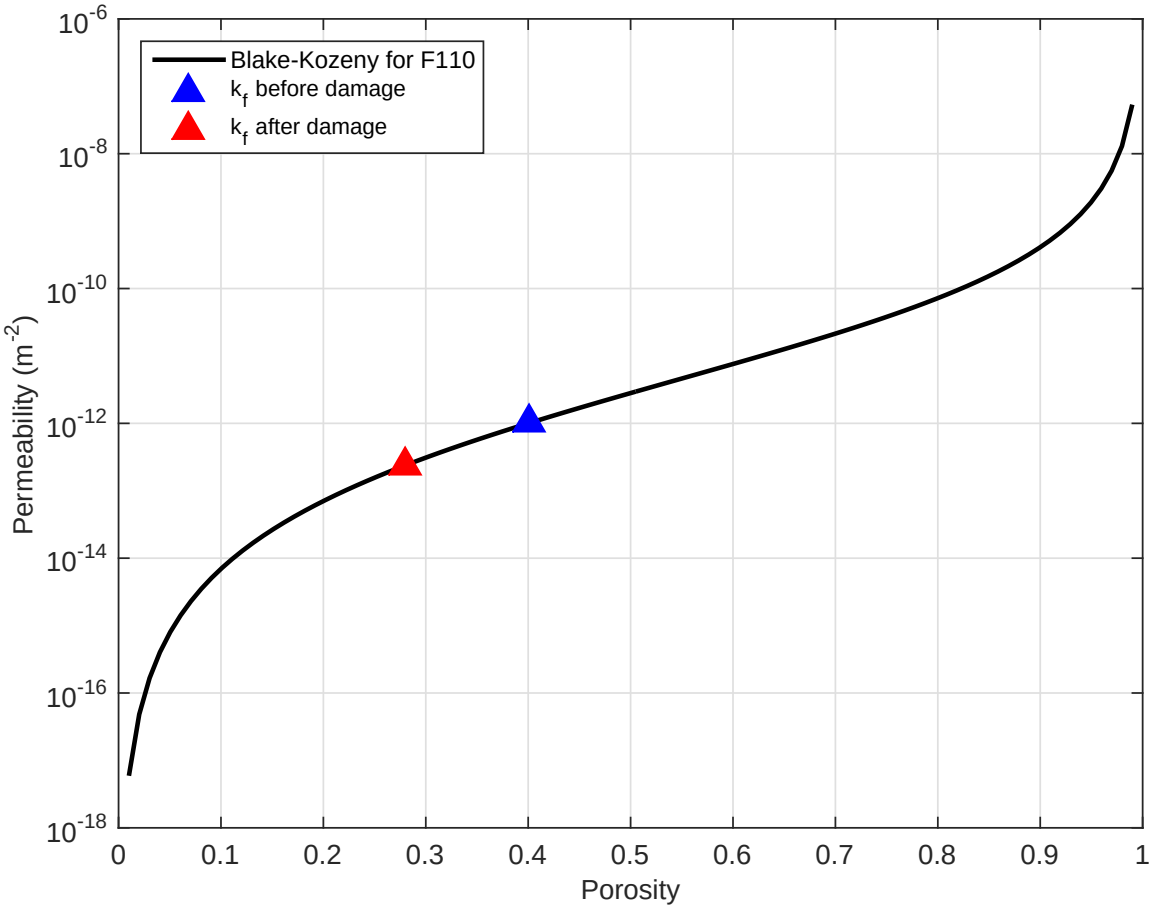

Figure 77: Permeability and porosity relation from Blake-Kozeny equation for Ottawa F110.

Table 11: Chemical transport properties

Parameters	Value	Description
c_{HF0}	1.61 $kmol/m^3$	Inlet HF acid concentration
c_{check}	1.61 $kmol/m^3$	Inlet fluid tracer concentration
k_r	6×10^{-10} $\frac{kmol(clay)}{m^2(clay)\cdot s\cdot[kmol/m^3(HF)]}$	Coefficient of surface reaction rate
a	8×10^3 m^2/kg	Reactive surface area for Kaolin particles
D_{HF}	10^{-6} m^2/s	Dispersion coefficient of HF acid
D_{tracer}	10^{-6} m^2/s	Dispersion coefficient of artificial concentration

characterized by element the Damköhler number $Da : Da = |s|h/|u|$ and the element Peclet number Pe: $Pe = |u|h/D$, where u is Darcy velocity, and h is the element size. s is rate coefficient determined as $s = k_r a M_{clay} c_{HF}$ for clay reaction. It is production if $s > 0$, and adsorption if $s < 0$. The numerical stability can be analyzed with Galerkin least-squares method [18] that is the product of Da and Pe should meet the criteria that

$$DaPe = \frac{|s|h^2}{D} \leq 1. \tag{74}$$

A laboratory measured diffusion coefficient of hydrofluoric acid is 10^{-9} m^2/s [77]. If this value is used, it would require millions of mesh to achieve the numerical stability. In addition, in large scale, the dispersion which includes mechanical dispersion and the diffusion is the main mixing mechanism and normally it is greater than the process of diffusion. Therefore, artificial dispersivity coefficient can be defined (see Table 11) to significantly reduce the size of required mesh.

5.3.2 Mesh options

In consideration of the required minimum element size defined by $DaPe$ and for the sake of the computational efficiency, a combination mesh can be generated as shown in Figure 78. Because of the large velocity inside the fracture, fine grid mesh is applied to in the fracture domain to satisfy the numerical stability and capture the

coupling process. In reservoir domain, no reaction appears far from the fracture, so the coupled transport equation would reduce to advection dispersion equation. For such a problem, the minimum element size is governed by the element Peclet number Pe as defined above. Darcy velocity will be smaller in the reservoir than inlet fluid flux and even smaller further from the inlet. Therefore, the required minimum mesh size is no longer needed to be substantially small. Between these two regime, a free triangular mesh can be applied to smooth transition from fine meshed zone to coarse. Each simulation consists of a total of 62,540 elements in the domain.

5.3.3 Numerical algorithm

The coupling algorithm is shown in Figure 79. When the simulation starts, the continuity equation (Eq. (58)) is solved to provide overall pressure field of the domain. Next, with the given pressure field, Darcy's law is applied to give the velocity field. Advection dispersion equation (Eq. (63)) acquires this velocity field and updates the concentration field. The clay concentration field updates the porosity (Eq. (68)), and with Blake-Kozeny equation (Eq. (70)) the permeability is calculated for the next time step.

5.4 Simulation results and discussions

5.4.1 Pressure field

Dimensionless wellbore pressure can be defined as [17],

$$p_{wD} = \frac{k_{res} H (p_w - p_0)}{\alpha_o Q B \mu}, \tag{75}$$

where α_o is unit conversion constant, and B is formation volume factor. For the case of oil, $\alpha_o = 1,842$, and we assume the formation volume factor B is 1.2. The wellbore history for all simulations are provided in Figure 80. Under same fracture conductivity, peak p_{wD} decreases as the injection rate increases. It also suggests that

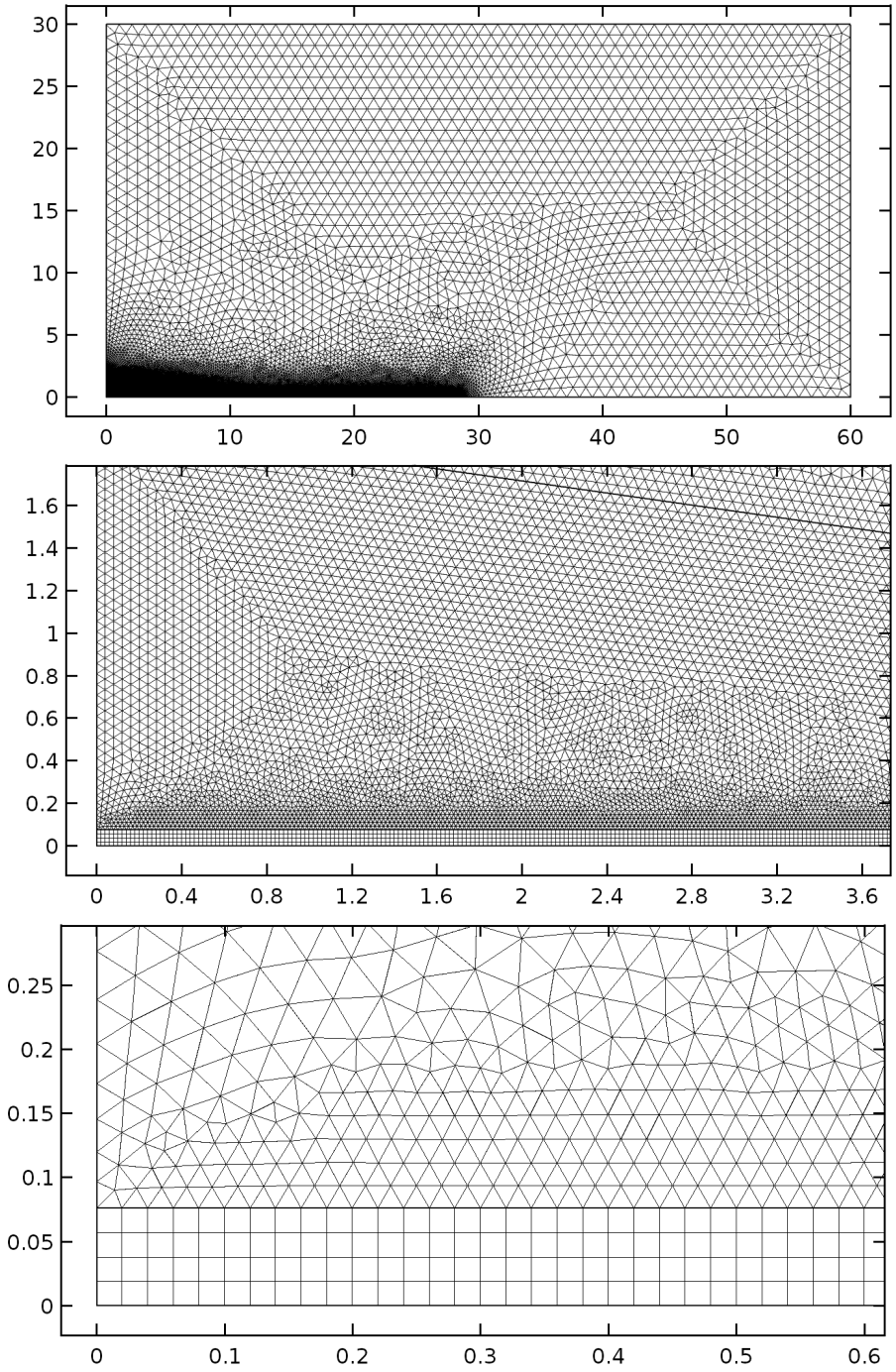

Figure 78: Combination of mapped mesh and free triangular mesh

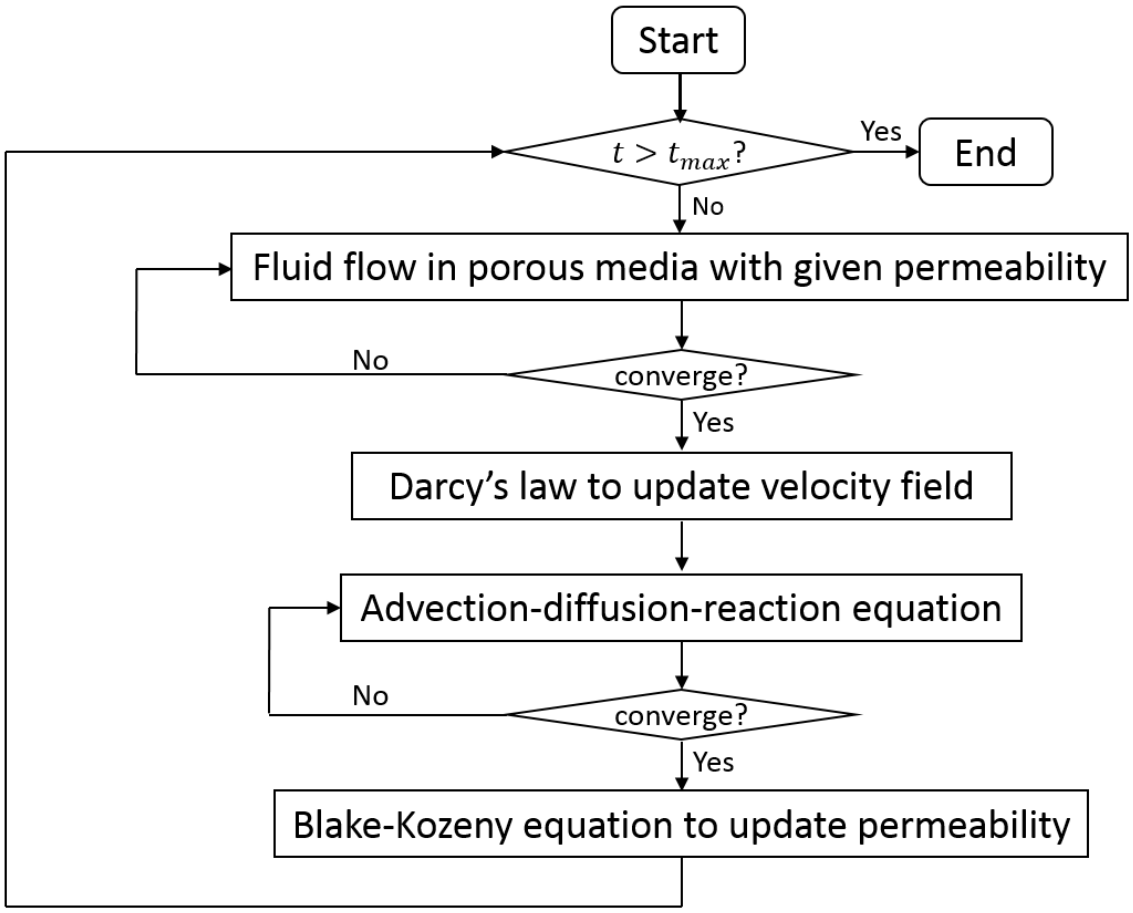

Figure 79: Numerical algorithm for coupled problem of advection-dispersion-reaction

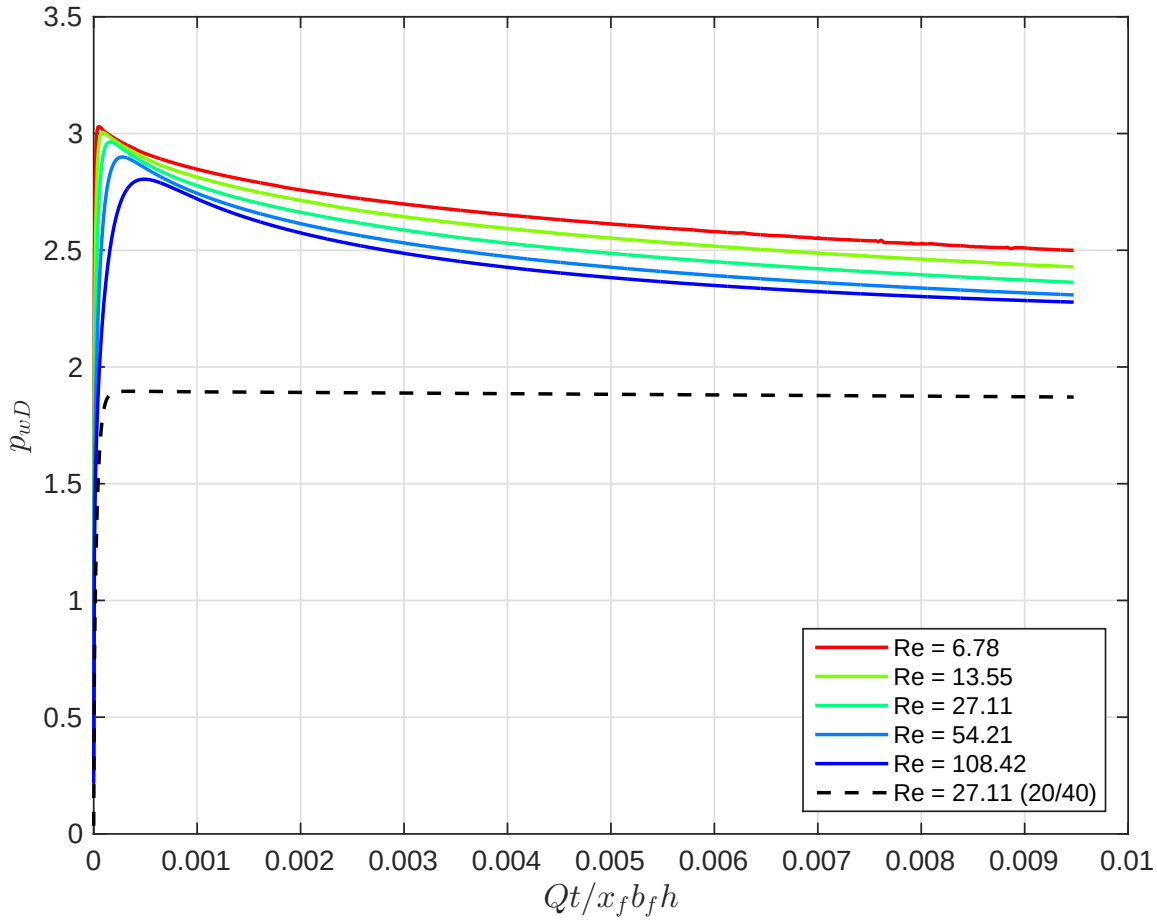

Figure 80: Dimensionless wellbore pressure with normalized injection volume

bilinear type of flow regime at early stage, when the wellbore pressure builds up to drive the fluid into the fracture until senses the fracture tip (Figure 82). In post peak zone, the fluid will gradually flow linearly into the formation (Figure 83), which also implies p_{wD}will gradually become flat and reach a constant plateau. The higher injection rates have less p_{wD}, which illustrates the fracture conductivity is increasing faster than slower injection rates. For the case of high fracture conductivity (Ottawa 20/40 proppant), no wellbore pressure peak is observed. Instead, it reaches a constant plateau when it is maximum, and the fluid flows perpendicular to fracture surface, which proves the flow is formation linear (Figure 84). Overall, because of the higher fracture conductivity in Ottawa 20/40, the required p_{wD} is about 40% less than Ottawa F110 fracture.

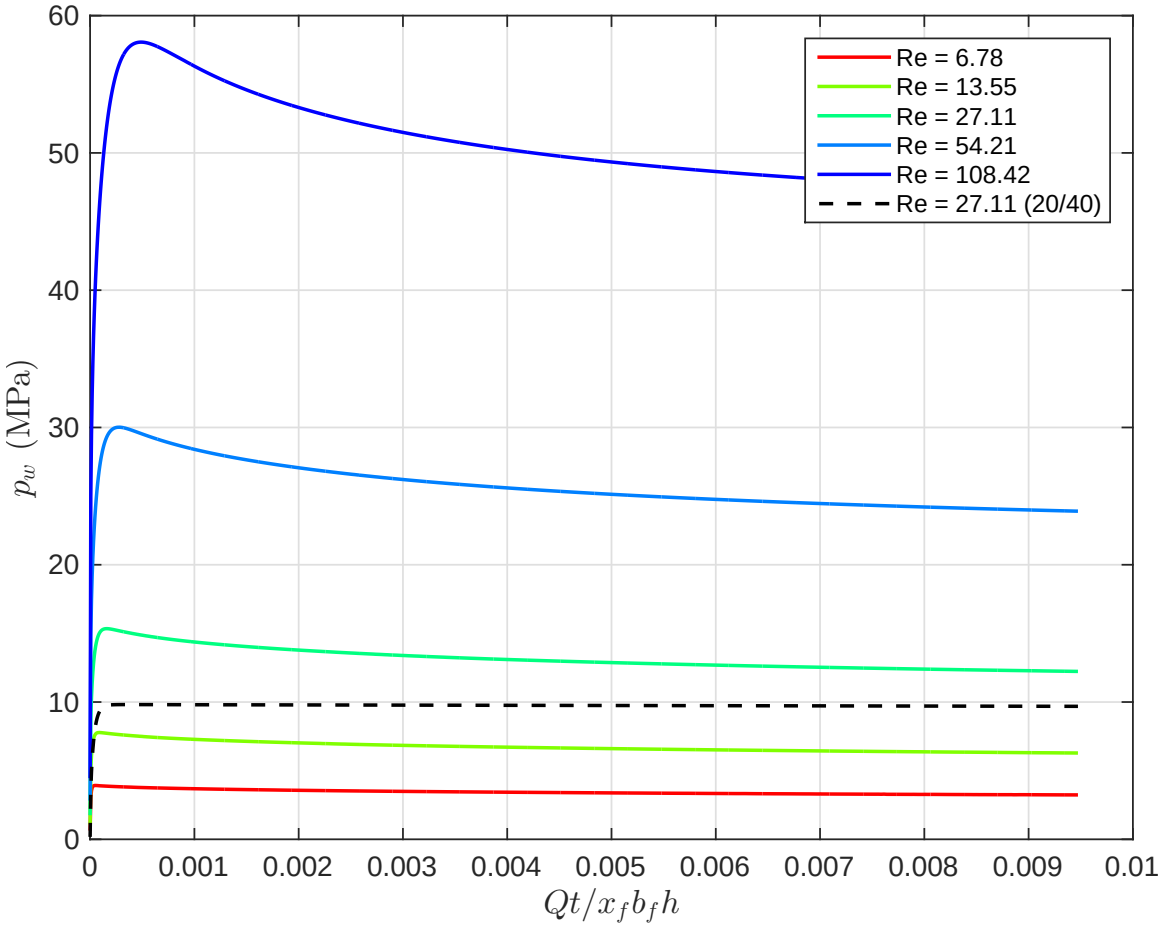

Figure 81: Wellbore pressure with normalized injection volume

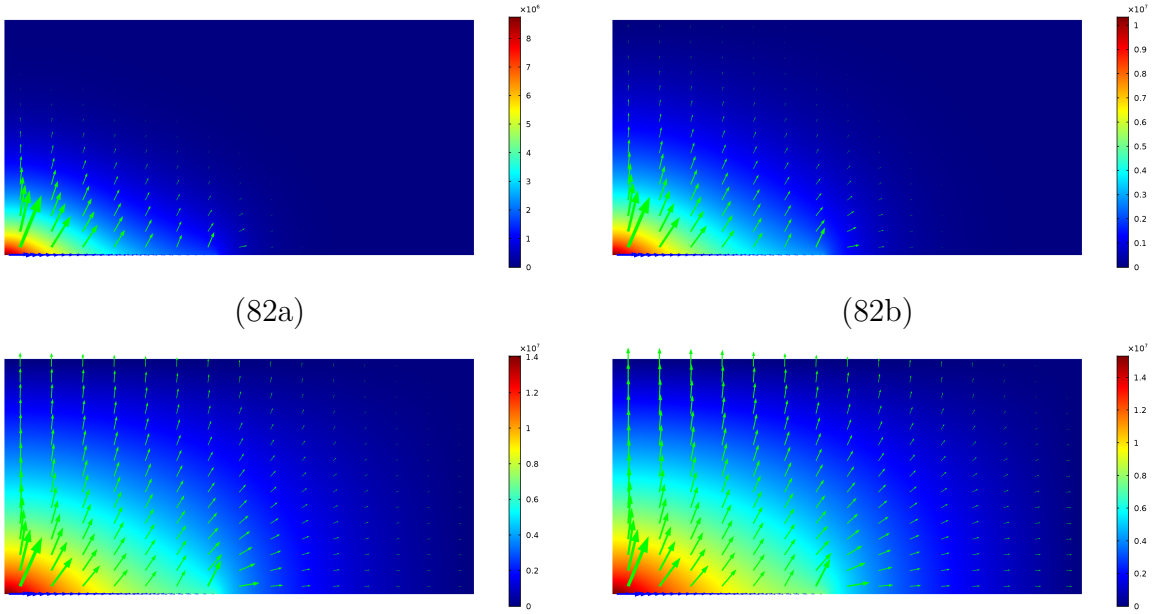

(82a) (82b)

(82c) (82d)

Figure 82: Pressure distribution before the peak wellbore pressure (Ottawa F110). From (a1) to (d1), figures are after an injection time of 1 *hour*, 2 *hour*, 4 *hour*, and 30 *hour*. The color bar units is in *Pa*. Pressure distribution indicating the bilinear flow regime. Green arrows depict flow pattern inside the reservoir, and blue arrows represent the flow direction inside the fracture. The Arrows are scaled to a ratio of 350:1 (green:blue), which suggests the fluid Darcy velocity in reservoir is much smaller comparing to the one in fracture. Large pressure gradient near wellbore enables fluid transport along the fracture and into the formation until the wellbore pressure senses the end of the fracture tip.

5.4.2 Concentration profiles

We find the reaction takes place faster than fluid convection effort. This can be seen the concentration profile inside the fracture (Figure 85) that the reaction front locates at a clear interface between clay and HF acid. The reaction interface lags behind fluid front, and the propagation rate of the fluid front is faster than the reaction front. One dimensional model is built to study the effect of reaction coefficient (Figure 86). It shows HF acid could not penetrate this interface unless the reaction coefficient reduces

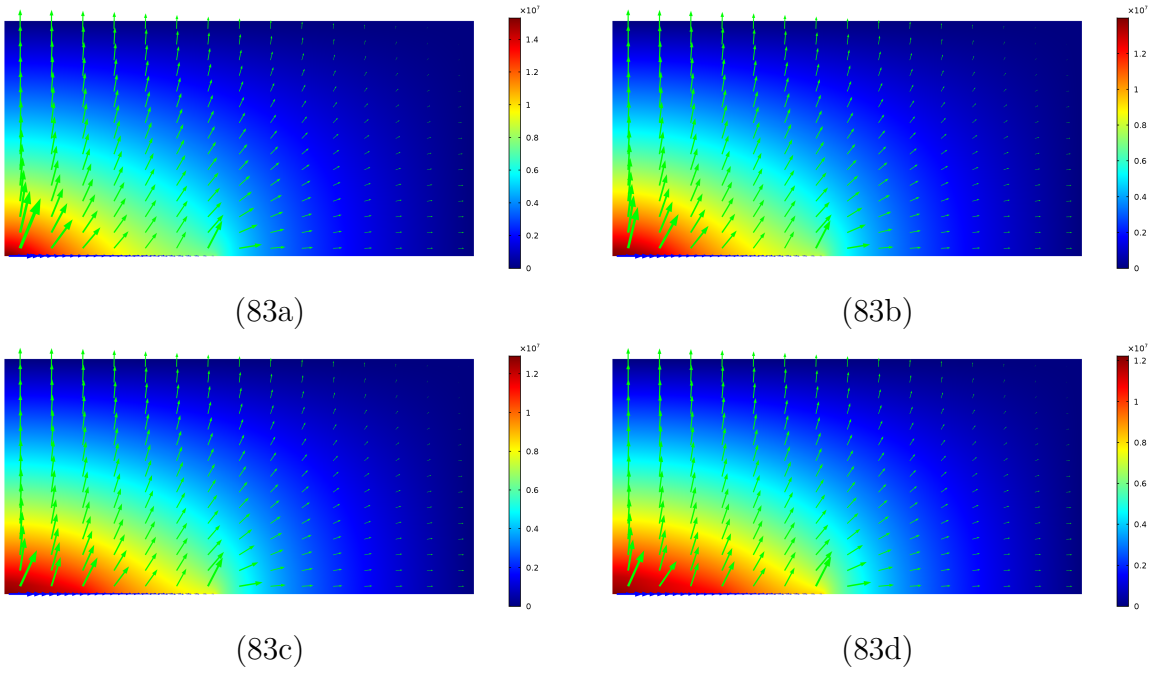

(83a) (83b)

(83c) (83d)

Figure 83: Pressure distribution after the peak wellbore pressure. Scaling and units are the same as Figure 82. From a to d, figures are after an injection time of 30 *hour*, 10 *days*, 20 *days*, and 40 *days*. After peak, the wellbore pressure has sensed the fracture tip and so that the pressure gradients reduces, and pressure distribution develops vertically to the fracture into the formation, and thereby the fluid velocity gradually towards perpendicular to the fracture indicating formation linear regime. Late time near wellbore flow is radial because of the increased reservoir permeability from reaction.

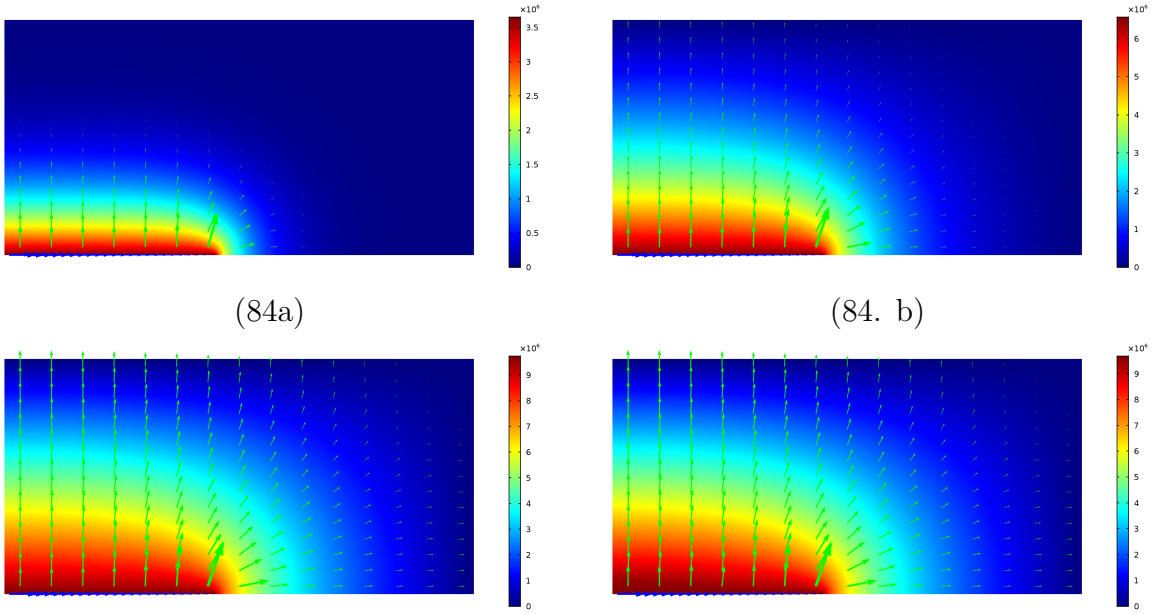

(84a) (84. b)

(84c) (84d)

Figure 84: Pressure distribution for Ottawa 20/40. From a to d, figures are after an injection time of 1 *hour*, 4 *hour*, 1 *day*, and 60 *day*. Scaling and units are the same as Figure 82. Pressure distribution suggests formation linear flow regime. The change in permeability has limited influence on the flow pattern.

several orders of magnitude, i.e., HF acid cannot be diffused or convected deep into the formation.

Inside domain, Figure 87 shows how HF acid concentration can be transported and what the flow pattern looks like. From Figure. 87a to Figure. 87d, the concentration of the tracer represent the flow pattern inside the regime. At low injection speed, the flow is more like radial and fluid tracer diffused into the reservoir. With a greater injection speed, the fluid flow become more formation linear and dispersion is limited. The concentration profile of the HF acid also indicates the treatment front as discussed in above context. With a higher injection rate, the treatment will be more effective.

Under different fracture conductivity, we can clearly identify the differences between flow pattern, which is more radial in low conductivity, and linear in high conductivity. However, the fracture recovery is not significantly improved based on the concentration profile of the HF acid (see Figure 88).

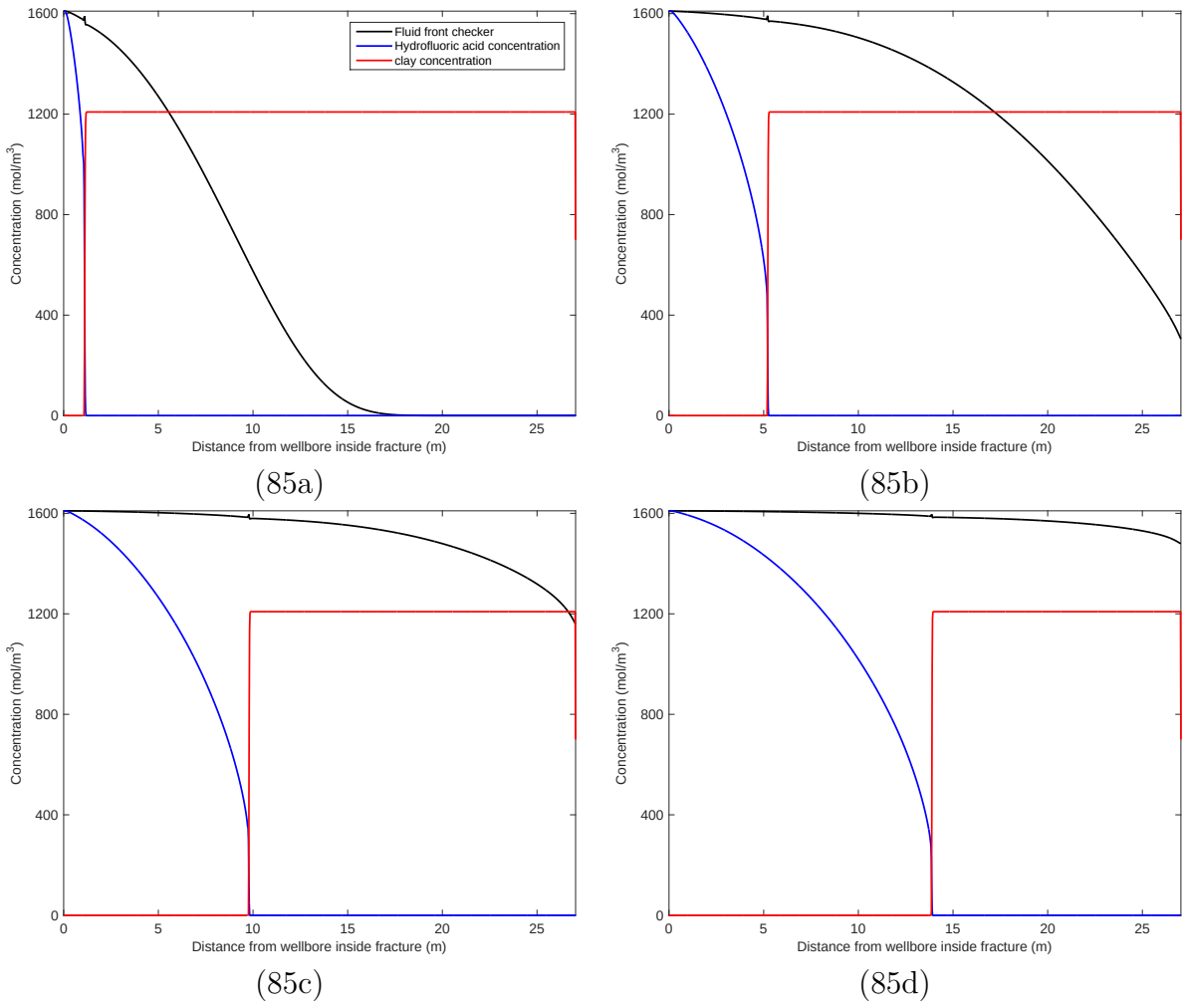

Figure 85: Concentration profile inside the fracture. From a to d, they are after injection 1 *day*, 10 *day*, 30 *day* and 60 *day* with a rate of 35 m^3/day. Fluid front can be identified as half concentration of the tracer in the fluid.

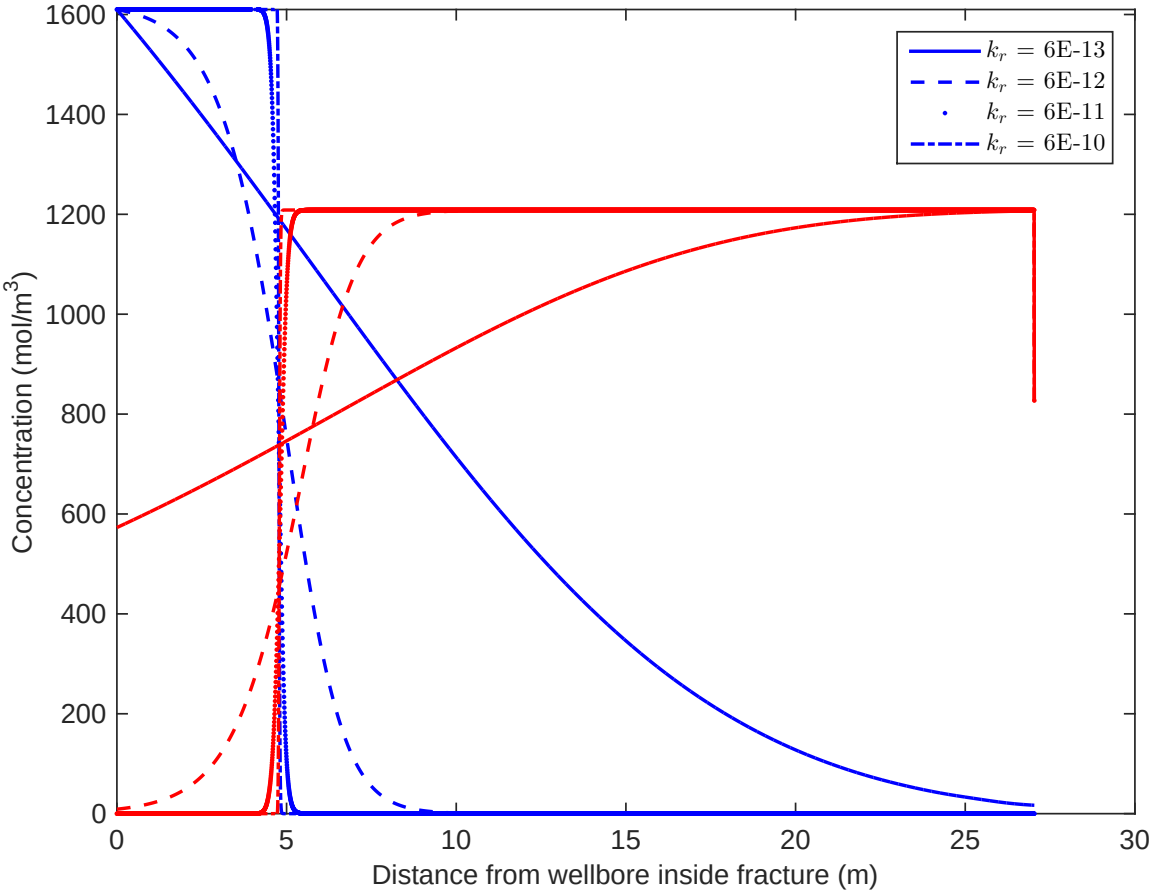

Figure 86: Effect of reaction coefficient after injecting 1 day while injecting with 35 m^3/day. Red lines are concentration of clay, and blue lines are concentration of HF acid. At a surface reaction rate of 6×10^{-13} m/s, the HF acid penetrates the reaction interface.

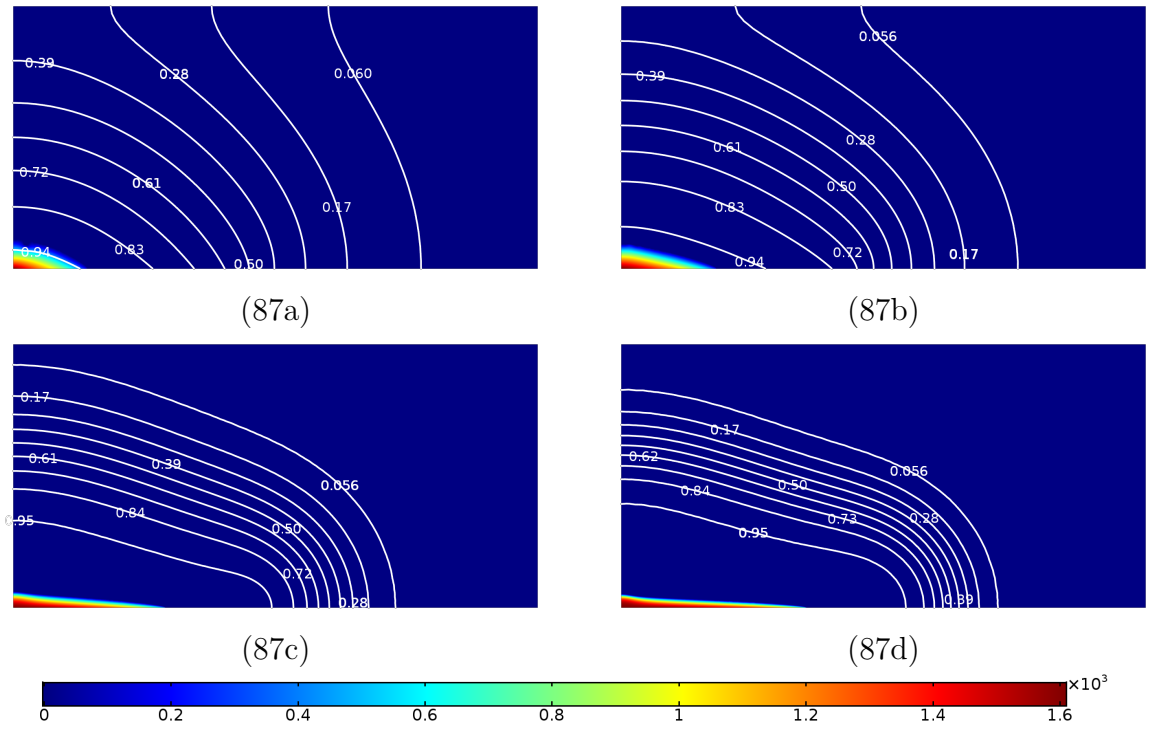

Figure 87: Concentration profile of tracer and HF acid with different injection rate. a, b, c, and d are regarding to a injection rate of 8.75 m^3/day, 17.5 m^3/day, 70 m^3/day, and 140 m^3/day, respectively. Color contour is the concentration profile of the HF acid, and isolines are concentration of fluid tracer normalized by the inlet concentration.

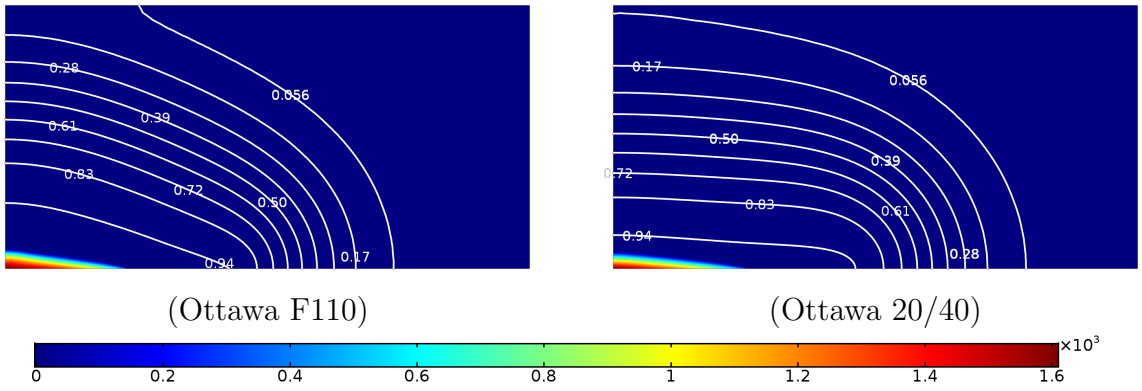

Figure 88: Comparison between different fracture conductivity, at a injection rate of 35 m^3/day.

5.4.3 Fracture treatment

As discussed in the above texts, the clay - HF acid interface can be regarded as the treatment front of the fracture. Overall simulation results on fracture treatment is provided in Figure 89. The injection rate can be normalized with Reynolds number $Re = \rho_w u b_f/\mu$, and u is the inlet velocity. The reaction front propagates with the injected HF acid, but overall treatment rate is dropping as injection continues. Again the effect of the $(k_f b_f)_D$ has limited effect on the recovery. An alternative mapping with different injection conditions at different dimensionless injection time t_{Dx_f} can be plotted to interpolate any case of injection within the same model setup (see Figure. 90).

$$t_{Dx_f} = \frac{\beta k_{res} t}{n_{res} \mu c_t x_f^2}, \tag{76}$$

where the total compressibility c_t depends on the compressibility of fluid and porous media. Since we apply rigid condition on porous media, the total compressibility simply reduces to compressibility of the fluid. β is a unit conversion constant. The units of k_{res} and t here are μm^2 and *hour* respectively. From Figure 90, it can be seen that the recovery almost reaches a plateau as injection continues at low injection Reynolds number Re, and the lower Re the lower cleaning efficiency. Therefore, under the allowable pressure, the injection rate should be maximized to maximize the efficiency of acid cleaning.

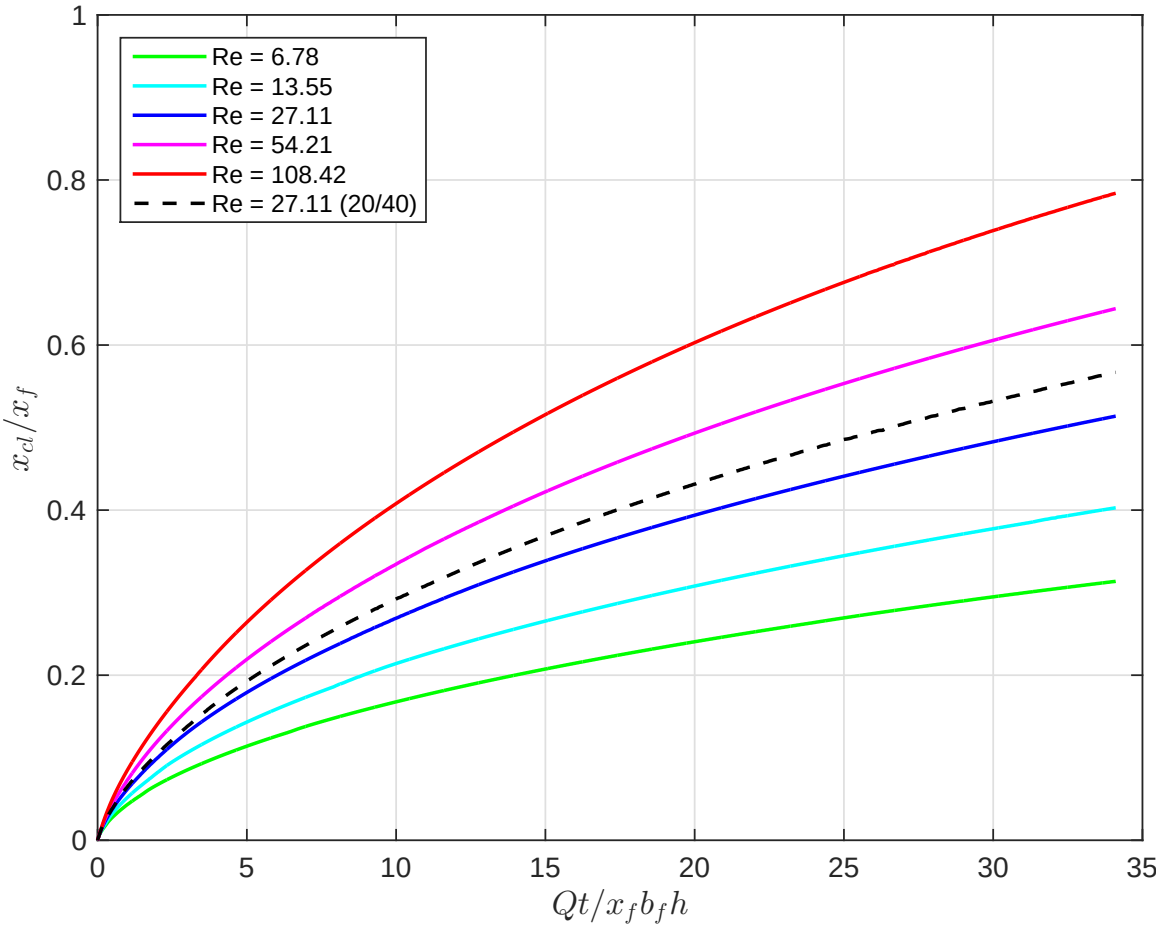

Figure 89: Fracture treatment with normalized injected volume. All solid lines represent model of Ottawa F110 proppant, and dotted line for Ottawa 20/40 proppant. x_{cl} is the reaction front.

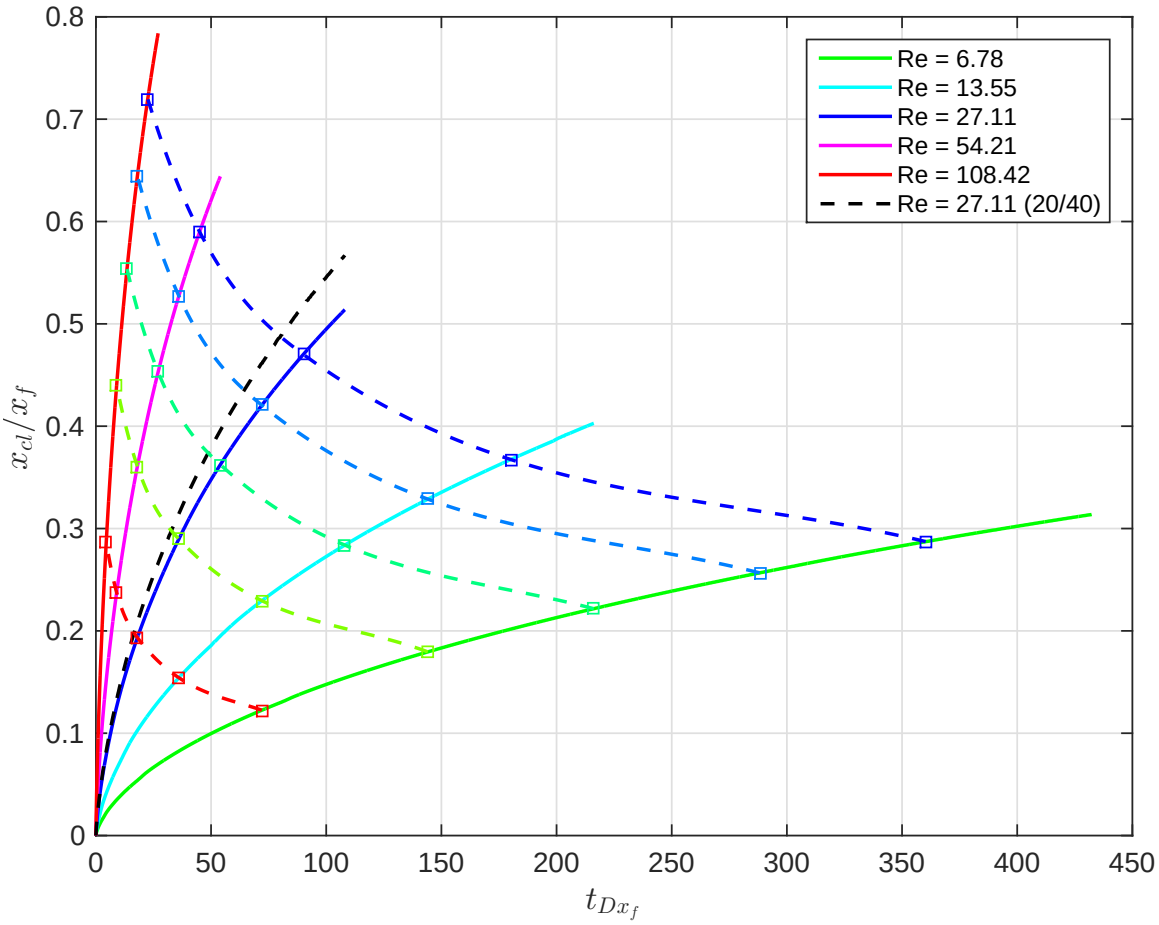

Figure 90: Fracture treatment map vs t_{wD}. x_{cl} indicates the location of the reaction front. The markers with same color are reaction fronts at equal amounts of injected volume. Dotted lines suggest the possibility to interpolate fracture treatment status under other injection conditions.

5.5 Conclusions

The acid cleaning process is simulated using a hydro-chemically coupled scheme implemented in an equation based solver COMSOL Multiphysics®. Effects of injection rate, dimensionless fracture conductivity, and reaction rate on the effectiveness of acid cleaning are examined. It is found that inlet Reynolds number governs the efficiency of acid cleaning, while effects of dimensionless fracture conductivity and reaction rate

are relatively insensitive. Outcomes from this research could serve as guidelines to optimize the field practice. Furthermore, one should be aware of the risk that such fast rate of reaction can also lead to the quartz exposed to high concentration of HF near the wellbore and inside cured fracture, which may result in non-negligible reaction between HF acid and quartz component of proppant and sandstone [76, 88, 77, 69]. The effect of the reaction between HF and quartz need to be further explored.

Table 12: Nomenclatures

Parameter	Description	Parameter	Description
ρ	Fluid density	k_{f1}	Fracture permeability after damage
ρ_0	Reference density	k_{res}	Instant reservoir permeability
c_f	Fluid compressibility	k_{res0}	Initial reservoir permeability
t	Time	ξ	Initial clay portion in fracture
$\boldsymbol{u}$	Darcy velcocity	G_c	Specific gravity of clay
k	Permeability	G_s	Specific gravity of sandstone
μ	Fluid viscosity	ρ_s	Density of reservoir mass
p	Fluid pressure	ρ_w	Density of water
p_0	Reference pressure	ζ	Reservoir fine content weight %
p_b	Model back pressure	L	Reservoir length
n	Porosity	W	Reservoir width
$\dot{S}$	Mass source term	H	Formation height
c_i	Concentration of chemical specie i	r_w	Fracture radius/half width
D_i	Diffusion coefficient of specie i	b_f	Fracture width
R_i	Reaction rate of specie i	x_f	Fracture length
c_{HF}	Concentration of hydrofluoric (HF) acid	Q	Injection rate of chemical solution
c_{tracer}	Concentration of fluid flow tracer	s	Reaction rate coefficient
D_{HF}	Dispersion coefficient of HF acid	h	Mesh size
D_{tracer}	Dispersion coefficient of tracer	D_d	Diffusion coefficient
k_r	Surface reaction rate	D_i	Dispersion coefficient of specie i
k_b	Bulk reaction rate	Da	Damköhler number
a	Reactive surface area of clay	Pe	Peclet number
M_{clay}	Molar mass of clay	$(k_f b_f)_D$	Dimensionless fracture conductivity
w_{clay}	Unit mass of clay per unit volume	L_D	Characteristic length of dispersion
n_f	Instant fracture porosity	p_{wD}	Dimensionless wellbore pressure
n_{f0}	Fracture porosity before damage	α_o	Unit conversion constant
n_r	Instant reservoir porosity	B	Formation volume factor
n_{r0}	Initial reservoir porosity	β	Unit conversion constant
k_f	Instant fracture permeability	c_t	Total compressibility
k_{f0}	Fracture permeability before damage	x_{cl}	Location of the reaction front

CHAPTER VI

CONCLUSIONS AND FUTURE WORK

In this work, both the fracturing and acid cleaning processes in the unconsolidated formations are examined. Specifically, we first focus on how fracture morphology and fluid leakoff are affected by the injection rate, fluid rheology, and formation permeability. Then we numerically analyze the acid cleaning process to recover fractures damaged from fines migration.

A series of injection experiments is performed with mixtures of sand and silica flour. As the weight percentage of the silica flour increases, the matrix permeability decreases significantly and the capillary effect becomes non-negligible. The capillary effect at low permeability restrains the grain movements and promotes the fluid infiltration. Results also show a variation in fractal dimension of the fingering geometry suggesting the surface tension at low permeability probably restrains grain rotational and sliding movements. An additional dimensionless number incorporating surface tension is derived to characterize the fluid-grain displacement. A methodology for classifying the fluid-grain displacement patterns based on two dimensionless numbers is suggested.

The process of fluid injection into dense granular media is modeled using the DEM code PFC2D® coupled with a pore network model with the focus on the effect of non-Newtonian rheology. The numerical analysis shows that for a shear thinning fluid, the high shear rheology is critical to the early time near-wellbore behaviors. The transition in the fluid flow and granular response is reflected not only in the partition of the injected fluid volume between the pore spaces and the newly created openings, but also in the wellbore pressure history and the energy partition in the system. As the

injection rate becomes large, the breakdown pressure becomes insensitive to the fluid rheology. An apparent viscosity of non-Newtonian shear thinning fluid is defined to characterize the fluid-grain displacement patterns during fluid injection into a densely packed granular medium. The DEM coupled analysis provides valuable insights into the effect of shear thinning rheology on the injection process.

As a continuum approach, the pressurized fracture propagation process is simulated with phase field method. A hybrid phase field method is developed by adopting viscous phase evolution and the hybrid scheme for constitutive law to reduce the computational cost and enhance the stability. The model is constructed and implemented into the equation based solver COMSOL Multiphysics®. The model is verified with the classic Griffith's theory and Sneddon's solution. Furthermore, it is shown in this work that the constructed model is capable of modeling complicated fracture growth such as merging and tip splitting. Crack growth from a wellbore is modeled under various stress conditions.

The acid cleaning process is simulated using a hydro-chemically coupled scheme implemented in an equation based solver COMSOL Multiphysics®. Effects of injection rate, dimensionless fracture conductivity, and reaction rate on the effectiveness of acid cleaning are examined. It is found that inlet Reynolds number governs the efficiency of acid cleaning, while effects of dimensionless fracture conductivity and reaction rate are relatively insensitive. Outcomes from this research could serve as guidelines to optimize the field practice.

Suggestions for future work on this topic are as follows:

1. Injection problem under field condition needs to be investigated, including anisotropic stress condition and other complexity.

2. More complex rheology should be incorporated into the model to cover the full aspects of non-Newtonian fluid characteristics such as, zero-shear zone, yield stress, and multi-phase characteristics such as internal and external filter cake

formation. Numerical analysis on effects of other complexities of fluid rheology. After the consideration of the full signatures of a non-Newtonian fluid, the simulation results can be compared with the laboratory injection experiments or field test and serve as guidelines to optimize the field practice.

3. The current 2D DEM-pore network model is only able to simulate granular fingering in two dimensional. Improvement is needed in order to further investigate the creation of fingers in 3D.

4. In this work, the phase field method is developed based on brittle failure mechanism. However, fracture is not necessarily a sharp discontinuity. Damaged zone could form along the fracture surface. The degradation of the material property may not follow simple quadratic function used in this work. Therefore, further examination of the degradation function in phase field approach is important to investigate how it could best reflect the real physics.

5. Comparison of the acid cleaning process with field or laboratory testing.

REFERENCES

[1] Al-Busaidi, A., Hazzard, J. F., and Young, R. P., "Distinct element modeling of hydraulically fractured Lac du Bonnet granite," *J. Geophys. Res.*, vol. 110, pp. B06302, doi:10.1029/2004JB003297, 2005.

[2] Ambati, M., Gerasimov, T., and Lorenzis, L. D., "A review on phase-field models of brittle fracture and a new fast hybrid formulation," *Computational Mechanics*, vol. 55, pp. 383–405, dec 2014.

[3] Ambrosio, L. and Tortorelli, V. M., "Approximation of functional depending on jumps by elliptic functional via t-convergence," *Communications on Pure and Applied Mathematics*, vol. 43, no. 8, pp. 999–1036, 1990.

[4] Amor, H., Marigo, J.-J., and Maurini, C., "Regularized formulation of the variational brittle fracture with unilateral contact: Numerical experiments," *Journal of the Mechanics and Physics of Solids*, vol. 57, no. 8, pp. 1209 – 1229, 2009.

[5] Anderson, T. L., *Fracture mechanics: fundamentals and applications*. CRC press, 2005.

[6] B. Bourdin, G. F. and Marigo, J.-J., "Numerical experiments in revisited brittle fracture," *Journal of the Mechanics and Physics of Solids*, vol. 48, no. 4, pp. 797 – 826, 2000.

[7] Bear, J., *Dynamics of fluids in porous media*. Courier Corporation, 2013.

[8] Blunt, M. J., "Flow in porous media - pore-network models and multiphase flow," *Current opinion in colloid & interface science*, vol. 6, no. 3, pp. 197–207, 2001.

[9] Bohloli, B. and de Pater, C., "Experimental study on hydraulic fracturing of soft rocks: Influence of fluid rheology and confining stress," *Journal of Petroleum Science and Engineering*, vol. 53, no. 1, pp. 1 – 12, 2006.

[10] Bourdin, B., Chukwudozie, C. P., and Yoshioka, K., "A variational approach to the numerical simulation of hydraulic fracturing," in *SPE Annual Technical Conference and Exhibition*, Society of Petroleum Engineers, 2012.

[11] Cahn, J. W. and Hilliard, J. E., "Free energy of a nonuniform system. I. Interfacial free energy," *The Journal of Chemical Physics*, vol. 28, no. 2, pp. 258–267, 1958.

[12] Chang, H., *Hydraulic fracturing in particulate materials*. PhD thesis, Georgia Institute of Technology, 2004.

[13] Chen, L., "Phase-field models for microstructure evolution," *Annual Review of Materials Research*, vol. 32, no. 1, pp. 113–140, 2002.

[14] Cheng, X., Xu, L., Patterson, A., Jaeger, H. M., and Nagel, S. R., "Towards the zero-surface-tension limit in granular fingering instability," *Nature Physics*, vol. 4, no. 3, pp. 234–237, 2008.

[15] Choo, H., *Engineering behavior and characterization of physical-chemical particulate mixtures using geophysical measurement techniques*. PhD thesis, Georgia Institute of Technology, 2013.

[16] Chuoke, R., van Meurs, P., and van der Poel, C., "The instability of slow, immiscible, viscous liquid-liquid displacements in permeable media," *Trans. AIME*, vol. 216, 1959.

[17] Cinco-Ley, H. and Samaniego-V, F., "Transient pressure analysis for fractured wells," *Journal of petroleum technology*, vol. 33, no. 09, pp. 1–749, 1981.

[18] COMSOL Multiphysics®, *COMSOL Reference Manual, pp. 185-191*. COMSOL AB, Stockholm, Sweden, v. 5.2 ed., 2015.

[19] Crowe, C., Masmonteil, J., and Thomas, R., "Trends in matrix acidizing," *Oilfield Review*, vol. 4, no. 4, pp. 22–40, 1992.

[20] Daccord, G., "Chemical dissolution of a porous medium by a reactive fluid," *Physical review letters*, vol. 58, no. 5, p. 479, 1987.

[21] de Pater, C. J., Dong, Y., and Bohloli, B., "Experimental study of hydraulic fracturing in sand as a function of stress and fluid rheology," in *SPE hydraulic fracturing technology conference*, Society of Petroleum Engineers, 2007.

[22] Dong, Y. and de Pater, C., "Observation and modeling of the hydraulic fracture tip in sand," in *The 42nd US Rock Mechanics Symposium (USRMS)*, American Rock Mechanics Association, 2008.

[23] Dong, Y., *Hydraulic fracture containment in sand*. PhD thesis, Delft University of Technology, 2010.

[24] Eastgate, L., Sethna, J. P., Rauscher, M., Cretegny, T., Chen, C.-S., and Myers, C., "Fracture in Mode I using a conserved phase-field model," *Physical Review E*, vol. 65, no. 3, p. 036117, 2002.

[25] Economides, M. J. and Nolte, K. G., *Reservoir stimulation*, vol. 18. Wiley New York, 2000.

[26] Fatt, I., "The network model of porous media I. Capillary pressure characteristics," *Trans. AIME*, 1956.

[27] Francfort, G. and Marigo, J.-J., "Revisiting brittle fracture as an energy minimization problem," *Journal of the Mechanics and Physics of Solids*, vol. 46, no. 8, pp. 1319 – 1342, 1998.

[28] Fuggle, A. R., *Geomaterial gradation influences on interface shear behavior*. PhD thesis, Georgia Institute of Technology, 2011.

[29] Germanovich, L. N., Hurt, R. S., Ayoub, J. A., Siebrits, E., Norman, D., Ispas, I., and Montgomery, C. T., "Experimental study of hydraulic fracturing in unconsolidated materials," in *SPE International Symposium and Exhibition on Formation Damage Control*, Society of Petroleum Engineers, 2012.

[30] Golovin, E., Jasarevic, H., Chudnovsky, A., Dudley, J. W., and Wong, G. K., "Observation and characterization of hydraulic fracture in cohesionless sand," in *44th US Rock Mechanics Symposium and 5th US-Canada Rock Mechanics Symposium*, American Rock Mechanics Association, 2010.

[31] Griffith, A. A., "The phenomena of rupture and flow in solids," *Philosophical Transactions of the Royal Society of London A: Mathematical, Physical and Engineering Sciences*, vol. 221, no. 582-593, pp. 163–198, 1921.

[32] Guppy, K. H., Cinco-Ley, H., Ramey Jr., H. J., and Samaniego-V., F., "Non-darcy flow in wells with finite-conductivity vertical fractures," *Society of Petroleum Engineers Journal*, vol. 22, no. 05, pp. 681–698, 1982.

[33] Gwaba, D., *Fluid-assisted fracturing in geological materials*. PhD thesis, Georgia Institute of Technology, 2016.

[34] Haralock, R. M. and Shapiro, L. G., *Computer and robot vision*. Addison-Wesley Longman Publishing Co., Inc., 1991.

[35] Henry, H. and Levine, H., "Dynamic instabilities of fracture under biaxial strain using a phase field model," *Physical Review Letters*, vol. 93, sep 2004.

[36] Hill, S., A., M., P., F. I., and F.S.S., "Channeling in packed columns," *Chemical Engineering Science*, vol. 1, no. 6, pp. 247–253, 1952.

[37] Holtzman, R., Szulczewski, M. L., and Juanes, R., "Capillary fracturing in granular media," *Physical review letters*, vol. 108, no. 26, p. 264504, 2012.

[38] Homsy, G. M., "Viscous fingering in porous media," *Annual review of fluid mechanics*, vol. 19, no. 1, pp. 271–311, 1987.

[39] Hou, Y., Wang, L., Yue, P., Pauli, T., and Sun, W., "Modeling Mode I cracking failure in asphalt binder by using nonconserved phase-field model," *Journal of Materials in Civil Engineering*, vol. 26, no. 4, pp. 684–691, 2013.

[40] Huang, H., Zhang, F., Callahan, P., and Ayoub, J., "Fluid injection experiments in 2D porous media," *SPE J.*, vol. 17, no. 3, pp. 903–911, doi:10.2118/140502–PA, 2012.

[41] Huang, H., Zhang, F., Callahan, P., and Ayoub, J., "Granular fingering in fluid injection into dense granular media in a hele-shaw cell," *Physical review letters*, vol. 108, no. 25, p. 258001, 2012.

[42] Huang, H., Zhang, F., Callahan, P., and Ayoub, J. A., "Fluid injection experiments in two-dimensional porous media," in *SPE Hydraulic Fracturing Technology Conference*, Society of Petroleum Engineers, 2011.

[43] Hurt, R. S., *Toughness-dominated hydraulic fractures in cohesionless particulate materials*. PhD thesis, Georgia Institute of Technology, 2012.

[44] Ispas, I., Eve, R., Hickman, R., Keck, R. G., Willson, S. M., and Olson, K. E., "Laboratory testing and numerical modelling of fracture propagation from deviated wells in poorly consolidated formations," in *SPE Annual Technical Conference and Exhibition*, Society of Petroleum Engineers, 2012.

[45] Itasca Consulting Group, *PFC2D User Manual*. Minneapolis, Minnesota, 2008.

[46] Johnsen, Ø., Chevalier, C., Lindner, A., Toussaint, R., Clément, E., Måløy, K., Flekkøy, E., and Schmittbuhl, J., "Decompaction and fluidization of a saturated and confined granular medium by injection of a viscous liquid or gas," *Physical Review E*, vol. 78, no. 5, p. 051302, 2008.

[47] Johnsen, Ø., Toussaint, R., Måløy, K. J., Flekkøy, E. G., and Schmittbuhl, J., "Coupled air/granular flow in a linear hele-shaw cell," *Physical Review E*, vol. 77, no. 1, p. 011301, 2008.

[48] Johnsen, Ø., Toussaint, R., Måløy, K. J., and Flekkøy, E. G., "Pattern formation during air injection into granular materials confined in a circular hele-shaw cell," *Physical Review E*, vol. 74, no. 1, p. 011301, 2006.

[49] Kang, Q., Chen, L., Valocchi, A. J., and Viswanathan, H. S., "Pore-scale study of dissolution-induced changes in permeability and porosity of porous media," *Journal of Hydrology*, vol. 517, pp. 1049–1055, 2014.

[50] Kang, Q., Zhang, D., and Chen, S., "Simulation of dissolution and precipitation in porous media," *Journal of Geophysical Research: Solid Earth*, vol. 108, no. B10, 2003.

[51] Karma, A., Kessler, D. A., and Levine, H., "Phase-field model of Mode III dynamic fracture," *Physical Review Letters*, vol. 87, jul 2001.

[52] Khodaverdian, M. and McElfresh, P., "Hydraulic fracturing stimulation in poorly consolidated sand: mechanisms and consequences," in *SPE Annual Technical Conference and Exhibition*, Society of Petroleum Engineers, 2000.

[53] Khodaverdian, M., Sorop, T., Postif, S. J., and Van den Hoek, P. J., "Polymer flooding in unconsolidated-sand formations: Fracturing and geomechanical considerations," *SPE Production & Operations*, vol. 25, no. 02, pp. 211–222, 2010.

[54] Kuhn, C. and Müller, R., "A continuum phase field model for fracture," *Engineering Fracture Mechanics*, vol. 77, no. 18, pp. 3625 – 3634, 2010. Computational Mechanics in Fracture and Damage: A Special Issue in Honor of Prof. Gross.

[55] Lee, J.-S., Dodds, J., and Santamarina, J. C., "Behavior of rigid-soft particle mixtures," *Journal of materials in civil engineering*, vol. 19, no. 2, pp. 179–184, 2007.

[56] Lee, S., Wheeler, M. F., and Wick, T., "Pressure and fluid-driven fracture propagation in porous media using an adaptive finite element phase field model," *Computer Methods in Applied Mechanics and Engineering*, vol. 305, pp. 111 – 132, 2016.

[57] Lee, S., Wheeler, M. F., and Wick, T., "Iterative coupling of flow, geomechanics and adaptive phase-field fracture including level-set crack width approaches," *Journal of Computational and Applied Mathematics*, vol. 314, pp. 40–60, 2017.

[58] Lemaire, E., Abdelhaye, Y. O. M., Larue, J., Benoit, R., Levitz, P., and van Damme, H., "Pattern formation in noncohesive and cohesive granular media," *Fractals*, vol. 1, no. 04, pp. 968–976, 1993.

[59] Lemaire, E., Levitz, P., Daccord, G., and van Damme, H., "From viscous fingering to viscoelastic fracturing in colloidal fluids," *Physical review letters*, vol. 67, no. 15, p. 2009, 1991.

[60] Lenormand, R., Touboul, E., and Zarcone, C., "Numerical models and experiments on immiscible displacements in porous media," *Journal of Fluid Mechanics*, vol. 189, pp. 165–187, 1988.

[61] Li, L. and Holt, R. M., "Simulation of flow in sandstone with fluid coupled particle model," in *DC Rocks 2001, The 38th US Symposium on Rock Mechanics (USRMS)*, American Rock Mechanics Association, 2001.

[62] Li, S., Lowengrub, J. S., Fontana, J., and Palffy-Muhoray, P., "Control of viscous fingering patterns in a radial hele-shaw cell," *Physical review letters*, vol. 102, no. 17, p. 174501, 2009.

[63] Løvoll, G., Méheust, Y., Toussaint, R., Schmittbuhl, J., and Måløy, K. J., "Growth activity during fingering in a porous hele-shaw cell," *Physical Review E*, vol. 70, no. 2, p. 026301, 2004.

[64] MacMinn, C. W., Dufresne, E. R., and Wettlaufer, J. S., "Fluid-driven deformation of a soft granular material," *Physical Review X*, vol. 5, no. 1, p. 011020, 2015.

[65] Måløy, K. J., Feder, J., and Jøssang, T., "Viscous fingering fractals in porous media," *Physical review letters*, vol. 55, no. 24, p. 2688, 1985.

[66] Mandelbrot, B. B., *The fractal geometry of nature*, vol. 173. Macmillan, 1983.

[67] Mauthe, S. and Miehe, C., "Hydraulic fracture in poro-hydro-elastic media," *Mechanics Research Communications*, vol. 80, pp. 69 – 83, 2017. Multi-Physics of Solids at Fracture.

[68] Maxworthy, T., "The nonlinear growth of a gravitationally unstable interface in a hele-shaw cell," *Journal of Fluid Mechanics*, vol. 177, pp. 207–232, 1987.

[69] McLeod, H. O., "Matrix acidizing," *Journal of Petroleum Technology*, vol. 36, no. 12, pp. 2–055, 1984.

[70] Miehe, C., Welschinger, F., and Hofacker, M., "Thermodynamically consistent phase-field models of fracture: Variational principles and multi-field fe implementations," *International Journal for Numerical Methods in Engineering*, vol. 83, no. 10, pp. 1273–1311, 2010.

[71] Miehe, C., Hofacker, M., and Welschinger, F., "A phase field model for rate-independent crack propagation: Robust algorithmic implementation based on operator splits," *Computer Methods in Applied Mechanics and Engineering*, vol. 199, pp. 2765–2778, nov 2010.

[72] Miehe, C. and Mauthe, S., "Phase field modeling of fracture in multi-physics problems. part iii. crack driving forces in hydro-poro-elasticity and hydraulic fracturing of fluid-saturated porous media," *Computer Methods in Applied Mechanics and Engineering*, vol. 304, pp. 619 – 655, 2016.

[73] Mikelić, A., Wheeler, M. F., and Wick, T., "A phase field approach to the fluid filled fracture surrounded by a poroelastic medium," *ICES report*, vol. 1315, 2013.

[74] Mikelić, A., Wheeler, M. F., and Wick, T., "A phase-field method for propagating fluid-filled fractures coupled to a surrounding porous medium," *Multiscale Modeling & Simulation*, vol. 13, no. 1, pp. 367–398, 2015.

[75] Mikelić, A., Wheeler, M. F., and Wick, T., "A quasi-static phase-field approach to pressurized fractures," *Nonlinearity*, vol. 28, no. 5, p. 1371, 2015.

[76] Monk, D. J., Soane, D. S., and Howe, R. T., "A review of the chemical reaction mechanism and kinetics for hydrofluoric acid etching of silicon dioxide for surface micromachining applications," *Thin Solid Films*, vol. 232, no. 1, pp. 1–12, 1993.

[77] Monk, D. J., Soane, D. S., and Howe, R. T., "Hydrofluoric acid etching of silicon dioxide sacrificial layers i. experimental observations," *Journal of the Electrochemical Society*, vol. 141, no. 1, pp. 264–269, 1994.

[78] Muecke, T. W., "Formation fines and factors controlling their movement in porous media," *Journal of Petroleum Technology*, vol. 31, no. 02, pp. 144–150, 1979.

[79] Mulligan, C., Yong, R., and Gibbs, B., "Surfactant-enhanced remediation of contaminated soil: a review," *Engineering Geology*, vol. 60, no. 1, pp. 371–380, 2001.

[80] Paterson, L., "Radial fingering in a hele shaw cell," *Journal of Fluid Mechanics*, vol. 113, pp. 513–529, 1981.

[81] Potyondy, D. O. and Cundall, P. A., "A bonded-particle model for rock," *International journal of rock mechanics and mining sciences*, vol. 41, no. 8, pp. 1329–1364, 2004.

[82] Provatas, N. and Elder, K., *Phase-field methods in materials science and engineering*. John Wiley & Sons, 2011.

[83] Saffman, P. G. and Taylor, G., "The penetration of a fluid into a porous medium or hele-shaw cell containing a more viscous liquid," *Proceedings of the Royal Society A: Mathematical, Physical and Engineering Sciences*, vol. 245, pp. 312–329, June 1958.

[84] Salgado, R., Bandini, P., and Karim, A., "Shear strength and stiffness of silty sand," *Journal of Geotechnical and Geoenvironmental Engineering*, vol. 126, no. 5, pp. 451–462, 2000.

[85] Sears, F. W. and Zemansky, M. W., *University physics: Mechanics, heat and sound*. Addison-Wesley, 1963.

[86] Semmens, B. and Meggy, A., "The reaction of kaolin with fluorides. ii. effect of aqueous hydrofluoric acid," *Journal of Applied Chemistry*, vol. 16, no. 4, pp. 125–128, 1966.

[87] Shimizu, H., Murata, S., and Ishida, T., "The distinct element analysis for hydraulic fracturing in hard rock considering fluid viscosity and particle size distribution," *International Journal of Rock Mechanics and Mining Sciences*, vol. 48, no. 5, pp. 712–727, 2011.

[88] Smith, C., Hendrickson, A., and others, "Hydrofluoric acid stimulation of sandstone reservoirs," *Journal of Petroleum Technology*, vol. 17, no. 02, pp. 215–222, 1965.

[89] Sneddon, I. N. and Lowengrub, M., "Crack problems in the classical theory of elasticity," *1969, 221 P*, 1969.

[90] Thallak, S., Rothenburg, L., and Dusseault, M., "Simulation of multiple hydraulic fractures in a discrete element system," in *The 32nd US Symposium on Rock Mechanics (USRMS)*, American Rock Mechanics Association, 1991.

[91] Trojer, M., Szulczewski, M. L., and Juanes, R., "Stabilizing fluid-fluid displacements in porous media through wettability alteration," *Physical Review Applied*, vol. 3, no. 5, p. 054008, 2015.

[92] van Damme, H. and Lemaire, E., "From flow to fracture and fragmentation in colloidal media," in *Disorder and Fracture*, pp. 83–104, Springer, 1990.

[93] van Damme, H., Lemaire, E., Ould, Y., Abdelhaye, M., Mourchid, A., and Levitz, P., "Pattern formation in particulate complex fluids: A guided tour," *Non-linearity and breakdown in soft condensed matter*, pp. 134–150, 1994.

[94] Weinberg, K., Dally, T., Schuss, S., Werner, M., and Bilgen, C., "Modeling and numerical simulation of crack growth and damage with a phase field approach," *GAMM-Mitteilungen*, vol. 39, pp. 55–77, may 2016.

[95] Wheeler, M., Wick, T., and Wollner, W., "An augmented-lagrangian method for the phase-field approach for pressurized fractures," *Computer Methods in Applied Mechanics and Engineering*, vol. 271, pp. 69 – 85, 2014.

[96] Zhang, F., Damjanac, B., and Huang, H., "Coupled discrete element modeling of fluid injection into dense granular media," *Journal of Geophysical Research: Solid Earth*, vol. 118, no. 6, pp. 2703–2722, 2013.

[97] Zhang, F., Huang, H., and Damjanac, B., "Dem/pore network modeling of fluid injection into granular media," in *46th US Rock Mechanics/Geomechanics Symposium*, American Rock Mechanics Association, 2012.

[98] Zhang, T. Y. and Suen, C. Y., "A fast parallel algorithm for thinning digital patterns," *Communications of the ACM*, vol. 27, no. 3, pp. 236–239, 1984.

[99] Zhao, X. and Paul Young, R., "Numerical modeling of seismicity induced by fluid injection in naturally fractured reservoirs," *Geophysics*, vol. 76, no. 6, pp. WC167–WC180, 2011.

VITA

Longde Jin was born in Yanji, China, on November 13 (October 5th in lunar calendar), 1988. Between 2007 and 2011, he obtained his B.S. in Mechanical Engineering from University of Science and Technology of China. In August 2011, he started his graduate study in the Geosystems Engineering Group at the School of Civil and Environmental Engineering in Georgia Institute of Technology under the supervision of Dr. Haiying Huang. He obtained a M.S. degree in Civil Engineering in 2014 and will receive a Ph.D. degree in Civil Engineering in December 2017 from Georgia Institute of Technology.